The role of MKI67 in the regulation of 60S pre-ribosome nucleolar export, transcripts, energy supply, and apoptosis

Shiro Iuchi and Joao A. Paulo

Department of Cell Biology
Harvard Medical School, 240 Longwood Ave., Boston, MA, 02115, USA

Email: shiro_iuchi@hms.harvard.edu

ABSTRACT

MKI67 (Ki67) is expressed exclusively in proliferating cells in human tissues, rendering it as a valuable diagnostic marker for cancer. However, the function of this protein in cells remains unclear. In this study, we present the findings on the regulatory functions of MKI67 in conjunction with its partner proteins GNL2 and MDN1, which are involved in pre-ribosome processing, as well as the regulatory functions in its absence. In proliferating HEK293T cells, MKI67 binds contiguously to the chromatin in conjunction with GNL2 and MDN1, localizing most densely to the nucleolar periphery to regulate 60S pre-ribosome export. On the other hand, RNA-seq analysis reveals that these three proteins can independently regulate many target transcripts, but they often share their target transcripts, yet often regulate them at different expression levels. MDN1 depletion strongly downregulates RNA gene transcripts involved in ribosome biogenesis and splicing. In contrast, MKI67 depletion strongly upregulates transcripts of protein-coding genes, including synapse-specific proteins and the mitosis-related protein HEK7. Furthermore, MKI67 depletion coordinately up- or down-regulates the levels of transcripts of several pathways, thereby enabling MKI67-depleted cells to adapt to less active metabolic states. The underlying mechanism by which MKI67 depletion upregulates transcripts appears to involve attenuation of transcript levels in cooperation with mRNA degradation systems, as evidenced by analysis of HEK7 and UNC13A translations. In conclusion, the present results indicate that MKI67 contributes to proliferation via nucleolar export of 60S pre-ribosome particles and high energy supply. Conversely, its absence leads the cells to adapt to the senescent and differentiated conditions.

INTRODUCTION

MKI67 has been studied and used for the diagnosis of malignant neoplasms and cancers because the protein was found to be present in proliferating cells but not in quiescent cells, suggesting that it may be a potent tool for simple and rapid evaluation of proliferating cells, i.e., cancer cells, in a tumor (Gerdes et al., 1983; Scholzen & Gerdes, 2000). However, knockdown and knockout of this gene do not apparently stop cell proliferation (Garwain et al., 2021; Iuchi & Paulo, 2021; Sobecki et al., 2016), suggesting that the role of MKI67 in proliferation remains to be elucidated. Since the discovery of Ki67 including its 2 versions (Gerdes et al., 1983; Grasmann et al., 2019), several groups have steadily gained insight into this protein. The long Ki67 is a large protein consisting of 3256 amino acid residues while the shorter one is 2896 AA long. The only difference between the two versions is the exclusion of MKI67$^{135\text{-}494}$ in the short form and both proteins share the same characteristics (Saiwaki et al., 2005). As shown in Figure 1A, the long MKI67 contains positively and negatively charged amino acids along the entire molecule and thus the protein can be stretched long due to many Intrinsically Disordered Regions (IDRs) (Booth & Earnshaw, 2017; Iuchi & Paulo, 2021). This protein consists of, from the N-terminus, the FHA (forkhead associated) domain that interacts with NIFK (Takagi et al., 2001), the PP1 binding site that interacts with the serine/threonine protein phosphatase PP1-gamma catalytic subunit (PP1G) (Booth et al.,

2014;(Takagi et al., 2014), 16 repeats each consisting of 122 amino acid residues (Booth et al., 2014;(Gerdes et al., 1991)), and the C-terminal 321 amino acid peptide that contains at least two regions capable of binding to naked DNA without typical DNA binding motifs (MacCallum & Hall, 2000). The authors found that this C-terminus binds preferentially to AT-rich DNA by determining that poly(dI-dC).poly(dI-dC) and poly(dA-dT).poly(dA-dT) interfered much more strongly with the binding of pUC19 HaeIII digest to MKI67 than did poly(dG-dC).poly(dG-dC). In interphase cells, MKI67 binds to chromatin through the heterochromatin protein 1 group, CBX1(HP1$_\beta$) (Sobecki et al., 2016), in addition to naked DNA and colocalizes with nucleolar peripheral heterochromatin (Cheutin et al., 2003; Hori et al., 2023; Kreitz et al., 2000; Scholzen et al., 2002). This MKI67 at the nucleolar periphery is not static but undergoes dynamic turnover (Saiwaki et al., 2005; Sobecki et al., 2016). MKI67 was previously reported earlier to colocalize with the NORs in the nucleolus and was therefore thought to regulate transcription of the rRNA gene. However, an electron microscopy study found that MKI67 was never associated with FC or DFC where the rRNA the gene is transcribed but was associated with condensed chromatin at the nucleolar periphery (Cheutin et al., 2003; Hori et al., 2023). Consistent with this, one group has shown that MKI67 is not involved in regulating rRNA gene expression (Sobecki et al., 2016) but is involved in silencing transcription of other genes and organizing heterochromatin through H3K9me3 and CBX1(HP1β) (Sobecki et al., 2016). On the other hand, in prophase and mitosis, MKI67 uses both the C-terminal binding region, and the repeats present in the middle of the protein to loosely bind to chromosomes and form a thick layer called the prechromosomal layer (PCL) (Booth et al., 2014; Saiwaki et al., 2005;(Hayashi et al., 2017). The PCL acts as a surfactant to disperse chromosomes and prevent their collapse so that the haploid chromosomes are properly segregated to each daughter cell by mitotic microtubules (Cuylen et al., 2016). CDKs-mediated phosphorylation of Ki-67 in mitosis increases its propensity to undergo phase separation and gains association with the periphery of mitotic chromosomes (Valverde et al., 2023), but the phospho-moieties are removed by Ki-67-interacting PP1G in anaphase (Takagi et al., 2014). Transcription of the *MKI67* gene is regulated at its promoter by binding of the MuvB protein complex, which functions as a repressor complex when associated with additional factors in G0/G1, but as an activator when associated with other proteins in late G1 to M (Uxa et al., 2021). Accordingly, the *MKI67* mRNA is not expressed in G0/early G1 but begins to be expressed in late G1 and continues to increase throughout S, reaching its maximum level in prophase/mitosis. The level of MKI67 follows that of the mRNA with a lag of about 5 hours, and generally declines in general or becomes undetectable in G1 phase in some cell lines (Gerdes et al., 1984; Miller et al., 2018; Uxa et al., 2021). In addition, the *MKI67* gene expression is indirectly repressed by the tumor suppressors, RB and p53/p21 (Uxa et al., 2021). Interestingly, depletion of Ki-67 causes DNA damage during mitosis (Booth et al., 2014; Garwain et al., 2021) and concomitant depletion of p53 exacerbates the damage. However, this DNA damage can be prevented by expression of the C-terminal DNA-binding region of MKI67, suggesting that the Ki-67 C-terminus can maintain genome stability (Garwain et al., 2021).

Ribosome biogenesis involves many RNAs and proteins and involves the long journey of pre-60S ribosome particles to maturation in the cytoplasm (Klinge & Woolford, 2019;(Tomecki et al., 2017). Biogenesis begins with transcription of 45S RNA in the nucleolus from the tandemly arrayed *rRNA* genes/nucleolus organizer regions (NORs) of chr13, 14, 15, 21, and 22 p-arms, followed by processing of the 45S pre-rRNA and import of both 5S RNA transcribed from chr1 near the nucleolus (Hori et al., 2023) and proteins and RNPs required for pre-ribosome processing. RMRP and LAS1L are responsible for cleaving the pre-rRNA at ITS1 and ITS2, respectively, and the direct cleavage products, i.e., precursors of 5.8S and 38S RNA are then trimmed by exonuclease XN2 to the final 5.8S and 38S sizes, both of which remain with the pre-60S ribosome particle (Castle et al., 2012; Castle et al., 2010; Finkbeiner et al., 2011; Thiel et al., 2005; Tomecki et al., 2017). LAS1L is a subunit of the human RIX1 complex consisting of PELP1, NOL9, TEX10, WDR18, and SEN3P (Castle et al., 2012; Castle et al., 2010; Finkbeiner et al., 2011), and MDN1 can be a subunit of the RIX1 complex through direct interaction with PELP1 (Raman et al., 2016). This situation of MDN1 makes it unclear whether MDN1 is involved in the cleavage at ITS2. During the processing, H/ACA snoRNAs and C/D snoRNAs, which are abundant in the nucleolus, associate with different sets of core proteins to convert RNA uridines to pseudo-uridylated uridine and methylate ribose at the 2'-O position, respectively (Webster & Ghalei, 2023). These chemical modifications are required for the proper folding of pre-rRNA and therefore necessary for pre-ribosome processing. MDN1 is also known to sequentially remove ribosomal factors to mature the pre-60S ribosome in yeast (Bassler & Hurt, 2019; Matsuo et al., 2014). In Hela cells, MDN1 recruited to RIX1 by SUMOylated PELP1 is essential for pre-60S ribosome processing and the cell proliferation (Raman et al., 2016). As a large AAA-type chaperone with 5596 aa residues, MDN1, like its S. pombe orthologue, should undergo a drastic conformational change that consumes ATP to complete pre-ribosome maturation in human cells (Chen et al., 2018).

GNL2 is a 731 amino acid protein with a central GTP-binding domain, and this protein localizes primarily to the nucleolus by using the N-terminal NLS and the C-terminal NOLS (Scott et al., 2010; Scott et al., 2011). The latter also contributes to its nuclear localization (Chennupati et al., 2011). Two *S. cerevisiae* orthologues, NOG2 of human GNL2 and Rea1 of human MDN1 on the 60S pre-ribosomal subunit, remodel the pre-ribosome, with Real1 replacing NOG2 with Nmd3 (human NMD ribosome export adaptor) and then departing from the pre-ribosome. The resulting precursor then leaves the nucleus for the cytoplasm (Klinge & Woolford, 2019; Matsuo et al., 2014). Consumption of GTP and ATP is essential for this remodeling. The authors conclude that Nog2 (GNL2) is a regulatory GTPase that controls 60S pre-ribosome maturation to be replaced by the nuclear export machinery protein during the remodeling (Matsuo et al., 2014).

In the past, we have observed that numerous proteins coimmunoprecipitate with ELMSAN1, which activates and represses genes required for mouse neural differentiation (Mondal et al., 2020) and that the yield of coimmunoprecipitated proteins, such as MKI67, GNL2, MDN1, YTHDC2, CNOT1, and PELP1, was higher than that of ELMSAN1 itself (Iuchi & Paulo, 2021). These proteins together with other coimmunoprecipitated proteins, form a network that is most relevant to RNA metabolism, and we therefore named this group of proteins as the

RNAmetasome network. This network includes some proteins in P- and stress bodies (Riggs et al., 2020; Youn et al., 2019), but the network includes a much larger number of the proteins found in immunoprecipitants performed with an antibody to flag-tagged MKI67 (Sobecki et al., 2016). The RNAmetasome network consists of 11 functional groups, each consisting of several or more proteins, such as RNA polymerases, ribosome proteins, pre-ribosome processing proteins, spliceosome complex, RNA degradation systems, and mitosis-related proteins. However, the most prominent feature of the RNAmetasome network contains MKI67, GNL2, and MDN1 as the major components. Reciprocal co-immunoprecipitation revealed that MKI67 interacts most closely with GNL2, followed by YTHDC2 and MDN1, and most distantly with ELMSNN1. The CCR4-NOT subunit CNOT1 is also one of the proteins that closely interacts with MKI67. Confocal microscopy has shown that both MKI67 and GNL2 are most abundant at the nucleolar periphery, whereas MDN1 is slightly localized with them and the majority is widely distributed in the nucleus (Iuchi & Paulo, 2021). To gain insight into the RNAmetasome network, this research has focused on the mechanism of binding of the MKI67/GNL2/MDN1 complex (MGMc) to the chromosome and the cellular role of this binding. Furthermore, this research has focused on the regulation of gene and protein expression. Consequently, this report presents several discoveries, including the specific binding of MKI67 to chromosomal DNA, the mechanism of MGMc formation and 60S pre-ribosome particle export, MKI67-mediated mRNA degradation and translational repression, the coordination between ribosome biogenesis and energy supply, and the regulation of apoptotic pathways. The distinct binding of MDN1 to POLRIII-dependent RNA genes identified during this research is briefly described in the discussion section. In summary, the results obtained in this study suggest that the presence and absence of MKI67 are both critical for cellular processes. Furthermore, the results indicate that the absence of MKI67 may confer a survival advantage to non-dividing quiescent and differentiated cells.

RESULTS

HEK293T is derived from a neuronal cell lineage

Before describing our current results, we would like to clarify the cell lineage of HEK293T, because the parent cell line HEK293 has been reassigned from a kidney cell lineage to a neuronal cell lineage. Graham et al originally established HEK293 by transforming the embryonic human kidney cells with sheared Ad5 DNA (Graham et al., 1977) and considered HEK293 to be a kidney cell lineage, and this idea was widely accepted. However, 25 years later, the same group reported that HEK293 was derived from human neuronal lineage cells due to the nature of Ad5, which preferentially transforms neuronal cells (Shaw et al., 2002). To ensure that the HEK293T we use inherits the neuronal cell characteristics of HEK293, we submitted our previous MS data (Iuchi & Paulo, 2019) to the STRING database via Cytoscape (Shannon et al., 2003) and investigated what the HEK293T cell lineage looks like. Out of a total of 7811 proteins that we submitted, 7570 proteins were recognized by the database with 99% confidence, and the database showed that these proteins were much more highly expressed in the human nervous system than in any other human

tissue, including the kidney and the adjacent adrenal gland (Supplemental Figure 1). This result has confirmed that HEK293T is a human neuronal lineage cell line. Therefore, we will interpret the data of this report as the results derived from an embryonic neuronal cell lineage.

The MKI67 protein binds to almost the entire genome in conjunction with GNL2 and MDN1, often at heterochromatic sites

We have previously proposed that MKI67, GNL2, and MDN1 form MGMc and that MGMc binds to the human genome through MKI67. Therefore, these three proteins must bind to the same chromosomal sites. To demonstrate this binding, we performed ChIP-Seq twice on samples obtained from proliferating HEK293T cultures. Presentation of the first ChIP-Seq data by bigWig shows that MKI67 binds contiguously to the chromosomes almost everywhere, including centromeres, except for areas that were not mapped, such as the rRNA genes/NORs (Figure 1B top and Supplemental Figure 2). Although the cross-linking conditions of the second ChIP-Seq sample were not necessarily the same as the first ChIP-Seq sample, the second ChIP-Seq shows that MKI67 binds to the exact same areas. Both bigWig plots of the first and second ChIP-Seq show that MKI67 binds more densely to some specific areas of chromosomes, which was found more explicitly on chr1, 7, 9, 13, 18, 21 (Supplemental Figure 2). This tendency is not due to the PCL in mitosis, since the antibody we used essentially does not recognize mitotic MKI67 and our growing cultures contain only 6% mitotic cells (Supplemental Figure 3). To further investigate the binding propensity of MKI67, GNL2, and MDN1, we used bam plots and found that GNL2 binds to the same sites as MKI67 in the first ChIP-Seq. However, unlike GNL2, the reads of the MDN1 in the ChIP-Seq were too low to draw any conclusions. Therefore, we doubled the number of cells for the second ChIP-Seq and extended the formaldehyde crosslinking by 20%. As a result, the reads of MDN1 became higher and showed that MDN1 shares the MKI67 binding sites with GNL2. Thus, these results suggest not only that MKI67, GNL2, and MDN1 form MGMc on the chromosomes, but also that MDN1 binds to MKI67 from a more distal location than GNL2. Unexpectedly, the second ChIP-Seq reduced the GNL2 reads (Figure 1C,D,E), suggesting that MDN1 itself or the 60S pre-ribosomal particle containing MDN1 engulfs GNL2, and thereby blocking the anti-GNL2 antibody from accessing to its epitope. This inverse relationship between GNL2 and MDN1 occurred everywhere, including both genes and intergenic regions (Figure 1C,D,E). In addition, we found that MGMc frequently binds to heterochromatic and semi-heterochromatic regions, including centromeric regions (Figure 1C,D,E). Taken together, we conclude that MGMc binds to chromosomes in the following manner: First, MKI67 binds directly to chromosomes; second, GNL2 binds to the protein; and finally, the MDN1/pre-ribosome particle binds to MKI67 via GNL2. However, it is important to note that the binding of the MDN1/pre-ribosome particles is expected to be relatively short, since most of them are distributed in the nucleus.

We also investigated whether MKI67 binds to promoter regions. The ChIPseeker result shows that MKI67 binds to the TSS, slightly shifted downstream, and additionally binds both upstream and downstream of the TSS (Figure 1F). Binding to the *PGAM1* gene is one such

example (Figure 1E). This binding raises the possibility that MKI67 may act as a regulatory protein at promoters and as a cushion or buffer zone for proteins and RNAs to access to enter and exit the chromatin. On the other hand, GNL2 binds to the TSS in the middle and MDN1 binds to it slightly downstream, suggesting that both GNL2 and MDN1 are associated with transcriptionally relevant events, independent of their role in MGMc. We will discuss this issue in more detail later.

Nucleotide sequence specificity of MKI67 at the centromeres

The objective of the subsequent investigation was to demonstrate the nucleotide sequence specificity of MKI67. To this end, consensus sequences to which MKI67 binds were sought. Using HOMER, we identified 15 candidate sequences consisting of octa-nucleotides with a P value of less than 1E-14 (Supplemental Table 1) across the entire genome. Therefore, MKI67 may bind to these consensus sequences in the nucleus. However, MKI67 appears to bind to much longer nucleotide sequences than any of these octa-nucleotide sequences because it binds through the long C-terminal DNA binding domain consisting of 321 amino acids (Garwain et al., 2021; MacCallum & Hall, 2000; Saiwaki et al., 2005). To identify longer MKI67-binding consensus sequences, we chose to use binding data at the centromeric regions of chr1, chr2, chr3, chr4, chr5, chr7, and chr13, to which MKI67 binds predominantly as single peaks. Notably, each single MKI67 binding peak occupied 50-120bp of DNA, and the median binding length was 80 to 90 bp (Figure 2A,B,C,D,E,F), consistent with our prediction that the 321 AA-long MKI67 C-terminal DNA binding domain can bind to unusually long DNA sequences. Interestingly, however, peak area reads, i.e., the amount of MKI67 in a peak area, are highly variable among centromeres. MKI67 binds most strongly to the chr7 centromere, followed by the chr13 centromere, and least strongly to the chr2 centromere, suggesting that the 50-120 bp sequences at each centromere differ in nucleotide sequence. To identify the consensus sequences to which MKI67 binds, we aligned a group of the top 65 chr7 peaks, consisting of 1986 to 50 reads per peak area. (Supplemental Figure 4). If these peaks contained a target sequence of MKI67, the alignment would yield a consensus sequence. There were two consensus sequences in this high -binding group: the first consensus sequence was present before a characteristic sequence (Figure 2G, Supplemental Figure 4G7lh), 5'-TGTGt/aTGTGTG-3', and the second consensus sequence was present after the sequence (Figure 2H, Supplemental Figure 4H7rh). If these two sequences were indeed MKI67 binding sequences, the same sequences would be found in other chromosome centromeres. Indeed, analogous consensus sequences were found in the chr13 acrocentric centromere. Although these chr13 sequences were not completely identical to the chr7 sequence, 9-10 short identical sequences are included in the two sequences (Figure2G,H) along the entire consensus sequences. In addition to this consensus sequence, MKI67 tends to bind more strongly to the consensus sequences when the sequences contain consecutive T or A such as AAA, AAAA, TTT, and TTTT (Supplemental Figure 4G7lh bottom rows), suggesting that these sequences confer additional affinity to MKI67. Some of these short consensus sequence units are also located in MKI67 weak binding sites, such as sites with 9-11 reads per peak area at the Chr7 centromere. Notably, the number of short binding units in these sites was lower than in the larger binding sites (Figure 2G,H). This again suggests

that the high-capacity consensus sequences have more short consensus sequence units for MKI67 to bind than the low capacity consensus sequences. In contrast to chr13, the centromeres of chr1, chr2, chr3, chr4, and chr5 do not exhibit such a striking resemblance to the consensus sequences of chr7. In the absence of the long consensus sequences at the centromeric regions of these chromatins, MKI67 may bind to sequences comprising different combinations of the short consensus sequence units (motifs), as may be the case at the non-centromeric regions. In summary, the MKI67-binding consensus sequences are composed of multiple short MKI67-binding sequence units, and the greater the number of these binding units present, the greater the amount of MKI67 that binds.

The GNL2 C-terminus is essential in formation of MGMc

The formation of MGMc is a complex process that needs to be elucidated. Since GNL2 is present at the center of MGMc, it may play a critical role in the formation of the complex. Accordingly, we cloned GNL2 cDNA from a HEK293T total RNA and differentially truncated it to identify the region that binds to MKI67 and recruits MDN1 (Figure 3A). The search for the interacting region was initially achieved by coimmunoprecipitation of endogenous MKI67 with antibodies directed against the N- or C-terminal tags of the cloned GNL2. As anticipated, the anti-GFP antibody captured endogenous MKI67 via the EGFP-tagged full-length GNL2 protein (G7 and #1), but not through the empty vector protein (#9) (Figure 3B-top). Upon extending the experiment to encompass C-terminal deletion mutants, it became evident that GNL2 devoid of the C-terminus were incapable of binding to MKI67. Conversely, a pulldown experiment with #8 demonstrated that the C-terminus of GNL2 is responsible for the binding to MKI67. The results with #4, #17, #26, and #18 indicate that the region of GNL2 responsible for binding to MKI67 is limited to the 593-731 AA peptide. The additional result with #5 (full length) and #18 (642-731) suggests that the majority of the binding activity is present in GNL2$^{642\text{-}731}$. The same GNL2 C-termini interacted with MDN1 (Figure 3C). It is noteworthy that the N-terminal region of #10 can alleviate the instability of GNL2$^{642\text{-}731}$.

The next important objective was to determine whether the GNL2 C-terminal peptide (GNL2$^{642\text{-}731}$) exhibited direct binding to both MKI67 and MDN1. To this end, an attempt was made to purify endogenous MKI67 using the GNL2 C-terminus tagged with 6x His, but this was unsuccessful because the endogenous MKI67 itself has an affinity for Pierce Ni-NTA magnetic agarose. Therefore, we took advantage of the affinity of MKI67 for the agarose to separate MKI67 from MDN1 and successfully separated them. We then used both the untreated and treated extracts for a Far Western blot (Figure 3D). Probe #20, which had been affinity purified (Supplemental Figure 5), showed a stronger binding affinity for some of the variously cleaved MKI67 fragments enriched by Ni-NTA magnetic agarose treatment (Figure 3D). In contrast, probe #21 showed a much weaker binding affinity for these fragments. Similarly, probe #20 showed binding to MDN1 (Figure 3E). However, in this case, probe #21 showed no binding to MDN1. These results demonstrate that GNL2$^{643\text{-}731}$ binds directly to MKI67 and MDN1.

This conclusion raised the next question that needed to be answered, how GNL2 can simultaneously bind to MKI67 and MDN1 via GNL2643-731. Fortunately, we found the clue, i.e., immunoprecipitants of the full-length GNL2 (G7) contained the unusually high levels of the C-terminal fragments (Figure 3B, middle and bottom panels), and conversely, the fresh cell lysates, in which the GNL2 was considerably stable, contained much less of the C-terminal fragments (Figure 3F). This observation suggests that the full-length GNL2 was highly cleaved at different sites in the nuclear extracts, and the fragmented C-termini bound to the undigested GNL2 (Figure 3F right), or that the full-length GNL2 dimers or oligomers formed at the C-terminus were more resistant to proteolysis. To confirm that this C-terminus-C-terminus binding, far western blots were performed (Figure 3G) using ectopically expressed and immunoprecipitated EGFP-GNL2 (#1) and C-terminus deleted mutants were used prays, and purified #20 was used as the probe. As a result, #20 bound to full-length GNL2 (#1) but not to any of the mutants, demonstrating that GNL2 forms a homodimer or oligomer at the C-terminus. In addition, this result suggests that binding of the GNL2$^{469\text{-}555}$ fragment binds to yet unidentified cellular proteins, rendering GNL2 resistant to the proteolysis.

Finally, we employed confocal microscopy to confirm that the C-terminal dimers/multimers are responsible for binding to MKI67 at the anticipated subcellular compartment. #8 containing the C-terminal 642-731 colocalized perfectly with MKI67 at the nucleolar periphery (Figure 3H). In addition, #4, which possesses a C-terminal region that partially overlaps the 642-731 region, colocalized with MKI67 at the periphery to a lesser extent. Full-length GNL2 (G7 and #1) colocalized with the MKI67, although it also localized to the center of the nucleolus separately from MKI67. The observed discrepancy in the localization of the two full-length GNL2 is likely attributable to overexpression and the cleaved EGFP N-terminus. The evidence from these images suggests that the C-terminal 642-731 region of GNL2 binds to MKI67 and MDN1 predominantly at the nucleolar periphery. It is noteworthy that EGFP-GNL2$^{1\text{-}223}$ (#2) and EGFP-6x His (#9) enter the nucleolus without being concentrated, suggesting that proteins with molecular mass less than 50 kDa diffuse into the nucleolus.

MKI67, together with GNL2 and MDN1, regulates 60S pre-ribosome export from the nucleolar periphery

MKI67 depletion resulted in a reduction in cell size, a change in the shape of nucleoli from irregular to spherical, and a decrease in the amount of high-density chromatin (heterochromatin) at the nucleolar periphery compared to that of the control cells (Figure 4A-12,16; B; Supplemental Figure 6). Furthermore, the KD simultaneously distributed high-density throughout the nucleus, as previously observed by another group (Sobecki et al., 2016), indicating that MKI67 is required to maintain high-density chromatins at the periphery.

Next, we investigated the role of MKI67 on the localization of GNL2 and MDN1. Depletion of MKI67 decreased the levels of both GNL2 and MDN1 in the nucleolus and adjacent nuclear zone, while increasing them in the nuclear periphery and the cytoplasm; consequently, MKI67 depletion caused 60S pre-ribosome particles to leak out of the nucleolar periphery (Figure

4A9-16, C and D). These results suggest that MKI67 at the nucleolar periphery serves to retain the 60S pre-ribosome particles for some time during its processing. Conversely, we investigated the role of GNL2 and MDN1 on MKI67 localization. Interestingly, depletion of GNL2 resulted in increased levels of MKI67 at the nucleolar periphery (Figure 4A17-18; E), and similarly, depletion of MDN1 resulted in increased levels of MKI67 (Figure 4A25-26). Therefore, we conclude that both GNL2 and MDN1 play a role in the turnover of the peripheral MKI67, and further that MDN1 plays a direct role in the segregation of the MKI67 layer, as the recruitment of MDN1 to the periphery by GNL2 was essential for the turnover. Next, we investigated how GNL2 and MDN1 behave upon depletion of either protein. Upon depletion of GNL2, MDN1 accumulated in the nucleolus while still translocating into the nucleus (Figure 4A21-22, G). In contrast, upon depletion of MDN1, GNL2 was predominantly retained at the periphery (Figure 4A29-31, F). These results are consistent with the putative roles of MKI67 as a barrier and of MDN1 as an executor of 60s pre-ribosome export. The indecisive phenotype of MDN1 upon GNL2 depletion may result from depletion of GNL2, which can serve as both a recruiter of MDN1 and a supporter of the MKI67 barrier.

To confirm this assertion for the roles of MKI67, GNL2, and MDN1, we examined the behavior of PELP1, another 60S pre-ribosomal subunit that directly interacts with MDN1 (Castle et al., 2010; Finkbeiner et al., 2011; Raman et al., 2016). As anticipated, PELP1 was more abundant at the nuclear periphery in the MKI67-depleted cells than in the control cells and more abundant in the nucleolus in the GNL2-depleted cells although it can still translocate into the nucleus (Figure 4H). Notably, PELP1 was much more abundant at the nucleolar periphery than any other compartment in the MDN1-depleted cells, suggesting that PELP1 remained at the periphery and was mostly unable to translocate through the MKI67 layer due to depletion of MDN1. This result strengthens our conclusion regarding the function of the MGMc subunits in 60S pre-ribosome particle export, especially regarding the direct involvement of MDN1 in the 60S pre-ribosome export. The role of MGMc is illustrated in Figure 4I.

Depletion of MDN1 results in a much stronger downregulation of transcripts of RNA genes required for ribosome processing and splicing compared to depletion of MKI67 or GNL2

What functions do MKI67, GNL2, and MDN1 have beyond the export of pre-ribosome particles? Our findings that these proteins bind to numerous sites on chromosomes (Figure 1B and Supplemental Figure 2) and frequently to heterochromatin regions including centromeres (Figure 1C,D) predicts that MKI67, GNL2, and MDN1 likely regulate gene and protein expression. Therefore, to elucidate the regulatory roles of these three proteins, we performed RNA-seq with triplicate cultures and quantified the severity of depletion first and then observed
the effect on genomic transcript levels under the same conditions. Each KD reduced its transcript levels by 70-80% (Figure 5A) and its cognate proteins to a similar extent or greater extent (Figure 5B). In addition, the results of KD-MKI67 also had a peculiar aspect, i.e., depletion of MKI67 increased MDN1 transcript levels by 20%, but conversely decreased MDN1 protein by 40%. As a result, KD of each gene essentially exerts its effect via specific depletion of MKI67, GNL2, or

MDN1; however, KD-MKI67 may also exert some of its effects via reduced levels of MDN1. The lower levels of MDN1 upon MKI67 depletion may be due to the leakage of pre-ribosome particles into the cytoplasm (Figure 4A, panel 14).

The results of the RNA-seq demonstrated that each depletion resulted in the up- and down-regulation of transcripts of numerous genes (Supplemental Figure 7 top three). From these data, we identified the names of transcripts whose levels changed by a factor of 2 or more (Supplemental Table 2A-C), resulting in a total of 6 groups. We then entered the names in each group into Metascape (Zhou et al., 2019). As a result, we found that the many transcripts in the same category/pathway behaved similarly across the three depletions (Figure 5C,D,E,F,G,H). For example, transcripts associated with the ribosome and ribosome biogenesis categories were downregulated by depletion of each of the three proteins (Figure 5C,D,E). However, in this category, depletion of MDN1 most strongly reduced the levels of transcripts, including MT-RNA1, MT-RNA2, RNA5, RNA5.8S, SNORA, RNU1, and RNU5 (Figure 5I and Supplemental Figure 7 bottom). This observation suggests that MDN1 is essential for mitochondrial and cellular ribosome processing and splicing of RNAs. Among these reduced RNAs, the reduction of many SNORA (H/ACA-type snoRNAs) and some SNORDs (Figure 5J) is particularly noteworthy, as this reduction can lead to the failure of the tertiary structure of target RNAs, such as rRNA, tRNA, and snRNA (Webster & Ghalei, 2023). This may be the most influential cause of the block in the processing of 60S pre-ribosome particles. Interestingly, depletion of MDN1 or GNL2 increased both HSPA1A and HSPA1B transcripts approximately 2 to 3-fold (Supplemental Table 2B,C), suggesting that a link between these heat shock proteins and pre-ribosome processing. In contrast, MKI67 depletion is not involved in the regulation of SNORs (Figure 5J) or HSPA1A and HSPA1B (Supplemental Table 2A).

Depletion of MKI67 upregulates various protein-coding transcripts including those of neurons.

Depletion of MKI67, GNL2, and MDN1 increased numerous transcripts. Notably, depletion of MKI67 increased more than100 transcripts to the greatest extent and in the broadest category (Figure 5F,G,H and Supplemental Table 2A-C). Specifically, this depletion resulted in the placement of 24 neuronal cell-specific transcripts at the top of the top 55-transcript list. These transcripts, such as ACTL6B43 (Bell et al., 2019) and SCN3B (Wang et al., 2017), primarily play a role in the presynapse. Regarding the loci of these 55 genes, 30 genes were located in the 15 heterochromatic and the 15 semi-heterochromatic regions, while the 17 genes were located in the euchromatic regions. This observation suggests that the 30 genes, which include many genes of the neuronal cell-specific transcripts, are likely to be silenced by heterochromatin-mediated mechanisms in the proliferating cells, whereas the 17 genes are downregulated by some other mechanisms. The remaining 8 genes were not mapped.

The subsequent objective was to ascertain the mechanism involved in the regulation of the transcript levels. To this end, the *NEK7* and *UNC13A* transcripts were selected. The genes of these transcripts were located in euchromatic regions, and the levels (baseMean) of these transcripts

were markedly higher than those of the genes located in heterochromatic and semi-heterochromatic regions. First, we analyzed the *NEK7* transcript, which is required for nucleation of mitotic microtubules at the centrosome (Kim et al., 2007). Depletion of either YTHDC2 or CNOT1 resulted in a 2- to 3-fold increase in the NEK7 protein (Figure 6A, see Supplemental Figure 8 for the entire Western blot image). However, neither of these incremental effects was observed beyond the increase by MKI67 depletion when these depletions were combined with that of MKI67 (Figure 6D). Similarly, depletion of G3BP1 increased NEK7 protein to a comparable extent, yet the elevated levels never exceeded those brought about by depletion of MKI67 (Figure 6H). It is noteworthy that the extent of the increase brought about by MKI67 depletion is approximately equal to the sum of the increases observed with each depletion of YTHDC2, CNOT1, and G3BP1. These results suggest that MKI67 on the chromatins binds the *NEK7* transcripts through the LLPS propensity (Figure 1) (Iuchi & Paulo, 2021) and transfers them to YTHDC2, CNOT1, and G3BP1 for degradation (Figure 6L-1,-2), and also suggests that MKI67 transfers the *NEK* transcript to G3BP1 for an additional role, that is, retention of the RNA until the NEK protein is required. This regulatory mechanism of the *NEK7* transcripts further suggests the possibility that other transcripts are similarly regulated, since MKI67 binds almost the entire chromatin.

On the other hand, as shown in Figure 7A (see Supplemental Figure 9 for the entire Western blot image), neither YTHDC2 nor CNOT1 depletion altered the level of UNC13A protein, which is known to be expressed in the brain and functions to prime presynaptic neuronal vesicles for calcium ion-dependent depolarization signaling (Willemse et al., 2023). In addition, no response of UNC13A to MKI67 depletion was observed, in contrast to its transcript response, suggesting that the *UNC13A* transcripts are immediately converted to a non-translational form via a mechanism of local translation. Therefore, we investigated the possibility that G3BP1 and G3BP2 are involved in trapping the *UNC13A* transcript and minimizing its translation, since both are known to be involved in local translation in neurons in addition to degradation of transcripts in stress bodies (Dar et al., 2024; Kipper et al., 2022; Sidibe et al., 2021); however, this investigation ended up with the result that neither G3BP1 nor G3BP2 depletion was able to increase UNC13A protein levels, regardless of the combination with MKI67 depletion (Figure 7B,D,F). We therefore investigated the last possibility, i.e., the involvement of FMR1 (Richter & Zhao, 2021) and found that depletion of this protein marginally increased translation of the *UNC13A* transcripts (Figure 7H,I). However, given the lack of response of UNC13A protein synthesis to MKI67 depletion, the observed result does not reveal how strongly FMR1 is involved in controlling UNC13A translation. The discrepancy between the responses of the UNC13A transcripts and the protein to MKI67 depletion may be due to the lack of local translation in HEK293T cells, which do not form axons and dendrites.

MKI67 upregulates transcripts involved in respiration transcripts, while MDN1 upregulates both ribosome biogenesis and respiration transcript levels

During gene knockdown experiments, we observed that depletion of either MKI67 or MDN1 resulted in more acidic cultures than the control cultures, whereas depletion of GNL2 did not. The acidification began 2 days after these protein depletions and continued for 3 days (Figure 8A), indicating that there are common metabolic changes in both MKI67-depleted and MDN1-depleted cultures. A more detailed examination of the pathways revealed that transcripts of the electron transport system at the complex III, cytochrome C, and complex IV decreased in both depletions, although not always the same transcripts. MKI67 depletion reduced transcripts of UQCRQ, UQCRH, UQCRHL, UQCR11, COX5B, and COX8A (Figure 8B, C, D, Supplemental Table 4), whereas MDN1 depletion reduced transcripts of UQCRHL, CYCS, and COX6C. The reduction in each transcript was relatively modest, ranging from 1.5 to 2-fold. However, the collective impact of these reductions should have resulted in a considerable impairment of the electron transport system, leading to a depletion of ATP and a reduction in the NAD+/NADH ratio. Notably, MDN1 depletion resulted in defects in both pre-ribosome processing and the electron transport system (Figure 5I, Figure 8). These results indicate that MDN1 regulates the electron transport system to ensure that the sufficient energy is available to meet the demands of pre-ribosome processing when needed. This phenomenon is analogous to the coordinated regulation of energy consumption and ribosome biogenesis controlled by eNoSC (energy-dependent nucleolar silencing complex), in which SIRT1 of the complex is postulated to be activated by the high NAD+/NADH ratio under glucose deprivation. This results in the shutdown of the rRNA gene expression by deacetylation of H3K9, possibly by a yet unknown protein, followed by dimethylation of H3K9 by SUV39H1 (Murayama et al., 2008). However, the regulatory mechanism underlying the process triggered by MDN1 depletion is reversed in the primary and secondary pathways for the eNoSC system. The primary target of MDN1 is the pre-ribosome processing, and the secondary targets are components of the electron transport system complexes III and IV, and CYCS. Moreover, MDN1 depletion is predicted to diminish the NAD+/NADH ratio, since NADH levels would be elevated at complex I due to reduced downstream metabolism. Thus, two different mechanisms govern the coordination between pre-ribosome processing and energy supply pathways. The substantial reduction in MT-RNA2 (Figure 5I), which is also known to be a crucial component in the escape from apoptosis (Guo et al., 2003), may be the primary cause of the reduction in respiration. With respect to glucose consumption, the RNA-seq data indicate that MDN1 depletion appears to consume more glucose than the control, whereas MKI67 depletion tended to consume less glucose than the control (Figure 8B and Supplemental Table 4).

Notably, depletion of either MKI67 or MDN1 resulted in the upregulation of phosphoglyceraldehyde mutases (PGAM1 and PGAM2), which enhances the adaptability of the glucose pathway to either cellular conditions requiring either increased glucose consumption or increased gluconeogenesis to replenish the pentose cycle. This increase in PGAMs appears to provide MKI67-depleted cells with the potential to produce sufficient nucleotides for continued proliferation.

DISCUSSION

The binding of GNL2 and MDN1 to promoter regions

As described above, GNL2 and MDN1 bind to promoter regions independently of MKI67. GNL2 binds to the 5' regions of protein-coding genes, including ZMPSTE24 and TBC1D13 (Supplemental Figure 10A,B). Depletion of GNL2 resulted in a 1.64-fold upregulation of ZMPSTE24 and a 0.67-fold downregulation of TBC1D13. This regulatory range was less extensive than that observed in other transcripts of genes whose promoters were not bound by GNL2 (Supplemental Figure 10C,D). Consequently, we deduce that GNL2 plays a role in transcription at these promoters, although it is more of an auxiliary factor.

MDN1 binds to the 5' regions of genes, including not only protein-coding genes, such as *DAB2IP*, *PAK4*, *RFX1*, and *SGSM1* (Supplemental Figure 11A,B), but also RNA genes, such as the small Y-RNA genes (*RNY1, 3, 4*), the *RNU6* genes, and the long-noncoding genes (*RMRP* and *RN7SK*) (Supplemental Figure 11C,D,E,F). The *RNA6* genes are of particular interest, as they are the only genes transcribed by POLRIII among all the snRNAs involved in spliceosome formation, and as the transcripts of these *RNU6* genes are the most critical factor, capable of recruiting Mg ions and cleaving the target pre-mRNA (Wilkinson et al., 2020). *Y-RNA*, *RMRP*, and *RN7SK*, are also transcribed by POLRIII (Dergai & Hernandez, 2019). The MDN1 binding to these gene promoter regions was 10-fold or higher than the binding to protein-coding genes, yet depletion of MDN1 did not result in evident changes in transcript levels (Supplemental Figure 12). These observations suggest that MDN1 is not a conventional transcription factor, but rather, has a different role. Furthermore, MDN1 exhibits a unique binding pattern, binding to the 5' and 3' ends of genes, albeit with reduced affinity at the 3' ends. An extreme example of this characteristic MDN1 binding was observed at the *RMPR* (Supplemental Figure 11D), where MDN1 covers the entire gene. These trends suggest that MDN1 plays a role in stabilizing these transcripts or in forming the necessary tertiary structure immediately after transcription. Alternatively, MDN1 may have the capability to select POLRIII, which terminates transcription at the desired position of the target RNA genes, over POLRII (Dergai & Hernandez, 2019; Duttke, 2014; Lobo & Hernandez, 1989; Wilkinson et al., 2020).

Benefit from the absence of the MKI67 in differentiated quiescent cells

As described above, chr-MGMc plays a role in regulating the release of pre-ribosome particles. Therefore, its structure and function are of great importance to the cells, and the nucleolar export of 60S pre-ribosome even appears to be an integral part of pre-ribosome processing. However, MKI67 depletion does not inhibit cell proliferation (Garwain et al., 2021; Iuchi & Paulo, 2021; Sobecki et al., 2016), nor does it reduce the rRNA levels (Sobecki et al., 2016). Conversely, depletion of MDN1 or a RIX1 subunit arrests cell proliferation in G1 through the PT53 system (Castle et al., 2012; Castle et al., 2010; Raman et al., 2016), and similarly, GNL2 depletion retards cell proliferation (Iuchi & Paulo, 2021). Therefore, the underlying mechanism of this phenomenon in MKI67-depleted cells is unique and remains to be elucidated. Given the large amount of RNA-seq data are now available on this topic, we can postulate a hypothesis to explain this phenomenon. The hypothesis is that depletion of MKI67 in the nucleolar periphery must be detrimental to the

cells and induce intrinsic apoptosis due to colossal DNA damage (Booth et al., 2014; Garwain et al., 2021); and therefore, the ability of the MKI67-depleted cells to continuously proliferate must be due to a concurrent compensation induced simultaneously by MKI67 deletion. Since we already know that MKI67 depletion alters intrinsic apoptotic signaling pathways (Figure 5C), we sought to identify specific apoptosis-related transcripts involved in the compensation process. This analysis revealed that eleven such transcripts were either up- or down-regulated among numerous apoptosis-related transcripts (Figure 9A,B and Supplemental Table 3). Among them, two anti-apoptotic transcripts, AVEN and XIAP, were upregulated, and eight pro-apoptotic transcripts, BAD, FAIM, BNIPL3, BNIP3, DDIT, and TP53 (Bensaad et al., 2006; Cancer Genome Atlas Research, 2014; Czabotar & Garcia-Saez, 2023; Diana & Carvalheira, 2022) were downregulated. In contrast, no change in the expression of these transcripts was observed in GNL2- and MDN1-depleted cells. Moreover, the levels of the PIK3R and arginine transporter transcripts, including PIK3R3 and SLC7As (Spears et al., 2023; Yu & Cui, 2016), were increased by MKI67 depletion, whereas the levels of these proteins were not increased by GNL2 or MDN1 depletion (Figure 9C,D), suggesting that MKI67-depleted cells have a higher potential to synthesize macromolecules required for proliferation via the mTOR activation through the higher expression of transcripts, such as those of the arginine transporters. These two lines of evidence provide a rational basis that MKI67 depletion not only enables the cells to escape apoptosis, but also enables the cells to promote proliferation. They further suggest that differentiated quiescent cells also similarly escape from cell death by MKI67 depletion and survive for a longer period while maintaining the functions conferred to differentiated cells. This mechanism may be particularly important in neurons.

METHODS

Cell culture.

HEK293T (ATCC CRL-3216) was cultivated in DMEM (Thermo Fisher Scientific) supplemented with 10% fetal bovine serum (HyClone). The cultivation and the handling procedures of this cell line have been approved by Harvard University Committee on Microbiological Safety (ID: 20-155). All experiments were conducted in accordance with the NIH rDNA and the Federal Occupational Safety and Health Administration Bloodborne Pathogen Standard Guidelines.

Cloning of the *GNL2* cDNA and its truncation.

Total RNA was purified from HEK293T cultures, and the first strand cDNA was synthesized from 600 ng total RNA using the ProtoScript II Kit (NEB, E6560S). From the cDNA, the cDNA encoding GNL2 (Q13823) was amplified using Q5 Hot Start High-Fidelity DNA Polymerase (NEB, M0494S). This product was then cloned into the ECORI-SCAII site of pEGFP-C2, yielding pGNL2-G7, which encodes GNL2 tagged with EGFP and 6x His at the N- and C-termini, respectively (Figure 3A). The 6x His tag was removed, yielding pGNL2-#1, and then these two plasmids encoding full-length GNL2 were differentially truncated using Q5 Site-Directed Mutagenesis Kit (NEB). Similarly, G7 and the fragments were amplified or truncated and ligated to pGEX-5X-1 at the ECORI-XhoI site to yield bacterial expression plasmids. All oligonucleotides

used in this cloning, truncation (purchased from IDT), and related plasmid construction information are listed in Supplemental Table 5.

Knockdown (KD) of genes

HEK293T culture was transfected with gene-specific DsiRNA (double-stranded RNA for gene knockdown, IDT) at 40 nM concentration according to the reverse transfection protocol of Lipofectamine RNAiMAX (ThermoFisher) to knockdown the MKI67, the GNL2, and the MDN1, the YTHDC2, the CNOT1, the G3BP1, the G3BP2, or the FMR1genes. Similarly, the HEH293T culture was transfected with the universal negative control (NC1) to make the control cultures. These transfected cultures were incubated for 70 h and then harvested to determine the knockdown consequence. These treated cells were mostly cultured in 12-well plates, but they were also cultured in 35-mm Matsunami glass-bottom dishes for cytological work. The DsiRNAs used in this study are summarized in Supplemental Table 6.

Western blotting to analyze the cellular interaction of GNL2 with endogenous MKI67 and MDN1 and to analyze the consequence of KD

To investigate the native protein-protein interaction, HEK293T cells grown in a 10-cm dish were transfected with 10 µg of plasmid encoding full-length GNL2 or its truncated protein using X-tremeGENE 9 DNA transfection reagent (Sigma) and cultured for 2 days. Nuclear extracts were prepared from the cultures as previously described (Iuchi & Paulo, 2021) in the nuclear extraction buffers supplemented with 10 µM BTZ (Bortezomib, AdipoGen LIFE SCIENCES, AG-CR1-3602). Nuclear extracts (300 µl) were pre-cleared with 20 µl of a mixture of protein A magnetic beads and protein G magnetic beads for 60 min. The precleared nuclear extracts were incubated with 3 µg of r-anti-GFP antibody or 3 µg of m-anti-6x His antibody for 60 min and further incubated for 70 min after addition of 20 µl of the mixture of protein A and protein G magnetic beads. The beads were washed 4 times with 300 µl of the nuclear extraction buffer containing 10 µM BTZ, suspended in 30 µl of 1.5x loading buffer, and heated at 100C for 5 min. Ten µl of the supernatant was applied to one well of 4–20% Mini-PROTEAN TGX gels (BIO-RAD, 4561096) for electrophoresis. Immunoprecipitants in the gel were transferred to a PVDF membrane for Western blot. Proteins on the membrane were detected by Western blotting using antibodies at the concentrations described in Supplemental Table 7. To investigate the effect of gene KD, KD cultures were trypsinized and collected in 1.5 ml centrifuge tubes and washed twice with PBS/1x Complete EDTA-free protease inhibitor cocktail (Roche). Cell pellets were resuspended in 30 µl of hypotonic lysis buffer, kept on ice for 20 min and subjected to two freeze-thaw cycles. The cell lysates were then used as cell extracts. Cellular proteins were estimated using the Micro BCA kit (Fisher Scientific), and a 50 µg protein sample was loaded into one well of 4–20% Mini-PROTEAN TGX gels (BIO-RAD 4561094). The loaded proteins were separated by PAGE and then transferred to a PVDF membrane for Western blot.

Far western for in vitro protein-protein interaction analysis

A prey sample was loaded, separated by SDS-PAGE, and transferred to a PVDF membrane. The membrane was immersed in 20 ml of 6 M guanidine-HCl solution and incubated for 10 min. The membrane was then transferred to a half concentration of guanidine-HCl diluted in basic buffer

(Iuchi and Joao) and incubated for 10 min. This transfer followed by 10-min incubation was repeated 6 times to slowly decrease the guanidine concentration to less than 100 mM. The membrane was washed twice with PBS, blocked with Li-COR blocking solution for 1 h, and incubated with a probe for 2 h at RT. After four washes with PBS /0.1% Tween 20, the membrane was subjected to Western blotting for double protein staining with m-anti 6x His and r-anti MKI67, m-anti 6x His and r-anti MDN1, or m-anti 6x His and r-anti GFP. When necessary, two sets of prey were prepared on a PVDF, and the PVDF membrane was cut into two pieces, each with an equal set of prey lanes. One half of the membrane was then probed with purified #20 and the other half with purified #21, the amounts of which were estimated to be equal between the two by Western blotting using m-anti 6x His (1.1 x106 Li-COR units).

Confocal microscopy

Cultures grown on Matsunami glass-bottom dishes were removed from a CO2 incubator, rinsed once with serum- and antibiotic-free DMEM, and fixed with 4% paraformaldehyde/PBS for 10 min. Fixation was terminated with 3x PBS, followed by replacement with 1x PBS. Fixed cultures were sequentially dehydrated through 50, 75, 95, and 100% ethanol, and finally air dried. Cells were permeabilized with 0.2% Triton X-100/PBS for 10 min and blocked with 1x PBS/ 5% BSA/0.1% IGEPAL CA630 for 5 min or longer. These ready-to-go samples were typically double stained with mouse and rabbit primary antibodies in the blocking buffer at 4C for 16-18 h, and washed four times with the blocking buffer. They were further stained with two goat secondary antibodies against mouse IgG and rabbit IgG in the blocking buffer for 1.5 h at room temperature, washed three times and rinsed with water, and air dried. These samples were treated with DAPI-containing Vectashield (Vector) and examined with a confocal microscope, Lucille spinning disk & FR, at the CITE at Harvard Medical School. Immunofluorescence images were acquired by capturing the emission from the excitation of Alexa Fluor 555 (red) and Alexa Fluor 488 (green) dyes and the emission of DAPI, respectively, and acquired images of a field were presented separately or merged. Z-plane images of a cell (or culture field) were taken every 0.2 µm, and these images, which cut through the center of the nucleolus, were used for comparison between different culture conditions. The acquired images were visualized and analyzed using Fiji (Schindelin et al., 2012).

Probe preparation

E. coli strain (NEB C3013) was transformed with plasmid #20, #21, or #22, and grown in 30 ml of LB/100-µg/ml carbenicillin and induced with 0.5 mM IPTG for 4 h for production of the encoded protein. The cells were pelleted by centrifugation and suspended in 0.3 ml of 150 mM NaCl/25 mM Na-phosphate buffer (p8.0)/2x Complete (EDTA-free)/1mM PMSF/0.5-mg/ml lysozyme, once frozen and thawed, and sonicated twice for 5 sec at 50% output power. The extract was centrifuged at 14000 rpm for 10 min and the supernatant was mixed with Triton X-100 to 0.05%. Two hundred and fifty µl of the extract were mixed with an equal volume equilibration buffer (50 mM sodium phosphate/0.3 M NaCl/10 mM imidazole/0.05% Tween 20, pH 8.0) and applied to on 50 µl of Ni-NTA magnetic agarose (Thermo Scientific 78605) that had been previously washed three times washed and diluted twofold. This agarose-extract mixture was

rotated at 4C for 1 h, washed four times with 250 µl of wash buffer (50 mM sodium phosphate/0.3 M NaCl/15 mM imidazole/0.05% Tween 20, pH 8.0), and the bound probe was eluted once with 50 µl of elution buffer A (50 mM sodium phosphate/0.3 M NaCl/0.1 M imidazole, pH 8.0). The remaining probe on the beads was eluted twice with 50 µl of elution buffer B (50 mM sodium phosphate/0.3 M NaCl/0.3 M imidazole, pH 8.0). The last two elutes were combined and used as the probe for the Western blot.

Preparation of protein samples from KD cultures

Cultures grown on 12-well plates were rinsed once with PBS and trypsinized with 500 µl of 0.025% trypsin/0.26 mM EDTA solution for 5 min, and the trypsinization was terminated by adding 500 µl of the fresh medium. The cell suspensions were transferred to 1.5-ml centrifuge tubes, washed twice with 500 µl of PBS/1x EDTA-free protease inhibitor cocktail at 4C, and resuspended in 30 µl of hypotonic lysis buffer (10 mM KCl/10 mM HEPES (pH 7.4)/0.05% IGEPAL CA-630/0.2 mM sodium orthovanadate/2x EDTA-free protease inhibitor cocktail/2-µl/ml benzonase/2 mM MgCl2). The suspensions were placed on ice for 20 min, and then frozen and thawed twice, which was used as cell lysates.

Protein samples for MS analysis

Each of four protein samples (approximately 100 µg protein) prepared as described above from duplicate KD-MKI67 and KD-CTL cultures was mixed with 10-volumes of cold 10%TCA/acetone, vortexed, and placed in a -20C freezer overnight. Precipitated proteins were collected by centrifugation at 15,000 rpm for 10 min at 4C and resuspended in 10-volumes of cold acetone of the original sample, vortexed, placed on ice for 10 min, and centrifuged at 15,000 rpm for 5 min at 4C. Proteins were washed with the 10 volumes of cold methanol of the original sample and air dried for 15 min. The samples were digested in 100µL of 100 mM EPPS, pH 8.5 and at 37°C with trypsin at a 100:1 protein-to-protease ratio overnight. The samples were desalted via StageTip, dried via vacuum centrifugation, and reconstituted in 5% acetonitrile, 5% formic acid for LC-MS/MS processing.

Mass spectrometric data collection. Mass spectrometry data were collected using a Exploris 480 mass spectrometer (Thermo Fisher Scientific, San Jose, CA) coupled with a Proxeon 1200 Liquid Chromatograph (Thermo Fisher Scientific). Peptides were separated on a 100 µm inner diameter microcapillary column packed with ~25 cm of Accucore C18 resin (2.6 µm, 150 Å, Thermo Fisher Scientific). We loaded ~1 µg onto the column.

Peptides were separated using a 90min gradient of 3 to 22% acetonitrile in 0.125% formic acid with a flow rate of 350 nL/min. The scan sequence began with an Orbitrap MS^1 spectrum with the following parameters: resolution 60,000, scan range 350−1350 Th, automatic gain control (AGC) target “standard”, maximum injection time “auto”, RF lens setting 50%, and centroid spectrum data type. We selected the top twenty precursors for MS^2 analysis which consisted of HCD high-energy collision dissociation with the following parameters: resolution 15,000, AGC was set at “standard”, maximum injection time “auto”, isolation window 1.2 Th, normalized collision energy (NCE) 28, and centroid spectrum data type. In addition, unassigned and singly charged species were excluded from MS^2 analysis and dynamic exclusion was set to 90 s. Each

sample was run twice, once with a FAIMS compensation voltage (CV) set of −40/−60/−80 V, and the second with a CV set of −30/−50/−70 V. A 1 s TopSpeed cycle was used for each CV.

Mass spectrometric data analysis.

Mass spectra were processed using a Comet-based in-house software pipeline. MS spectra were converted to mzXML using a modified version of ReAdW.exe. Database searching included all entries from the humanUniProt database (downloaded September 2023), which was concatenated with a reverse database composed of all protein sequences in reversed order. Searches were performed using a 50-ppm precursor ion tolerance. Product ion tolerance was set to 0.03 Th. Oxidation of methionine residues (+15.9949 Da) was set as a variable modification.

Peptide spectral matches (PSMs) were altered to a 1% FDR (Elias & Gygi, 2007, 2010*)*. PSM filtering was performed using a linear discriminant analysis, as described previously (Huttlin et al., 2010), while considering the following parameters: XCorr, ΔCn, missed cleavages, peptide length, charge state, and precursor mass accuracy. Peptide-spectral matches were identified, quantified, and collapsed to a 1% FDR and then further collapsed to a final protein-level FDR of 1%. Furthermore, protein assembly was guided by principles of parsimony to produce the smallest set of proteins necessary to account for all observed peptides. Spectral counts were then extracted, and the data were subsequently analyzed.

ChIP-Seq

A HEK293T culture was grown to a density of approximately 5 x 10^7 cells in a 15-cm dish. The cells were then washed once with cold PBS and subsequently crosslinked with 300 mM EGS (Thermo Fisher Scientific) in PBS for 30 minutes. This was followed by a second crosslinking step with 1% formaldehyde. The crosslinking reaction was terminated by a 5-minute incubation with 125 mM glycine, after which the cells were washed and suspended in 3 ml of PBS and transferred to a centrifuge. This collection procedure was repeated to obtain as many cells as possible. The crosslinked cells were once washed with PBS, suspended in 400 µl of lysis buffer (50 mM HEPES-KOH pH8.0/140 mM NaCl/1 mM EDTA pH8/1% Triton X-100/0.1% Sodium Deoxycholate/0.5% SDS/10 µM BTZ), placed on ice for 10 min, and then sonicated for 10 seconds at one-minute intervals on ice under 30% output power using a Branson sonicator. The general ChIP-Seq procedure was conducted as described above, but two distinct operating conditions were employed for the preparation of crosslinked samples: 1) Eleven cycles of sonication were performed on 5 x 10^7 cells that had been treated with formaldehyde for 10 minutes; 2) Thirteen cycles of sonication were performed on 10 x 10^7 cells that had been treated with formaldehyde for 12 minutes. The prepared extract was diluted fivefold with dilution buffer (lysis buffer lacking SDS) and centrifuged at 14,000 rpm for 10 minutes. The supernatants were precleared with a mixture of protein A and protein G magnetic beads (NEB) at 4°C for one hour. Thereafter, the supernatant was distributed into four parts. Subsequently, each supernatant was supplemented with 4 µg of rabbit anti-MKI67, rabbit anti-GNL2, rabbit anti-MDN1, or rabbit anti-GFP (serving as the control) and 60 µl of the protein A and protein G magnetic beads mixture and rotated at 4°C for 16 hours for immunoprecipitation. The beads were washed three times with 500 µl of a high-salt

buffe (50mM HEPES-KOH pH 8/500 mM NaCl/1 mM EDTA/1% Triton100/0.1% SDS/0.1% Sodium Deoxycholate), washed once with 500 µL of LiCl high salt buffer (50mM HEPES-KOH pH 8/250 mM LiCl/1 mM EDTA/1% Triton100/0.1% Sodium Deoxycholate), and then suspended in 100 µl of elution buffer (50 mM Tris HCl/10 mM EDTA/1% SDS). The crosslinked DNA-protein samples were eluted by incubating the beads at 65C for 5 min, and the crosslink of the sample was removed by incubation at 65C overnight in the presence of 1 µl RNase A (20 mg/ml, NEB). Then, proteins in the sample were digested with 2 µl proteinase K (800 u/ ml, NEB) for 1 h at 55C. Thereafter, the DNA fragments of the sample were purified using NEB PCR & DNA Cleanup Kit and dissolved in TE buffer. The concentration of the DNA fragments was determined using a Qubit fluorometer (Invitrogen). From these collected DNA fragments (20 µg), a sequencing library was prepared using the NEBNext Ultra II DNA Library Prep Kit for Illumina (NEB E7645) and treated with NEBNext Sample Purification Beads (E71044S) on two occasions during the procedure, once for the removal of the adapter and once for the cleanup of the end-product. The High Sensitivity D1000 ScreenTapes analysis demonstrated that the end-product contained DNA fragments with an average length of 400 bp and had no evidence of contamination from the adapter. This end-product library was subsequently sequenced for the 50-bp paired-end reads on an Illumina NextSeq 2000 sequencer at the Biopolymers Facilities at Harvard Medical School. The first and the second ChIP-Seq samples yielded $125x10^6$ and $240x10^6$ sequences of MKI67-binding sites, respectively, which is consistent with the expectation that these values would result from differences in cell numbers used for the first and the second ChIP-Seq sample preparations.

Statistical analysis of ChIP-Seq

Sequence data quality was evaluated using FASTQC v0.11.9 (see FASTQC in the Data and materials availability for reference). Reads were filtered and trimmed with Atropos v1.1.31 (Didion et al., 2017) to retain high quality reads, which were then mapped to the human reference genome hg38 using Bowtie2 v2.2.5 (Langmead & Salzberg, 2012). Multi-mapping reads and duplicates were removed followed by peak calling with MACS2 v2.2.7.1 (Zhang et al., 2008). Likely peak artifacts were filtered out using the ENCODE blacklist (Amemiya et al., 2019). ChIP-seq data quality was assessed using standard ENCODE metrics, including total reads, alignment rates, fraction of reads in peaks, PCR bottleneck coefficients and the non-redundant fraction (Davis et al., 2018). Data was visualized using IGV (Robinson et al., 2011). DeepTools v3.0.2 (Ramirez et al., 2016) was used to assess coverage and the reproducibility of peaks across replicates. ChIPseeker v1.32.0 (Yu et al., 2015) was used to annotate ChIP-seq peaks to their closest transcriptional start site and plot binding profiles. HOMER v4.11.1 (Heinz et al., 2010) was used to identify enriched transcription factor binding motifs. Analyses in R were done using R v4.2.1. The MAFFT program in Lasergene 17 was used to align DNA sequences in the centromeric regions to find the long MKI67 consensus binding sequences.

RNA-seq

Triplicate cultures of KD-MKI67 and KD-CTL were grown in the presence of 40 nM DsiRNA specific for the MKI67 gene and 40 nM negative control DsiRNA (NC1), respectively, for 70 h,.

In a separate experiment, triplicate cultures of KD-GNL2, KD-MDN1, and KD-CTL were grown in the presence of 40 nM DsiRNA specific for the GNL2 and the MDN1 genes and in the presence of 40 nM NC1, respectively, for 70 h. These cultures were harvested by trypsinization, and the total RNA was extracted using the Monarch Total RNA Miniprep Kit (NEB T2010S). The total RNA (1000 ng) was subjected to ribosomal RNA depletion using the NEBNext rRNA Depletion Kit v2 (E7400S), and the RNA sample was purified using NEBNext Sample Purification Beads (E7767S). Fragmentation was performed by heating at 94C for 10 min. The approximately 200 bp RNA sample was used to synthesize indexed cDNA using the NEBNext Ultra Directional RNA Library Prep Kit for Illumina (E7765) and NEBNext Multiple Oligos for Illumina (E7335). The NEBNext RNA Sample Purification Beads (E7767S) were used for both the size selection of the adaptor-ligated DNA and cleanup of the end-point DNA sample. The resulting cDNA library contained an average size of 300-bp DNAs and lacked the index primers and adaptor, as confirmed by High Sensitivity D1000 ScreenTape. The library was sequenced for 50-bp paired-end reads on an Illumina NextSeq 500 system at the Biopolymers Facilities at Harvard Medical School. The resulting reads were then analyzed using software in the RStudio environment (R/4.2.1) on o2, a platform for Linux-based high-performance computing platform managed by the Research Computing Group at Harvard Medical School. The software used included Rhisat2 VN2.2.1 (Kim et al., 2015) to align RNA-seq reads to the reference genome (GRCh38_snp_tran/genome_snp_tran), featureCount in Rsubread V2.12.2 (Liao et al., 2014)to quantify the number of reads aligned to each gene, DESeq2 v 1.46.0 (Love et al., 2014) to analyze the count matrix for differential gene expression, and Rsamtools V2.22.0 (Li et al., 2009) to sort and index BAM files for visualization in IGV (Robinson et al., 2011).

Acknowledgements

We thank Dr. Danesh Moazed for all his support, Dr. Steven Gygi for providing access to the MS facilities, Drs. Lingsheng Dong, Swapnil Suresh Parhad, William G. Rodriguez, and Harleen Saini for guidance with the RNA-seq statistical analysis and the o2 platform for Linux-based high-performance computing, the CITE at Harvard Medical School for providing access to a confocal microscope, and the BPF Genomics Core Facility at Harvard Medical School (RRID:SCR_007175) for next generation sequencing. We also thank Sergey Naumenko, Noor Sohail, and Shannan Ho Sui at the Harvard Chan Bioinformatics Core (RRID:SCR_025373) for assistance with the ChIP-seq data analysis. Their efforts were funded in part by the Harvard Medical School Foundry.

Author Contributions

S.I. designed the study, performed the experiments, analyzed the data, and wrote the manuscript. J.A.P performed the MS, wrote the methods, and revised the manuscript.

Competing Interests

The authors declare no competing interests.

Research funding

S.I. was supported by the late Dr. Howard Green. J.A.P was supported by NIH grant GM132129.

Data and Material Availability

The plasmids used in this study were deposited at Addgene.

The ChIP-Seq data and the RNA-seq data were deposited at GEO. The ChIP-Seq accession number is GSE288519, and the RNA-seq accession numbers are GSE287864 and GSE287866. The MS data were deposited at Pride, the project accession number is PXD060366.

Websites used in this study

The following websites were used to analyze the data and to reference gene and protein characteristics.

NoD (Nucleolar localization sequence detector) at University of Dundee:
https://www.compbio.dundee.ac.uk/www-nod/

FastQC for ChIP-Seq:
https://www.bioinformatics.babraham.ac.uk/projects/fastqc/ by the Bioinformatics Group at the Babraham Institute.

Gene and Protein characteristics:
https://www.ncbi.nlm.nih.gov/datasets/gene/
https://www.uniprot.org/uniprotkb

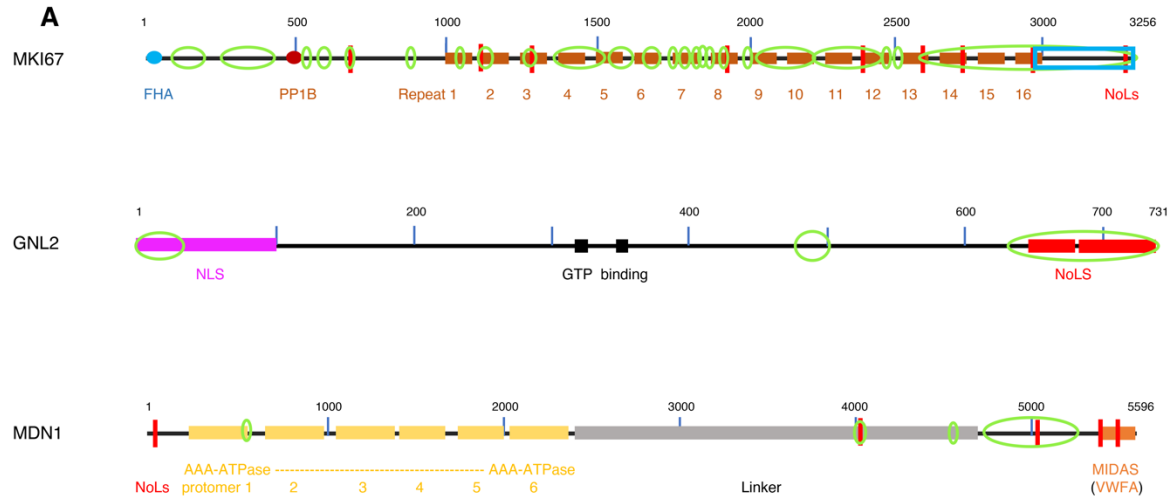

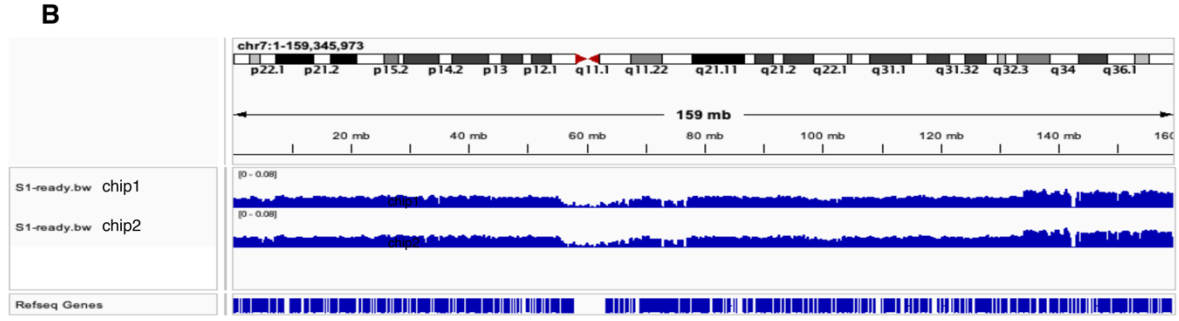

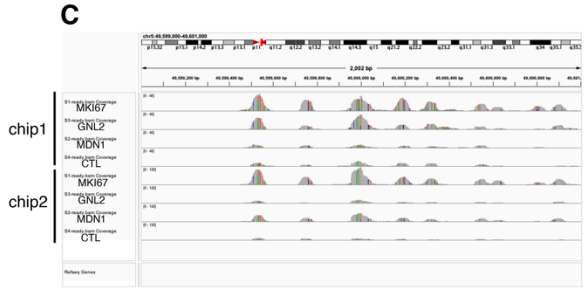

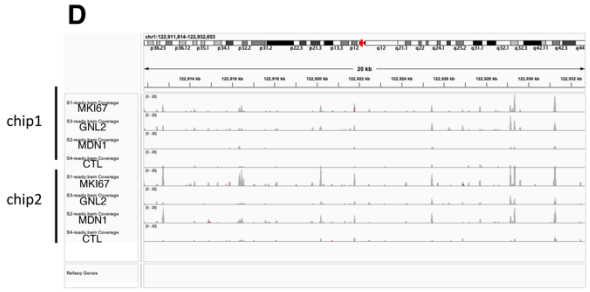

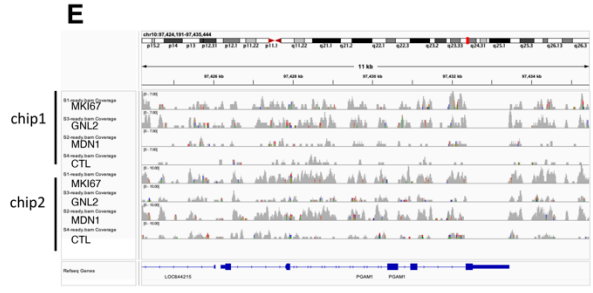

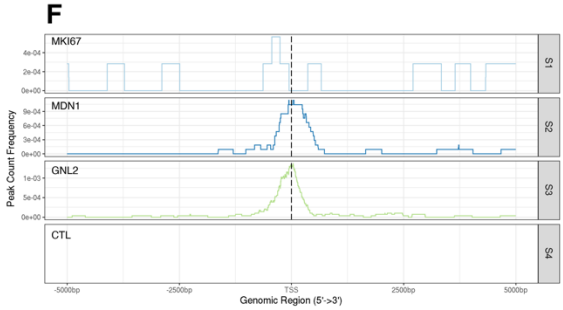

Figure 1 A schematic representation of the primary structures of MKI67, GNL2, and MDN1 proteins, and overview of ChIP-Seq results. **A**. Primary structure of MKI67, GNL2, and MDN1. The red bar, green loop, and blue rectangle indicate the predicted nucleolar localization signal (NoLS) and IDRs, and the C-terminal DNA-binding region, respectively; and additional structural information is provided directly below the sketches. **B**. Bigwig file of MKI67 ChIP-Seq on chr7. **C** and **D**. Overlap of MKI67, GNL2, and MDN1 at the centromeric regions of chr5 and chr1. **E**. Overlapping of MKI67, GNL2, and MDN1 at the PGAM1 gene. **F**. Features of MKI67, MDN1, and GNL2 binding at promoters revealed by ChlPseeker.

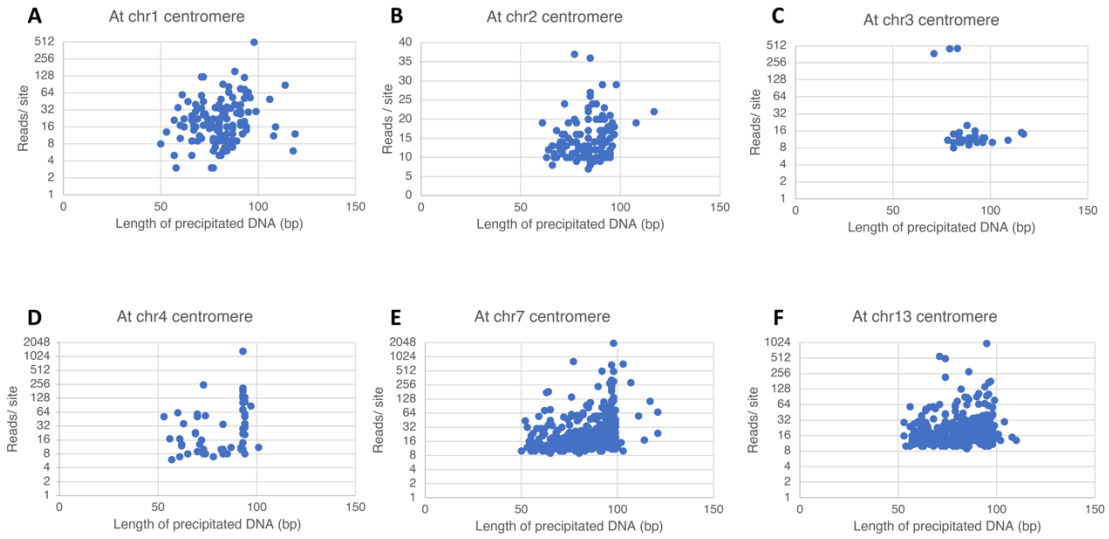

G The first consensus sequence

```
Chr7 left wing consensus for reads 50-1986:      TATtTggAcCTGTTTGAGGCCT-TCGTTGcAAACGGGATTTCTTCnTTTCAT-GCTAGAC--AGAAGTTCTCAGTAACTTTGTG
chr13 right wing consensus for reads 50-988:      aTTTgGAtaGGTTTGAgGccTaCGgTGGAAACGGGAATATCTTCCTATAAAACTAGACAGAAGCATtCTcaTCCTcaAAAC

Chr7  consensus for reads around 10: TtTGCAAGTGGAnATtTgGACCtaTTTGAGGCCtTCGTTgGAAACGGATTTct-TC-At---a
```

H The second consensus sequence

```
Chr7 right wing consensus for reads 50-1986:  TTCAACTCAGAGTtaAACcTTtCTTTtCAtAGAGCAGaTTtGAAACACTCTtTTGTaaAaTTTGCA-GTGaA-AtCtAGAC-aGAA---
Chr13 left wing of for reads 50-988:          cA--T-ACAGAGtTGAACcTTnCTTTTgAcAGAGCAGTTTTGAAACACTCTTT-TGTaGtATCTGgAAGTGgA-aTTtgg

Chr7 consensus for reads around 10:
             TtCtCAGtAAcTtcTTTGTGtTGTGTGtATTCAACTCACAGAGTTGAACCTTcCTTTtCA-AGAGcAG-tT-GAAACA
```

Figure 2 Binding of MKI67 to centromeric regions. All data shown in these graphs were obtained from the chip 2 experiment. **A**, **B**, **C**, **D**, **E**, **F**. Binding of MKI67 to the centromeric region of chr1, chr2, chr3, chr4, chr7, and chr13. Y-axis and X-axis indicate the total reads of a single peak area, and the length of the nucleotide sequence to which MKI67 bound. Only peaks with more than approximately 8 reads per peak area are plotted on the charts. **G**. The first consensus sequences to which MKI67 binds at the chr7 and the chr13 centromeres. **H**. The second consensus sequence to which MKI67 binds at the chr7 and the chr13 centromeres. Below the chr7 and chr13 consensus sequences is a short consensus sequence derived from the low-read (8-10) group of chr7.

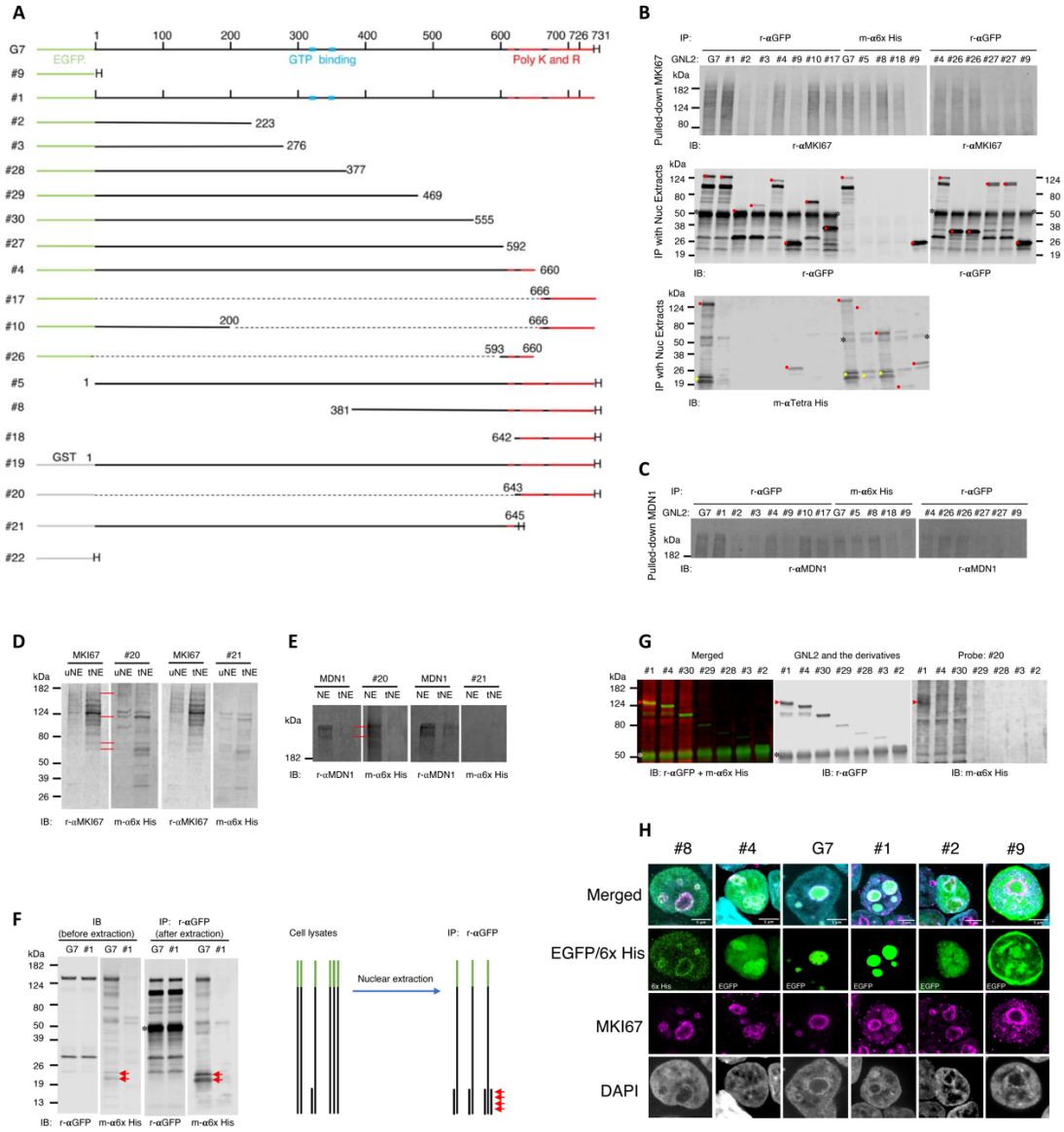

Figure 3 Interaction of GNL2 with MKI67 and MKI67 A. The primary structures encoded by the cloned GNL2 and its deletion mutants. Green line, H, and gray line indicate EGFP, 6x His, and GST tags, respectively. **B**. Endogenous MKI67 pulled down from the nuclear extracts of HEK293T that had been transfected with GNL2 or its mutant protein-encoding plasmids. Top, middle, and bottom panels show the pulled down endogenous MKI67, immunoprecipitants with rabbit anti-GFP antibody, and with mouse anti 6x His antibody, respectively. Red and yellow dots indicate intact and cleaved fragments of GNL2 and the mutants, respectively. **C**. Endogenous MDN1 pulled down with the same antibody and the same extracts. Protein #2 is hidden behind the rabbit IgG band. **D**, **E**. Far Western blots probed with #20 or #24 to show a direct binding of the GNL2 C-terminus to MKI67 and MDN1. **F**. Homologous GNL2-GNL2 binding at the C-terminus. Black star and red arrow indicate rabbit IgG and two cleaved-off GNL2 C-termini, respectively. The two right images (IP: r-**α**GFP) are copies of the middle image in B. An interpretation of the result is added to the right. **G**. Confirmation of the homologous C-terminus-C-terminus binding of GNL2 by far Western blotting. **H**. Confocal microscopic confirmation of the GNL2 C-terminus binding to MKI67 at the nucleolar periphery.

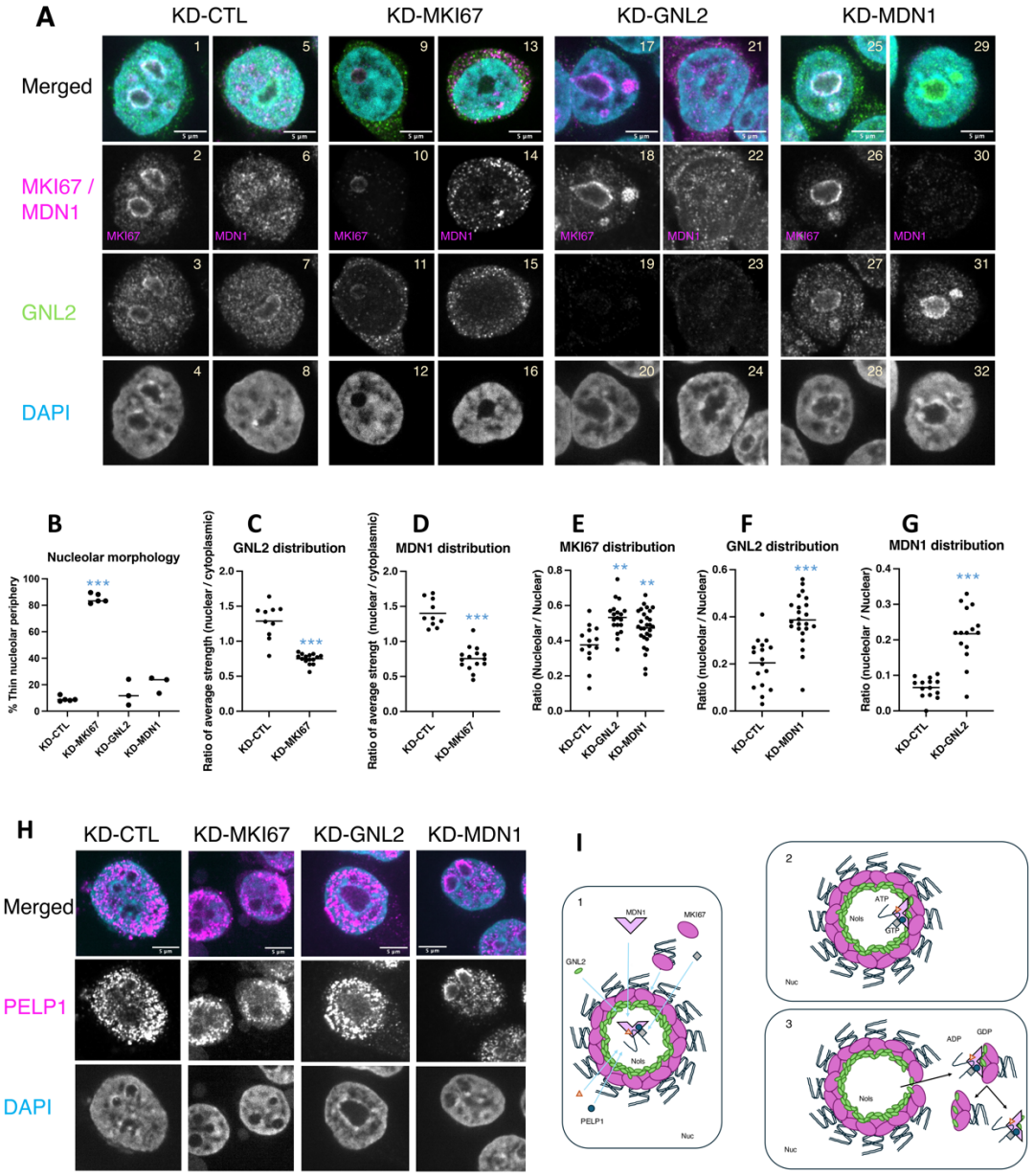

Figure 4 Analysis of nucleolar periphery function by depletion of MKI67, GNL2, and MDN1. **A**. Panels present confocal microscope images resulting from depletion of one of these three proteins and from the control. Only the merged images are shown in color. **B** - **G**. Graphs depict statistical analysis of the images. Most of these graphs are based on the total of signal in an area, whereas graphs **C** and **D** are described by the average signal strength. This is because images of the entire cytoplasm are not available. T-test: ** P <0.001, *** P <0.0001. **H**. PELP1 localization by MDN1 depletion. **I.** A model of the chr-MGMc function at the nucleolar periphery. **I-1**. Most proteins and RNAs are imported into the nucleolus (Nols), except for pre-rRNA. MKI67 can be imported with or without part of the chromosomes. **I-2**. MDN1 in the 60S pre-ribosome particle interacts with GNL2 on the MKI67 layer. **I-3**. MDN1 then opens a gate that allows the chr-MKI67 complex to exit into the nucleus. The exiting complex is likely to separate into a 60S pre-ribosome particle containing GNL2 and chr-MKI67.

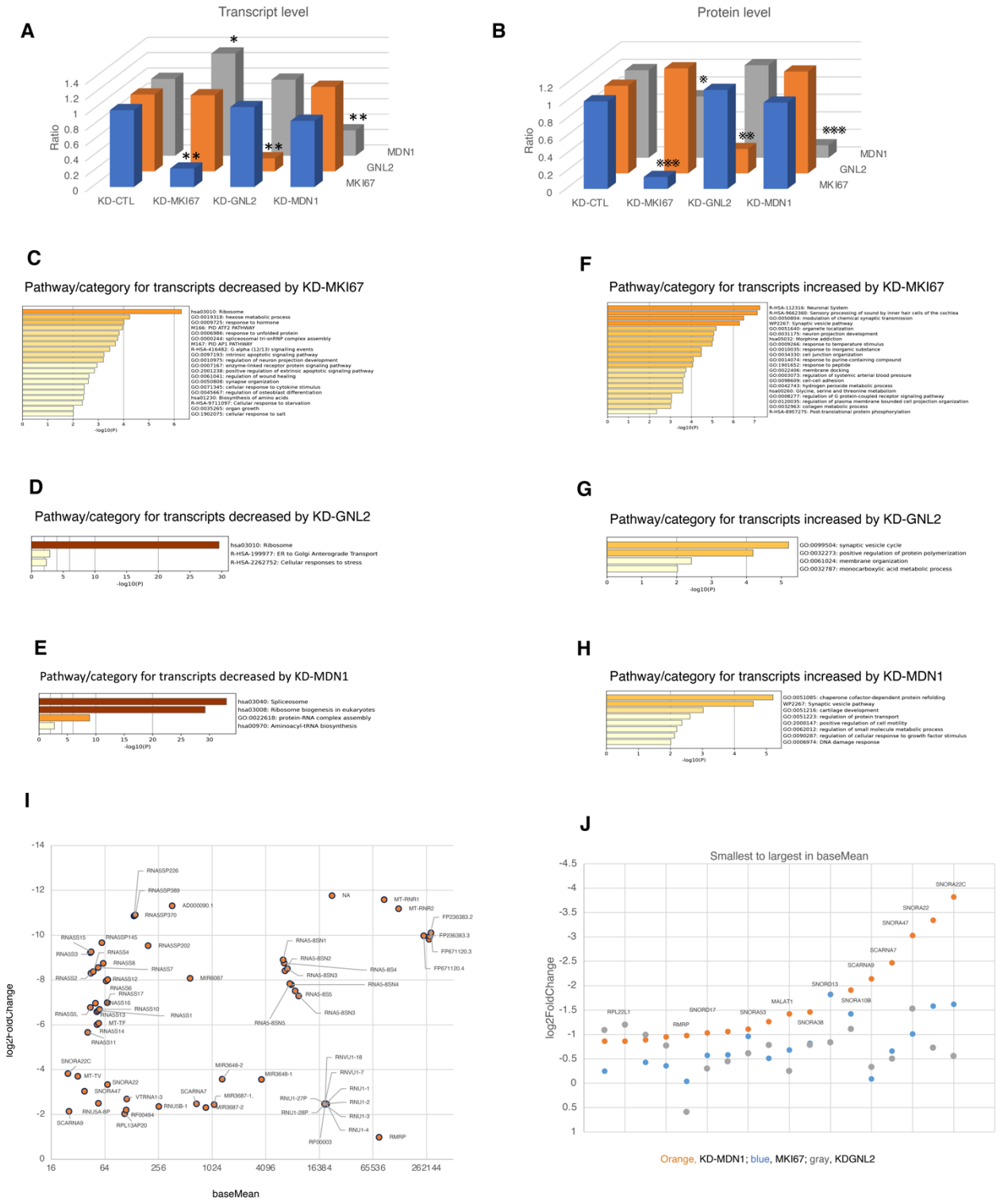

Figure 5 Depletion of MKI67, GNL2, and MDN1 and the consequences. **A**. Levels of transcripts in cultures depleted with siRNA for the *MKI67, GNL2, and MDN1* genes, and the control. The graph is generated from the RNA-seq data normalized to take the value of the control (KD-CTL) as 1.0. Significance is presented based on Padj as follows: ** < 1E-37, * <0.001. **B**. Protein levels in the knockdown cultures. Protein levels were determined by Western blotting for four

independent cultures. T-test, ※※※ < 1E-05, ※※ <0.01, ※ < 0.05. **C**,**D**,**E**. Metascape bar graphs showing pathways/categories reduced by KD-MKI67, KD-GNL2, or KD-MDN1. **F**,**G**,**H**. Metascape bar graphs showing pathways/categories increased by KD-MKI67, KD-GNL2, or KD-MDN1. **I**. Transcripts decreased by KD-MDN1. **J**. Levels of SNORAs and similar transcripts decreased by KD-MDN1, KD-MKI67, and KD-GNL2.

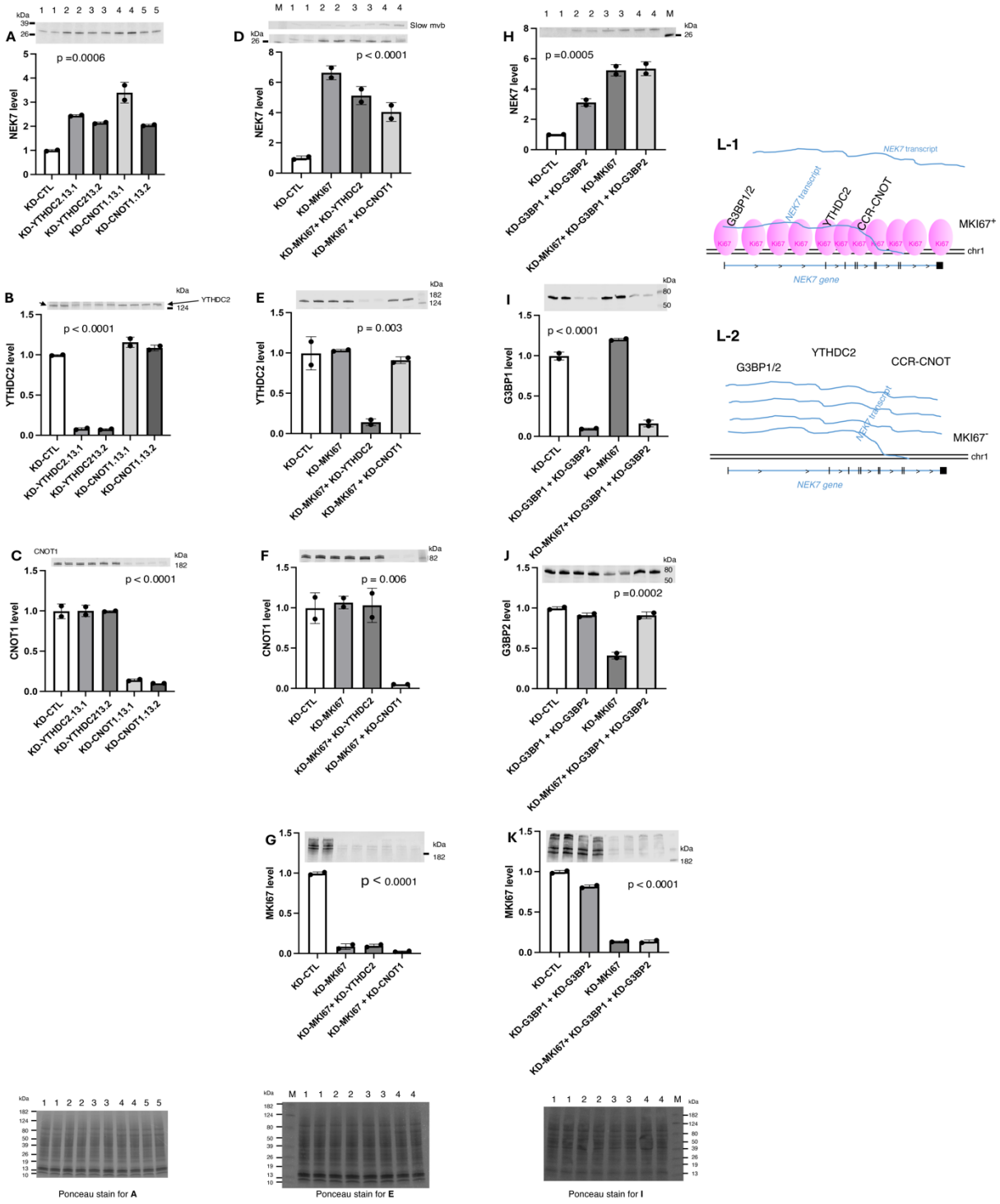

Figure 6 Changes in NEK7 protein levels upon depletion of YTHDC2, CNOT1, or G3BP1/2. Statistical significance was determined by one-way ANOVA test. **A**. Effect of YTHDC2 and CNOT1 depletion. **B**, **C**. Confirmation of depletion of YTHDC2 and CNOT1. **D**. The effect of depletion of YTHDC2 and CNOT1 in combination with MKI67 depletion. In lanes 3 and 4, slow mvb (slow mobilizing NEK7 bands) appeared and simultaneously the levels of 26-kDa NEK7 bands decreased. **E**, **F**, **G**. Confirmation of YTHDC2, CNOT1, and MKI67 depletion. **H**. Effect of depletion of both G3BP1 and G3BP2 in combination with MKI67 depletion. **I**, **J**, **K**. Confirmation of G3BP1, G3BP2, and MKI67 depletion. For these Western blots, 50 μg of extract protein was added to one well of protein gels. The Ponceau staining image of each experiment is shown at the bottom. **L**-1: A model of downregulation of the *NEK7* transcripts (pink lines) by cooperation of MKI67 with the G3BP1, YTHDC2, and CCR-CNOT systems; **L-2**: a model of upregulation of the *HEK7* transcripts due to release of the G3BP1, YTHDC2, and CCR4-NOT systems from the *NEK7* gene in MKI67-depleted cells.

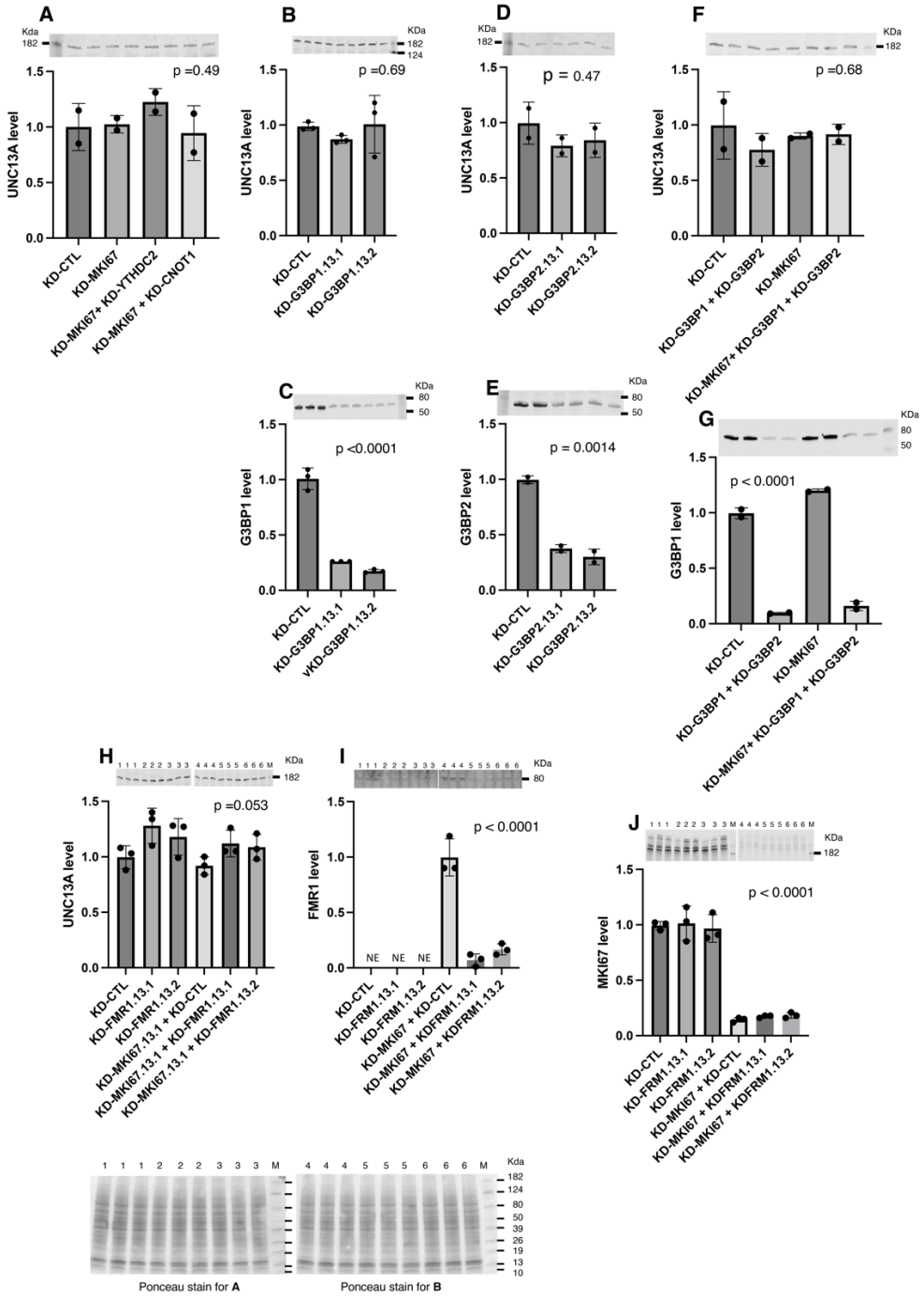

Figure 7 Changes in UNC13A protein levels upon depletion of YTHDC2, CNOT1, G3BP1/2, and FRM1. Statistical significance was determined by one-way ANOVA test. **A, B, D, F**. No effect of the YTHDC2, CNOT1, G3BP1, and G3BP2 depletion on UNC13A protein levels independent of MKI67 depletion. **C, E, G**. Confirmation of G3BP1 and G3BP2 depletion. **H**. Effect of FMR1 depletion with or without MKI67 depletion. **I**. Confirmation of FMR1 depletion. NE indicates no estimation of the levels due to the high background interference. **J**. Confirmation of MKI67 depletion. Western blotting for this set of experiments was performed as indicated in the legend of Figure 6. Ponceau staining is shown at the bottom.

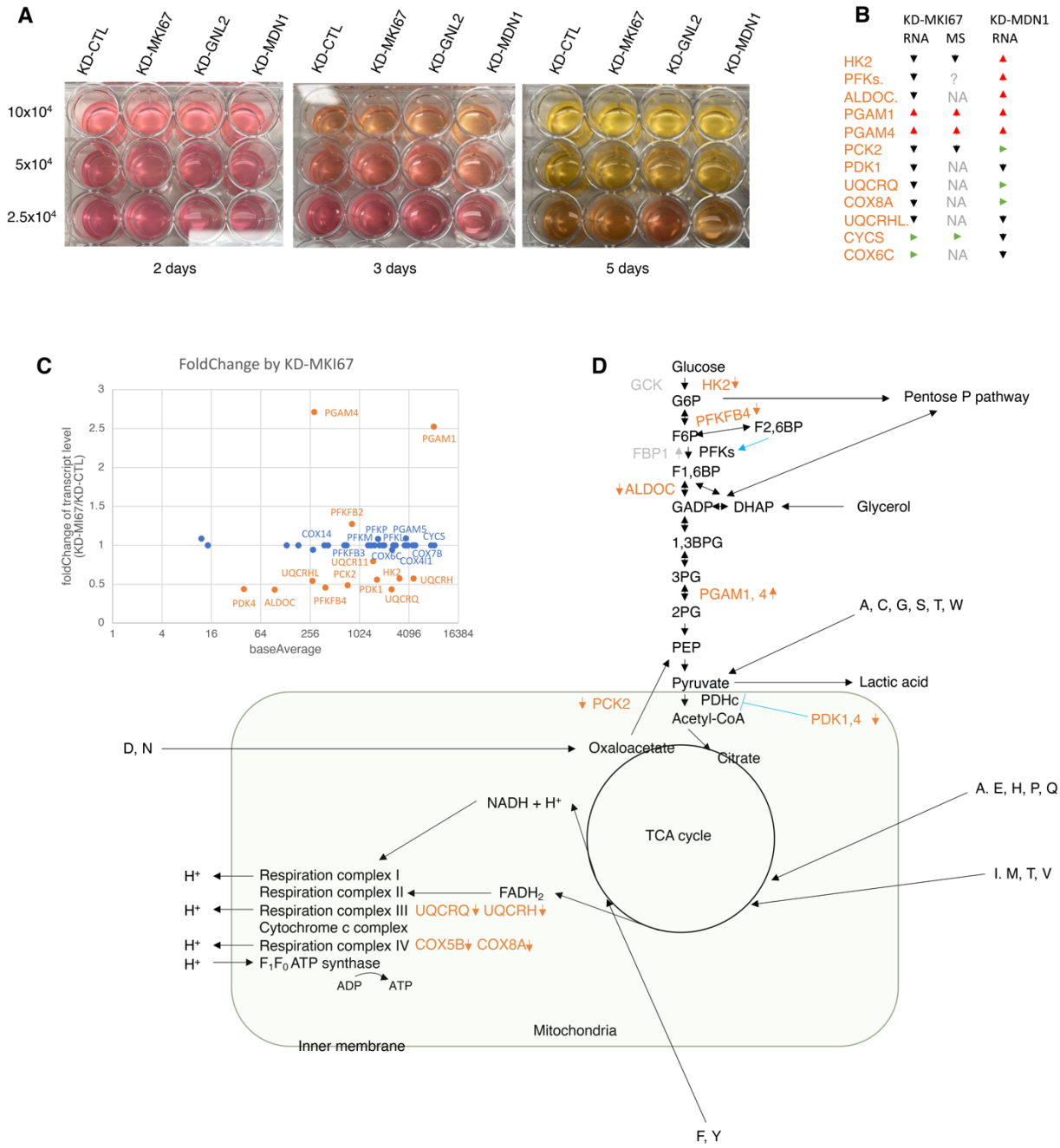

Figure 8 Changes in the levels of enzymes/factors of respiration and sugar metabolism caused by depletion of MKI67 or MDN1. **A**. Lower culture pH due to MKI67 or MDN1 depletion. The left lane shows the number of inoculated cells. Acidification of the cultures was evident 2, 3, and 5 days after the initiation of these KDs. **B**. The table provides a simplified overview of the changes in the levels of transcripts relevant to glucose metabolism and respiration (electron transport system). Upregulation and downregulation are indicated by red and black arrows, respectively. NA indicates data not available. The RNA and MS indicate that the data are from RNA-seq and mass spectrometry data, respectively. See Supplemental Table 4. **C**. Mplot of transcripts relevant for glucose metabolism and respiration (electron transport system) in the KD-MKI67 cultures. Orange circles indicate transcripts that were significantly changed by the

depletion (Padj <0.05). **D**. Visualization of MKI67 depletion-induced changes in proteins/enzymes on the glucose metabolism and respiration map. Black arrows indicate reaction flows, while blue lines indicate activation or inhibition.

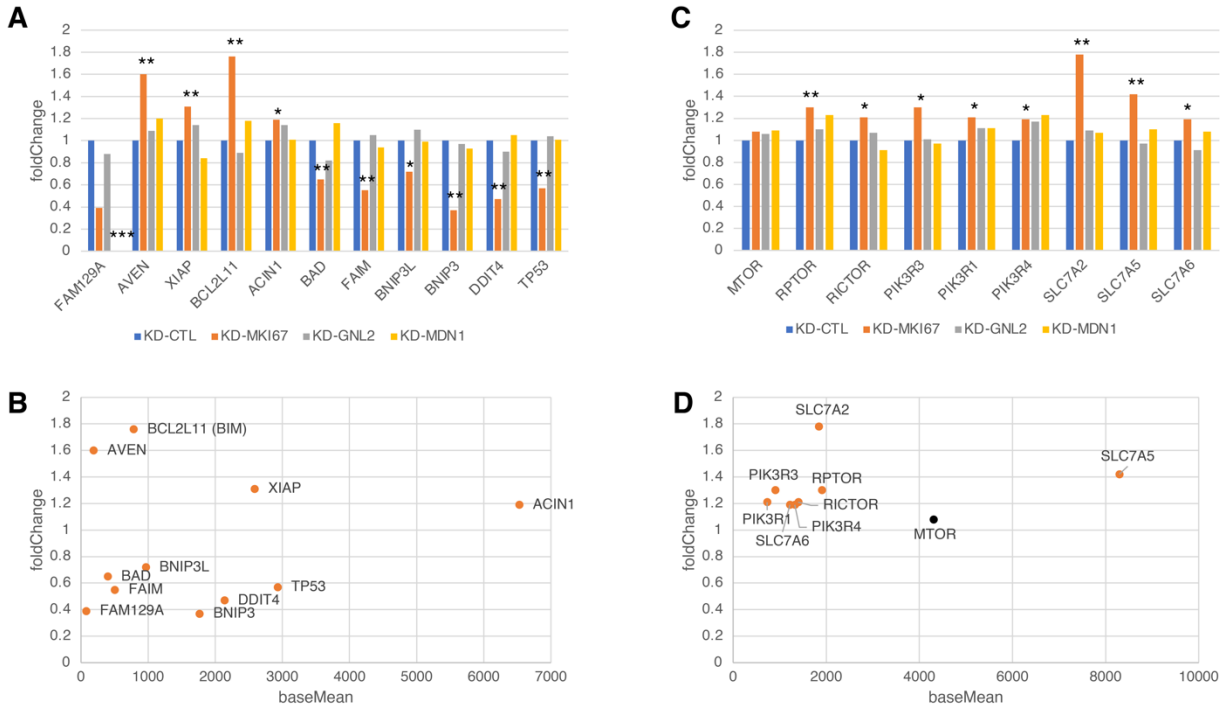

Figure 9 MKI67-mediated regulation of apoptotic proteins and MTOR-activating proteins. **A**. Alteration of transcript levels by MKI67 depletion indicating acquisition of apoptosis resistance. **B**. Mplot for A. **C**. MKI67-deletion-mediated upregulation of transcripts whose protein functions activate MTOR. **D**. Mplot for C. All data show the changes in MKI67-depleted cells compared to the control cells. *, **, ***, indicate Padj ≦ 0.05, Padj ＜0.001, and data not available, respectively.

REFERENCES

Amemiya, H. M., Kundaje, A., & Boyle, A. P. (2019). The ENCODE Blacklist: Identification of Problematic Regions of the Genome. *Sci Rep*, *9*(1), 9354. https://doi.org/10.1038/s41598-019-45839-z

Bassler, J., & Hurt, E. (2019). Eukaryotic Ribosome Assembly. *Annu Rev Biochem*, *88*, 281-306. https://doi.org/10.1146/annurev-biochem-013118-110817

Bell, S., Rousseau, J., Peng, H., Aouabed, Z., Priam, P., Theroux, J. F., Jefri, M., Tanti, A., Wu, H., Kolobova, I., Silviera, H., Manzano-Vargas, K., Ehresmann, S., Hamdan, F. F., Hettige, N., Zhang, X., Antonyan, L., Nassif, C., Ghaloul-Gonzalez, L., . . . Campeau, P. M. (2019). Mutations in ACTL6B Cause Neurodevelopmental Deficits and Epilepsy and Lead to Loss of Dendrites in Human Neurons. *Am J Hum Genet*, *104*(5), 815-834. https://doi.org/10.1016/j.ajhg.2019.03.022

Bensaad, K., Tsuruta, A., Selak, M. A., Vidal, M. N., Nakano, K., Bartrons, R., Gottlieb, E., & Vousden, K. H. (2006). TIGAR, a p53-inducible regulator of glycolysis and apoptosis. *Cell*, *126*(1), 107-120. https://doi.org/10.1016/j.cell.2006.05.036

Booth, D. G., & Earnshaw, W. C. (2017). Ki-67 and the Chromosome Periphery Compartment in Mitosis. *Trends Cell Biol*, *27*(12), 906-916. https://doi.org/10.1016/j.tcb.2017.08.001

Booth, D. G., Takagi, M., Sanchez-Pulido, L., Petfalski, E., Vargiu, G., Samejima, K., Imamoto, N., Ponting, C. P., Tollervey, D., Earnshaw, W. C., & Vagnarelli, P. (2014). Ki-67 is a PP1-interacting protein that organises the mitotic chromosome periphery. *Elife*, *3*, e01641. https://doi.org/10.7554/eLife.01641

Cancer Genome Atlas Research, N. (2014). Comprehensive molecular profiling of lung adenocarcinoma. *Nature*, *511*(7511), 543-550. https://doi.org/10.1038/nature13385

Castle, C. D., Cassimere, E. K., & Denicourt, C. (2012). LAS1L interacts with the mammalian Rix1 complex to regulate ribosome biogenesis. *Mol Biol Cell*, *23*(4), 716-728. https://doi.org/10.1091/mbc.E11-06-0530

Castle, C. D., Cassimere, E. K., Lee, J., & Denicourt, C. (2010). Las1L is a nucleolar protein required for cell proliferation and ribosome biogenesis. *Mol Cell Biol*, *30*(18), 4404-4414. https://doi.org/10.1128/MCB.00358-10

Chen, Z., Suzuki, H., Kobayashi, Y., Wang, A. C., DiMaio, F., Kawashima, S. A., Walz, T., & Kapoor, T. M. (2018). Structural Insights into Mdn1, an Essential AAA Protein Required for Ribosome Biogenesis. *Cell*, *175*(3), 822-834 e818. https://doi.org/10.1016/j.cell.2018.09.015

Chennupati, V., Datta, D., Rao, M. R., Boddapati, N., Kayasani, M., Sankaranarayanan, R., Mishra, M., Seth, P., Mani, C., & Mahalingam, S. (2011). Signals and pathways regulating nucleolar retention of novel putative nucleolar GTPase NGP-1(GNL-2). *Biochemistry*, *50*(21), 4521-4536. https://doi.org/10.1021/bi200425b

Cheutin, T., O'Donohue, M. F., Beorchia, A., Klein, C., Kaplan, H., & Ploton, D. (2003). Three-dimensional organization of pKi-67: a comparative fluorescence and electron tomography study using FluoroNanogold. *J Histochem Cytochem*, *51*(11), 1411-1423. https://doi.org/10.1177/002215540305101102

Cuylen, S., Blaukopf, C., Politi, A. Z., Muller-Reichert, T., Neumann, B., Poser, I., Ellenberg, J., Hyman, A. A., & Gerlich, D. W. (2016). Ki-67 acts as a biological surfactant to disperse

mitotic chromosomes. *Nature*, *535*(7611), 308-312. https://doi.org/10.1038/nature18610

Czabotar, P. E., & Garcia-Saez, A. J. (2023). Mechanisms of BCL-2 family proteins in mitochondrial apoptosis. *Nat Rev Mol Cell Biol*, *24*(10), 732-748. https://doi.org/10.1038/s41580-023-00629-4

Dar, S. A., Malla, S., Martinek, V., Payea, M. J., Lee, C. T., Martin, J., Khandeshi, A. J., Martindale, J. L., Belair, C., & Maragkakis, M. (2024). Full-length direct RNA sequencing uncovers stress granule-dependent RNA decay upon cellular stress. *Elife*, *13*. https://doi.org/10.7554/eLife.96284

Davis, C. A., Hitz, B. C., Sloan, C. A., Chan, E. T., Davidson, J. M., Gabdank, I., Hilton, J. A., Jain, K., Baymuradov, U. K., Narayanan, A. K., Onate, K. C., Graham, K., Miyasato, S. R., Dreszer, T. R., Strattan, J. S., Jolanki, O., Tanaka, F. Y., & Cherry, J. M. (2018). The Encyclopedia of DNA elements (ENCODE): data portal update. *Nucleic Acids Res*, *46*(D1), D794-D801. https://doi.org/10.1093/nar/gkx1081

Dergai, O., & Hernandez, N. (2019). How to Recruit the Correct RNA Polymerase? Lessons from snRNA Genes. *Trends Genet*, *35*(6), 457-469. https://doi.org/10.1016/j.tig.2019.04.001

Diana, P., & Carvalheira, G. M. G. (2022). NIBAN1, Exploring its Roles in Cell Survival Under Stress Context. *Front Cell Dev Biol*, *10*, 867003. https://doi.org/10.3389/fcell.2022.867003

Didion, J. P., Martin, M., & Collins, F. S. (2017). Atropos: specific, sensitive, and speedy trimming of sequencing reads. *PeerJ*, *5*, e3720. https://doi.org/10.7717/peerj.3720

Duttke, S. H. (2014). RNA polymerase III accurately initiates transcription from RNA polymerase II promoters in vitro. *J Biol Chem*, *289*(29), 20396-20404. https://doi.org/10.1074/jbc.M114.563254

Elias, J. E., & Gygi, S. P. (2007). Target-decoy search strategy for increased confidence in large-scale protein identifications by mass spectrometry. *Nat Methods*, *4*(3), 207-214. https://doi.org/10.1038/nmeth1019

Elias, J. E., & Gygi, S. P. (2010). Target-decoy search strategy for mass spectrometry-based proteomics. *Methods Mol Biol*, *604*, 55-71. https://doi.org/10.1007/978-1-60761-444-9_5

Finkbeiner, E., Haindl, M., & Muller, S. (2011). The SUMO system controls nucleolar partitioning of a novel mammalian ribosome biogenesis complex. *EMBO J*, *30*(6), 1067-1078. https://doi.org/10.1038/emboj.2011.33

Garwain, O., Sun, X., Iyer, D. R., Li, R., Zhu, L. J., & Kaufman, P. D. (2021). The chromatin-binding domain of Ki-67 together with p53 protects human chromosomes from mitotic damage. *Proc Natl Acad Sci U S A*, *118*(32). https://doi.org/10.1073/pnas.2021998118

Gerdes, J., Lemke, H., Baisch, H., Wacker, H. H., Schwab, U., & Stein, H. (1984). Cell cycle analysis of a cell proliferation-associated human nuclear antigen defined by the monoclonal antibody Ki-67. *J Immunol*, *133*(4), 1710-1715. https://www.ncbi.nlm.nih.gov/pubmed/6206131

Gerdes, J., Li, L., Schlueter, C., Duchrow, M., Wohlenberg, C., Gerlach, C., Stahmer, I., Kloth, S., Brandt, E., & Flad, H. D. (1991). Immunobiochemical and molecular biologic characterization of the cell proliferation-associated nuclear antigen that is defined by

monoclonal antibody Ki-67. *Am J Pathol*, *138*(4), 867-873. https://www.ncbi.nlm.nih.gov/pubmed/2012175

Gerdes, J., Schwab, U., Lemke, H., & Stein, H. (1983). Production of a mouse monoclonal antibody reactive with a human nuclear antigen associated with cell proliferation. *Int J Cancer*, *31*(1), 13-20. https://doi.org/10.1002/ijc.2910310104

Graham, F. L., Smiley, J., Russell, W. C., & Nairn, R. (1977). Characteristics of a human cell line transformed by DNA from human adenovirus type 5. *J Gen Virol*, *36*(1), 59-74. https://doi.org/10.1099/0022-1317-36-1-59

Grasmann, G., Smolle, E., Olschewski, H., & Leithner, K. (2019). Gluconeogenesis in cancer cells - Repurposing of a starvation-induced metabolic pathway? *Biochim Biophys Acta Rev Cancer*, *1872*(1), 24-36. https://doi.org/10.1016/j.bbcan.2019.05.006

Hayashi, Y., Kato, K., & Kimura, K. (2017). The hierarchical structure of the perichromosomal layer comprises Ki67, ribosomal RNAs, and nucleolar proteins. *Biochem Biophys Res Commun*, *493*(2), 1043-1049. https://doi.org/10.1016/j.bbrc.2017.09.092

Heinz, S., Benner, C., Spann, N., Bertolino, E., Lin, Y. C., Laslo, P., Cheng, J. X., Murre, C., Singh, H., & Glass, C. K. (2010). Simple combinations of lineage-determining transcription factors prime cis-regulatory elements required for macrophage and B cell identities. *Mol Cell*, *38*(4), 576-589. https://doi.org/10.1016/j.molcel.2010.05.004

Hori, Y., Engel, C., & Kobayashi, T. (2023). Regulation of ribosomal RNA gene copy number, transcription and nucleolus organization in eukaryotes. *Nat Rev Mol Cell Biol*, *24*(6), 414-429. https://doi.org/10.1038/s41580-022-00573-9

Huttlin, E. L., Jedrychowski, M. P., Elias, J. E., Goswami, T., Rad, R., Beausoleil, S. A., Villen, J., Haas, W., Sowa, M. E., & Gygi, S. P. (2010). A tissue-specific atlas of mouse protein phosphorylation and expression. *Cell*, *143*(7), 1174-1189. https://doi.org/10.1016/j.cell.2010.12.001

Iuchi, S., & Paulo, J. A. (2019). Lysine-specific demethylase 2A enhances binding of various nuclear factors to CpG-rich genomic DNAs by action of its CXXC-PHD domain. *Sci Rep*, *9*(1), 5496. https://doi.org/10.1038/s41598-019-41896-6

Iuchi, S., & Paulo, J. A. (2021). RNAmetasome network for macromolecule biogenesis in human cells. *Commun Biol*, *4*(1), 1399. https://doi.org/10.1038/s42003-021-02928-y

Kim, D., Langmead, B., & Salzberg, S. L. (2015). HISAT: a fast spliced aligner with low memory requirements. *Nat Methods*, *12*(4), 357-360. https://doi.org/10.1038/nmeth.3317

Kim, S., Lee, K., & Rhee, K. (2007). NEK7 is a centrosomal kinase critical for microtubule nucleation. *Biochem Biophys Res Commun*, *360*(1), 56-62. https://doi.org/10.1016/j.bbrc.2007.05.206

Kipper, K., Mansour, A., & Pulk, A. (2022). Neuronal RNA granules are ribosome complexes stalled at the pre-translocation state. *J Mol Biol*, *434*(20), 167801. https://doi.org/10.1016/j.jmb.2022.167801

Klinge, S., & Woolford, J. L., Jr. (2019). Ribosome assembly coming into focus. *Nat Rev Mol Cell Biol*, *20*(2), 116-131. https://doi.org/10.1038/s41580-018-0078-y

Kreitz, S., Fackelmayer, F. O., Gerdes, J., & Knippers, R. (2000). The proliferation-specific human Ki-67 protein is a constituent of compact chromatin. *Exp Cell Res*, *261*(1), 284-292. https://doi.org/10.1006/excr.2000.5064

Langmead, B., & Salzberg, S. L. (2012). Fast gapped-read alignment with Bowtie 2. *Nat Methods*, *9*(4), 357-359. https://doi.org/10.1038/nmeth.1923

Li, H., Handsaker, B., Wysoker, A., Fennell, T., Ruan, J., Homer, N., Marth, G., Abecasis, G., Durbin, R., & Genome Project Data Processing, S. (2009). The Sequence Alignment/Map format and SAMtools. *Bioinformatics*, *25*(16), 2078-2079. https://doi.org/10.1093/bioinformatics/btp352

Liao, Y., Smyth, G. K., & Shi, W. (2014). featureCounts: an efficient general purpose program for assigning sequence reads to genomic features. *Bioinformatics*, *30*(7), 923-930. https://doi.org/10.1093/bioinformatics/btt656

Lobo, S. M., & Hernandez, N. (1989). A 7 bp mutation converts a human RNA polymerase II snRNA promoter into an RNA polymerase III promoter. *Cell*, *58*(1), 55-67. https://doi.org/10.1016/0092-8674(89)90402-9

Love, M. I., Huber, W., & Anders, S. (2014). Moderated estimation of fold change and dispersion for RNA-seq data with DESeq2. *Genome Biol*, *15*(12), 550. https://doi.org/10.1186/s13059-014-0550-8

MacCallum, D. E., & Hall, P. A. (2000). The biochemical characterization of the DNA binding activity of pKi67. *J Pathol*, *191*(3), 286-298. https://doi.org/10.1002/1096-9896(2000)9999:9999<::AID-PATH628>3.0.CO;2-J

Matsuo, Y., Granneman, S., Thoms, M., Manikas, R. G., Tollervey, D., & Hurt, E. (2014). Coupled GTPase and remodelling ATPase activities form a checkpoint for ribosome export. *Nature*, *505*(7481), 112-116. https://doi.org/10.1038/nature12731

Miller, I., Min, M., Yang, C., Tian, C., Gookin, S., Carter, D., & Spencer, S. L. (2018). Ki67 is a Graded Rather than a Binary Marker of Proliferation versus Quiescence. *Cell Rep*, *24*(5), 1105-1112 e1105. https://doi.org/10.1016/j.celrep.2018.06.110

Mondal, B., Jin, H., Kallappagoudar, S., Sedkov, Y., Martinez, T., Sentmanat, M. F., Poet, G. J., Li, C., Fan, Y., Pruett-Miller, S. M., & Herz, H. M. (2020). The histone deacetylase complex MiDAC regulates a neurodevelopmental gene expression program to control neurite outgrowth. *Elife*, *9*. https://doi.org/10.7554/eLife.57519

Murayama, A., Ohmori, K., Fujimura, A., Minami, H., Yasuzawa-Tanaka, K., Kuroda, T., Oie, S., Daitoku, H., Okuwaki, M., Nagata, K., Fukamizu, A., Kimura, K., Shimizu, T., & Yanagisawa, J. (2008). Epigenetic control of rDNA loci in response to intracellular energy status. *Cell*, *133*(4), 627-639. https://doi.org/10.1016/j.cell.2008.03.030

Raman, N., Weir, E., & Muller, S. (2016). The AAA ATPase MDN1 Acts as a SUMO-Targeted Regulator in Mammalian Pre-ribosome Remodeling. *Mol Cell*, *64*(3), 607-615. https://doi.org/10.1016/j.molcel.2016.09.039

Ramirez, F., Ryan, D. P., Gruning, B., Bhardwaj, V., Kilpert, F., Richter, A. S., Heyne, S., Dundar, F., & Manke, T. (2016). deepTools2: a next generation web server for deep-sequencing data analysis. *Nucleic Acids Res*, *44*(W1), W160-165. https://doi.org/10.1093/nar/gkw257

Richter, J. D., & Zhao, X. (2021). The molecular biology of FMRP: new insights into fragile X syndrome. *Nat Rev Neurosci*, *22*(4), 209-222. https://doi.org/10.1038/s41583-021-00432-0

Riggs, C. L., Kedersha, N., Ivanov, P., & Anderson, P. (2020). Mammalian stress granules and P bodies at a glance. *J Cell Sci*, *133*(16). https://doi.org/10.1242/jcs.242487

Robinson, J. T., Thorvaldsdottir, H., Winckler, W., Guttman, M., Lander, E. S., Getz, G., & Mesirov, J. P. (2011). Integrative genomics viewer. *Nat Biotechnol*, *29*(1), 24-26. https://doi.org/10.1038/nbt.1754

Saiwaki, T., Kotera, I., Sasaki, M., Takagi, M., & Yoneda, Y. (2005). In vivo dynamics and kinetics of pKi-67: transition from a mobile to an immobile form at the onset of anaphase. *Exp Cell Res*, *308*(1), 123-134. https://doi.org/10.1016/j.yexcr.2005.04.010

Schindelin, J., Arganda-Carreras, I., Frise, E., Kaynig, V., Longair, M., Pietzsch, T., Preibisch, S., Rueden, C., Saalfeld, S., Schmid, B., Tinevez, J. Y., White, D. J., Hartenstein, V., Eliceiri, K., Tomancak, P., & Cardona, A. (2012). Fiji: an open-source platform for biological-image analysis. *Nat Methods*, *9*(7), 676-682. https://doi.org/10.1038/nmeth.2019

Scholzen, T., Endl, E., Wohlenberg, C., van der Sar, S., Cowell, I. G., Gerdes, J., & Singh, P. B. (2002). The Ki-67 protein interacts with members of the heterochromatin protein 1 (HP1) family: a potential role in the regulation of higher-order chromatin structure. *J Pathol*, *196*(2), 135-144. https://doi.org/10.1002/path.1016

Scholzen, T., & Gerdes, J. (2000). The Ki-67 protein: from the known and the unknown. *J Cell Physiol*, *182*(3), 311-322. https://doi.org/10.1002/(SICI)1097-4652(200003)182:3<311::AID-JCP1>3.0.CO;2-9

Scott, M. S., Boisvert, F. M., McDowall, M. D., Lamond, A. I., & Barton, G. J. (2010). Characterization and prediction of protein nucleolar localization sequences. *Nucleic Acids Res*, *38*(21), 7388-7399. https://doi.org/10.1093/nar/gkq653

Scott, M. S., Troshin, P. V., & Barton, G. J. (2011). NoD: a Nucleolar localization sequence detector for eukaryotic and viral proteins. *BMC Bioinformatics*, *12*, 317. https://doi.org/10.1186/1471-2105-12-317

Shannon, P., Markiel, A., Ozier, O., Baliga, N. S., Wang, J. T., Ramage, D., Amin, N., Schwikowski, B., & Ideker, T. (2003). Cytoscape: a software environment for integrated models of biomolecular interaction networks. *Genome Res*, *13*(11), 2498-2504. https://doi.org/10.1101/gr.1239303

Shaw, G., Morse, S., Ararat, M., & Graham, F. L. (2002). Preferential transformation of human neuronal cells by human adenoviruses and the origin of HEK 293 cells. *FASEB J*, *16*(8), 869-871. https://doi.org/10.1096/fj.01-0995fje

Sidibe, H., Dubinski, A., & Vande Velde, C. (2021). The multi-functional RNA-binding protein G3BP1 and its potential implication in neurodegenerative disease. *J Neurochem*, *157*(4), 944-962. https://doi.org/10.1111/jnc.15280

Sobecki, M., Mrouj, K., Camasses, A., Parisis, N., Nicolas, E., Lleres, D., Gerbe, F., Prieto, S., Krasinska, L., David, A., Eguren, M., Birling, M. C., Urbach, S., Hem, S., Dejardin, J., Malumbres, M., Jay, P., Dulic, V., Lafontaine, D., . . . Fisher, D. (2016). The cell proliferation antigen Ki-67 organises heterochromatin. *Elife*, *5*, e13722. https://doi.org/10.7554/eLife.13722

Spears, E., Stanley, J. E., Shou, M., Yin, L., Li, X., Dai, C., Bradley, A., Sellick, K., Poffenberger, G., Coate, K. C., Shrestha, S., Jenkins, R., Sloop, K. W., Wilson, K. T., Attie, A. D., Keller, M. P., Chen, W., Powers, A. C., & Dean, E. D. (2023). Pancreatic islet alpha cell function and proliferation requires the arginine transporter SLC7A2. *bioRxiv*. https://doi.org/10.1101/2023.08.10.552656

Takagi, M., Nishiyama, Y., Taguchi, A., & Imamoto, N. (2014). Ki67 antigen contributes to the timely accumulation of protein phosphatase 1gamma on anaphase chromosomes. *J Biol Chem*, *289*(33), 22877-22887. https://doi.org/10.1074/jbc.M114.556647

Takagi, M., Sueishi, M., Saiwaki, T., Kametaka, A., & Yoneda, Y. (2001). A novel nucleolar protein, NIFK, interacts with the forkhead associated domain of Ki-67 antigen in mitosis. *J Biol Chem*, *276*(27), 25386-25391. https://doi.org/10.1074/jbc.M102227200

Thiel, C. T., Horn, D., Zabel, B., Ekici, A. B., Salinas, K., Gebhart, E., Ruschendorf, F., Sticht, H., Spranger, J., Muller, D., Zweier, C., Schmitt, M. E., Reis, A., & Rauch, A. (2005). Severely incapacitating mutations in patients with extreme short stature identify RNA-processing endoribonuclease RMRP as an essential cell growth regulator. *Am J Hum Genet*, *77*(5), 795-806. https://doi.org/10.1086/497708

Tomecki, R., Sikorski, P. J., & Zakrzewska-Placzek, M. (2017). Comparison of preribosomal RNA processing pathways in yeast, plant and human cells - focus on coordinated action of endo- and exoribonucleases. *FEBS Lett*, *591*(13), 1801-1850. https://doi.org/10.1002/1873-3468.12682

Uxa, S., Castillo-Binder, P., Kohler, R., Stangner, K., Muller, G. A., & Engeland, K. (2021). Ki-67 gene expression. *Cell Death Differ*, *28*(12), 3357-3370. https://doi.org/10.1038/s41418-021-00823-x

Valverde, J. M., Dubra, G., Phillips, M., Haider, A., Elena-Real, C., Fournet, A., Alghoul, E., Chahar, D., Andres-Sanchez, N., Paloni, M., Bernado, P., van Mierlo, G., Vermeulen, M., van den Toorn, H., Heck, A. J. R., Constantinou, A., Barducci, A., Ghosh, K., Sibille, N., . . . Altelaar, M. (2023). A cyclin-dependent kinase-mediated phosphorylation switch of disordered protein condensation. *Nat Commun*, *14*(1), 6316. https://doi.org/10.1038/s41467-023-42049-0

Wang, J., Ou, S. W., & Wang, Y. J. (2017). Distribution and function of voltage-gated sodium channels in the nervous system. *Channels (Austin)*, *11*(6), 534-554. https://doi.org/10.1080/19336950.2017.1380758

Webster, S. F., & Ghalei, H. (2023). Maturation of small nucleolar RNAs: from production to function. *RNA Biol*, *20*(1), 715-736. https://doi.org/10.1080/15476286.2023.2254540

Wilkinson, M. E., Charenton, C., & Nagai, K. (2020). RNA Splicing by the Spliceosome. *Annu Rev Biochem*, *89*, 359-388. https://doi.org/10.1146/annurev-biochem-091719-064225

Willemse, S. W., Harley, P., van Eijk, R. P. A., Demaegd, K. C., Zelina, P., Pasterkamp, R. J., van Damme, P., Ingre, C., van Rheenen, W., Veldink, J. H., Kiernan, M. C., Al-Chalabi, A., van den Berg, L. H., Fratta, P., & van Es, M. A. (2023). UNC13A in amyotrophic lateral sclerosis: from genetic association to therapeutic target. *J Neurol Neurosurg Psychiatry*, *94*(8), 649-656. https://doi.org/10.1136/jnnp-2022-330504

Youn, J. Y., Dyakov, B. J. A., Zhang, J., Knight, J. D. R., Vernon, R. M., Forman-Kay, J. D., & Gingras, A. C. (2019). Properties of Stress Granule and P-Body Proteomes. *Mol Cell*, *76*(2), 286-294. https://doi.org/10.1016/j.molcel.2019.09.014

Yu, G., Wang, L. G., & He, Q. Y. (2015). ChIPseeker: an R/Bioconductor package for ChIP peak annotation, comparison and visualization. *Bioinformatics*, *31*(14), 2382-2383. https://doi.org/10.1093/bioinformatics/btv145

Yu, J. S., & Cui, W. (2016). Proliferation, survival and metabolism: the role of PI3K/AKT/mTOR signalling in pluripotency and cell fate determination. *Development*, *143*(17), 3050-3060. https://doi.org/10.1242/dev.137075

Zhang, Y., Liu, T., Meyer, C. A., Eeckhoute, J., Johnson, D. S., Bernstein, B. E., Nusbaum, C., Myers, R. M., Brown, M., Li, W., & Liu, X. S. (2008). Model-based analysis of ChIP-Seq (MACS). *Genome Biol*, *9*(9), R137. https://doi.org/10.1186/gb-2008-9-9-r137

Zhou, Y., Zhou, B., Pache, L., Chang, M., Khodabakhshi, A. H., Tanaseichuk, O., Benner, C., & Chanda, S. K. (2019). Metascape provides a biologist-oriented resource for the analysis of systems-level datasets. *Nat Commun*, *10*(1), 1523. https://doi.org/10.1038/s41467-019-09234-6

Supplemental Figure 1

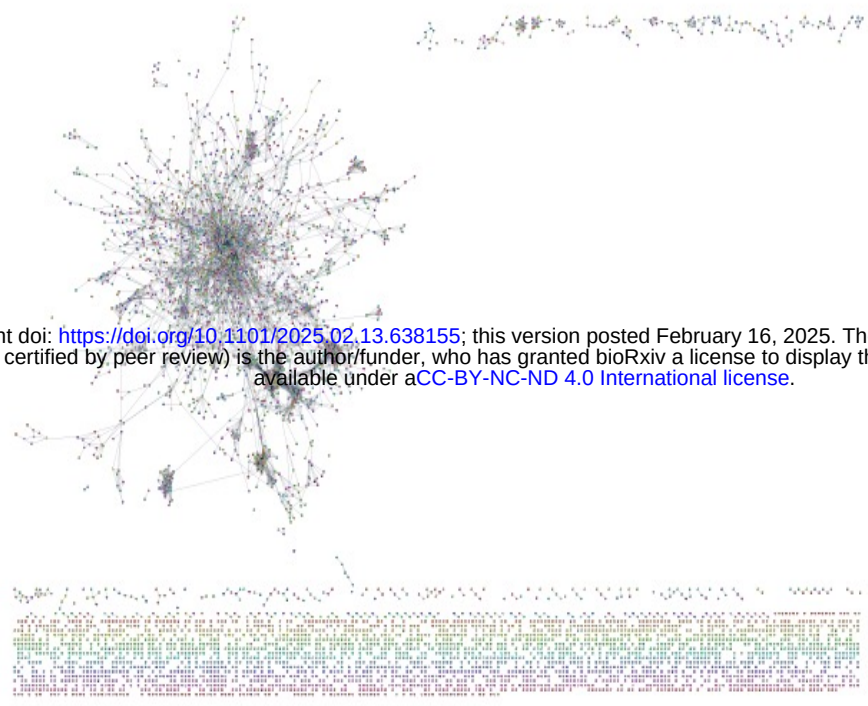

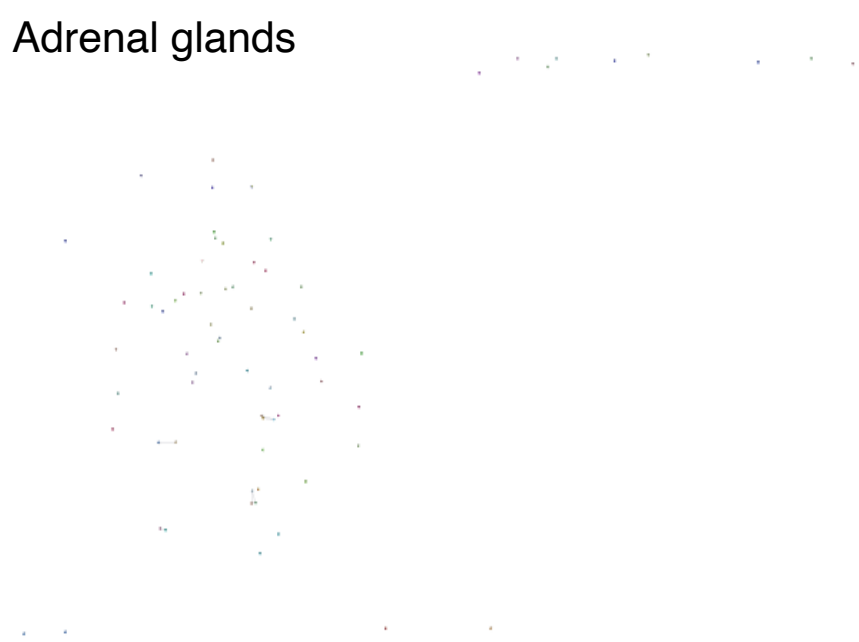

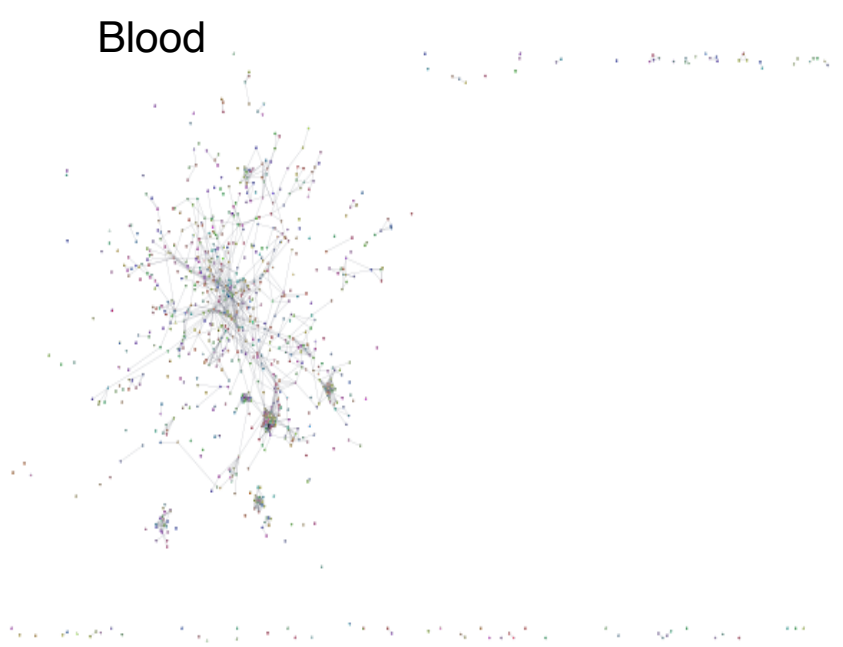

Nuclear protein species expressed in HEK293T cells are most similar to those expressed in the human nervous system.

Supplementary Figure 2

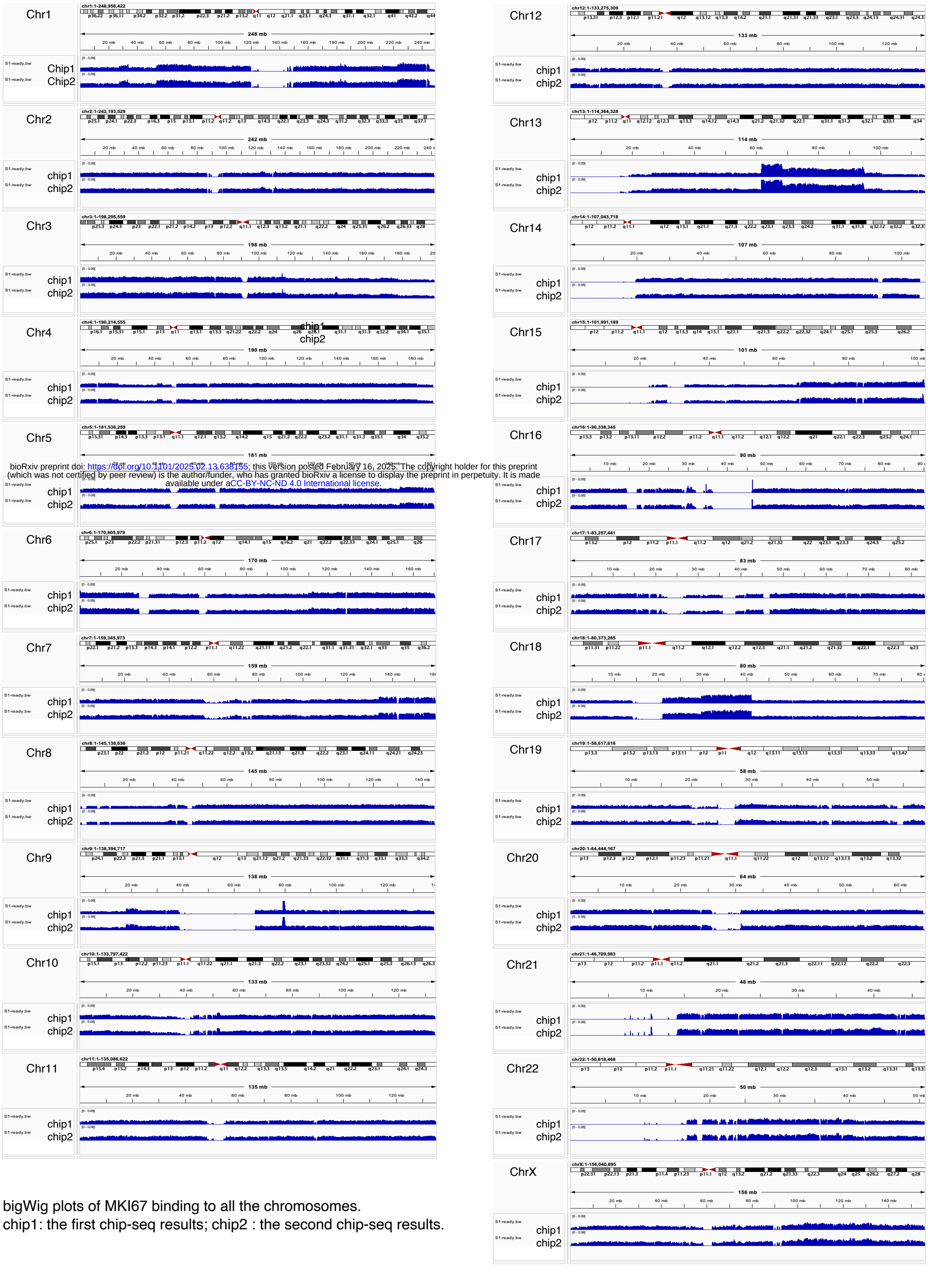

bigWig plots of MKI67 binding to all the chromosomes.
chip1: the first chip-seq results; chip2 : the second chip-seq results.

Supplemental Figure 3

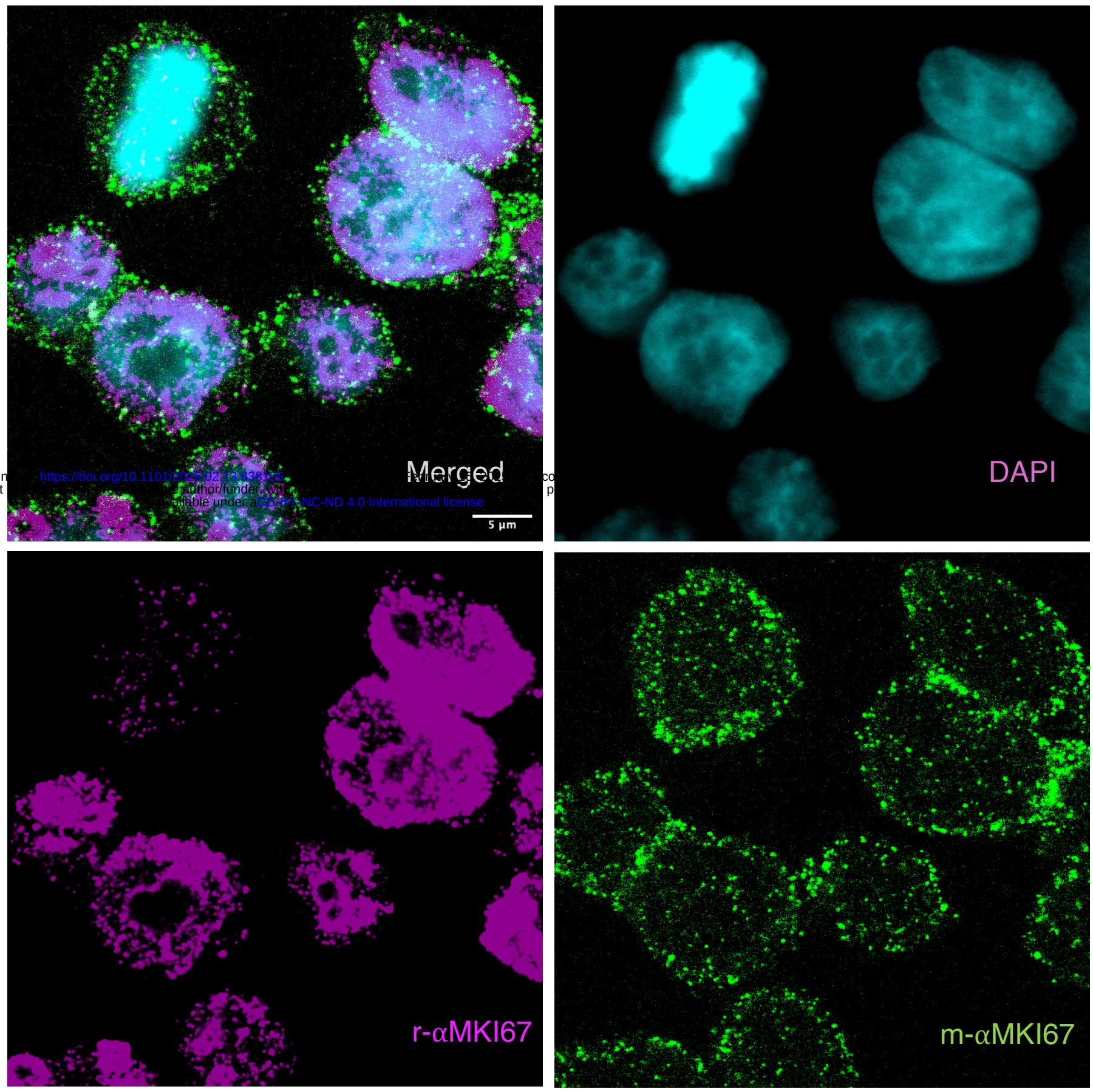

The anti-MKI67 (r- **α**MKI67) antibody detected only 7% of mitotic MKI67 compared to interphase MKI67, based on the following calculation: [(r-αMKI67 signal/ m- αMKI67 signal) in mitotic cells] / [(r- αMKI67 signal/ m- αMKI67 signal) in interphase cells]. On the other hand, the number of mitotic cells was 7% compared to the number of interphase cells in our randomly proliferating cultures. Thus, we estimate that the noise from mitotic cells affecting the chip-seq result Was 0.42% (0.07 x 0.06 x 100), which has virtually no real effect on our results.
The images for MKI67 were taken with overexposure for our eyes to be able to see the low signal from the mitotic cell.

Supplemental Figure 4 for Figure 2

The number to the left of the chromosome locus indicate the total reads of the MKI67 binding to the peak region.

G7lh MKI67-chr7-left wing, high

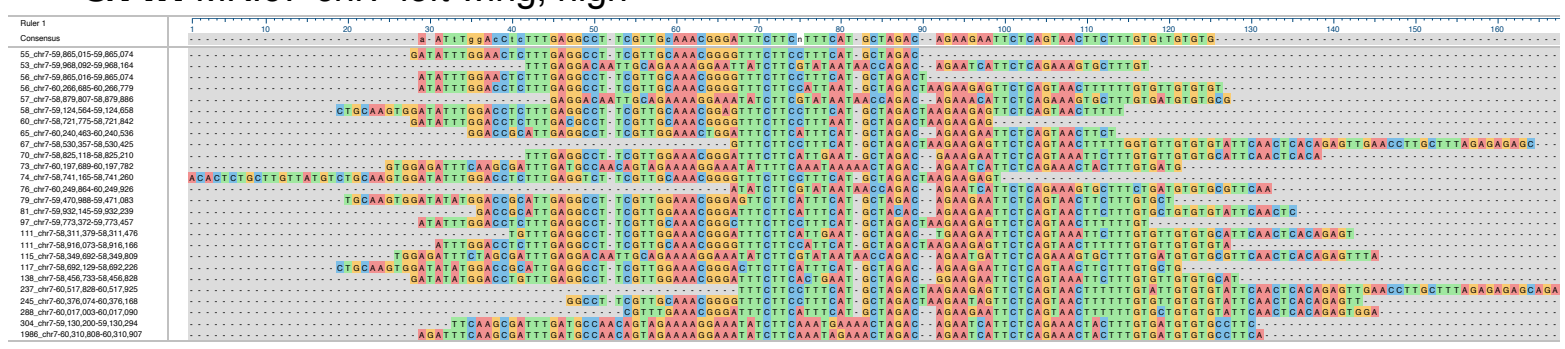

H7rh MKI67-chr7-right wing, high

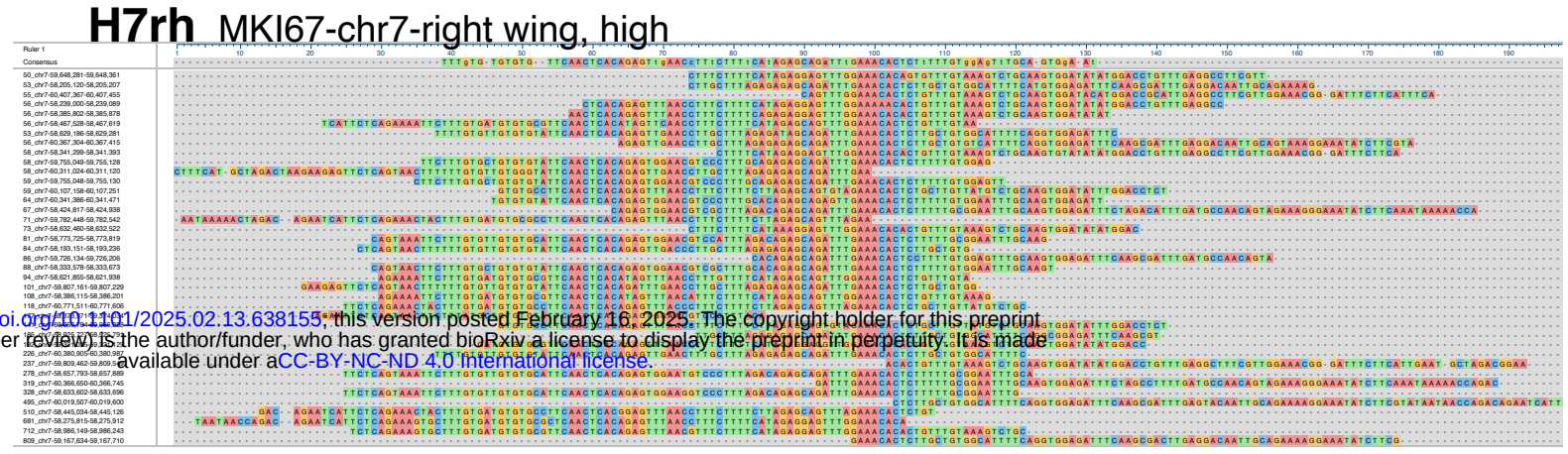

G13rh MKI67-chr13-right wing, high

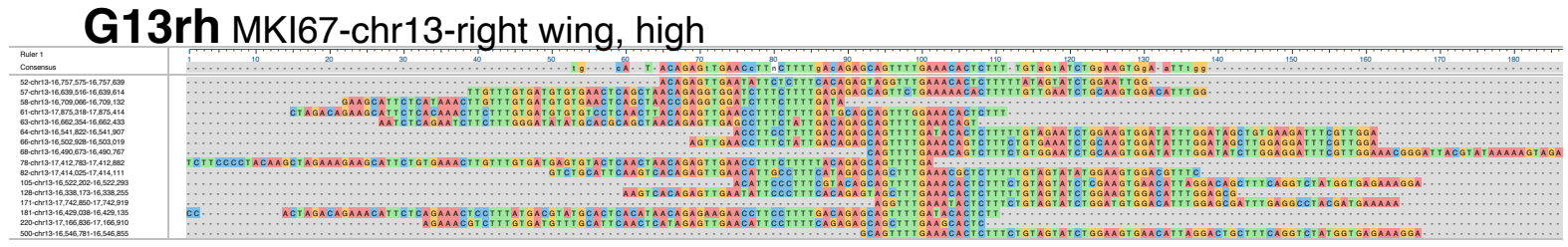

H13lh MKI67-chr13-left wing, high

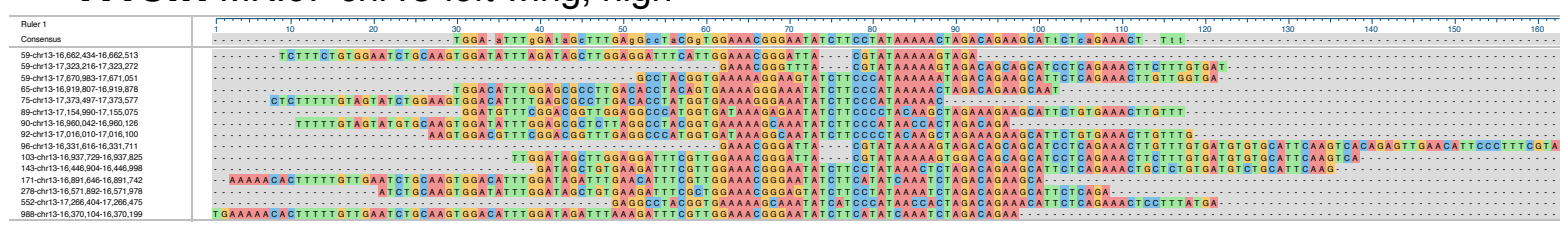

H7rl MKI67-chr7-right wing, low

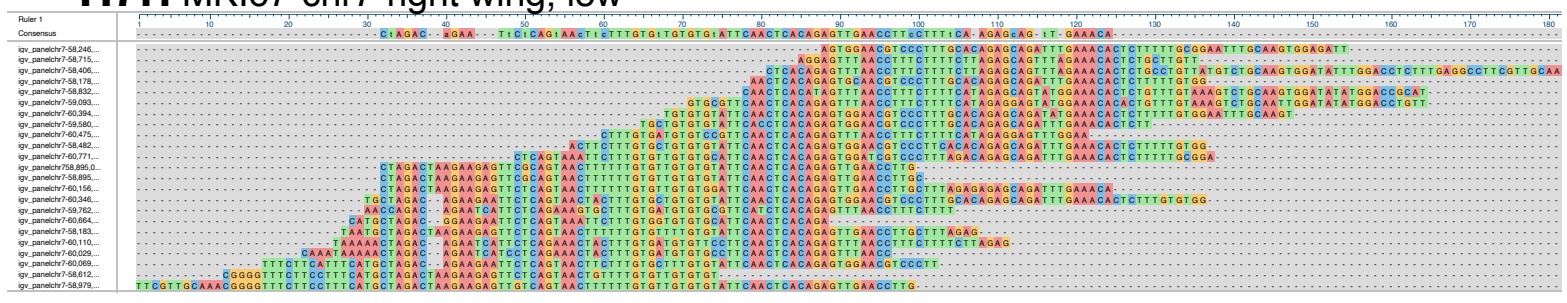

G7fl MKI67-chr7-TGTG-far wing, low

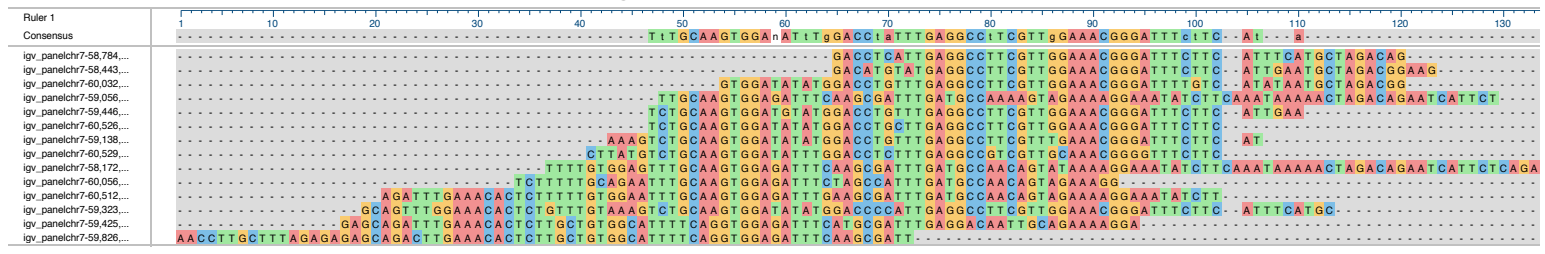

Supplemental Figure 5

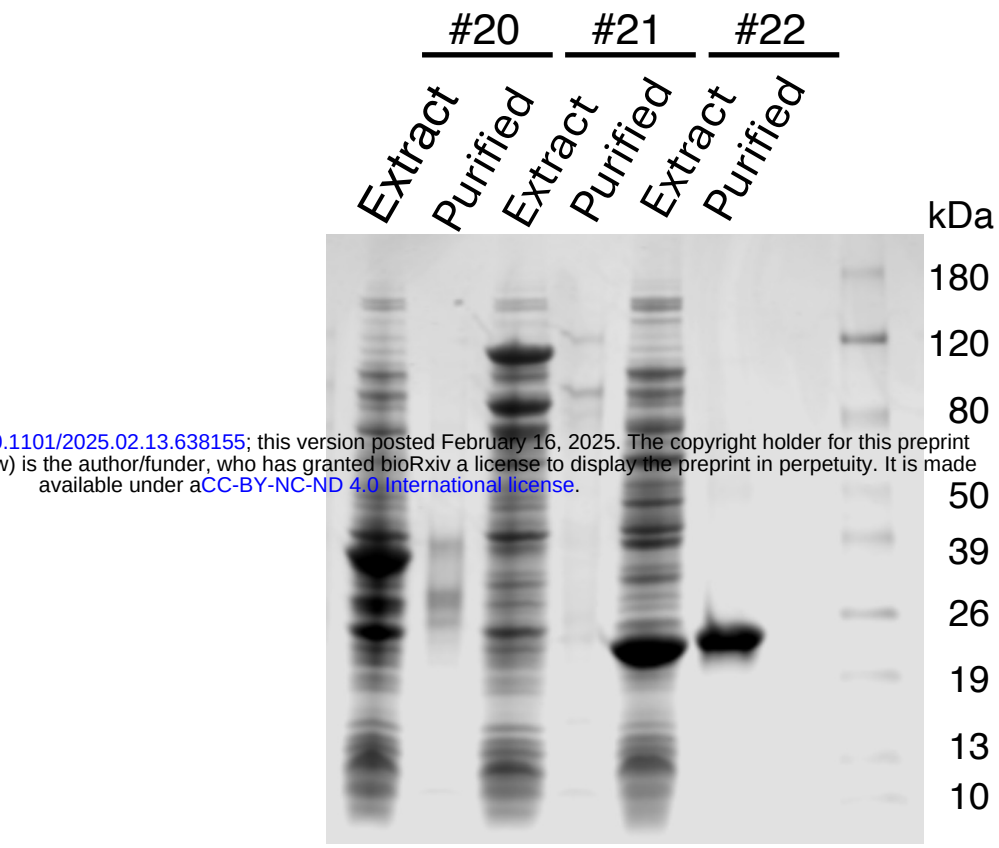

Affinity purified probes expressed in E. *coli* using their C-terminal 6x His tag.
Purified probes, #20 and #21, contained smaller fragments but were otherwise pure.

Complementary Figure 6 for Figure 4

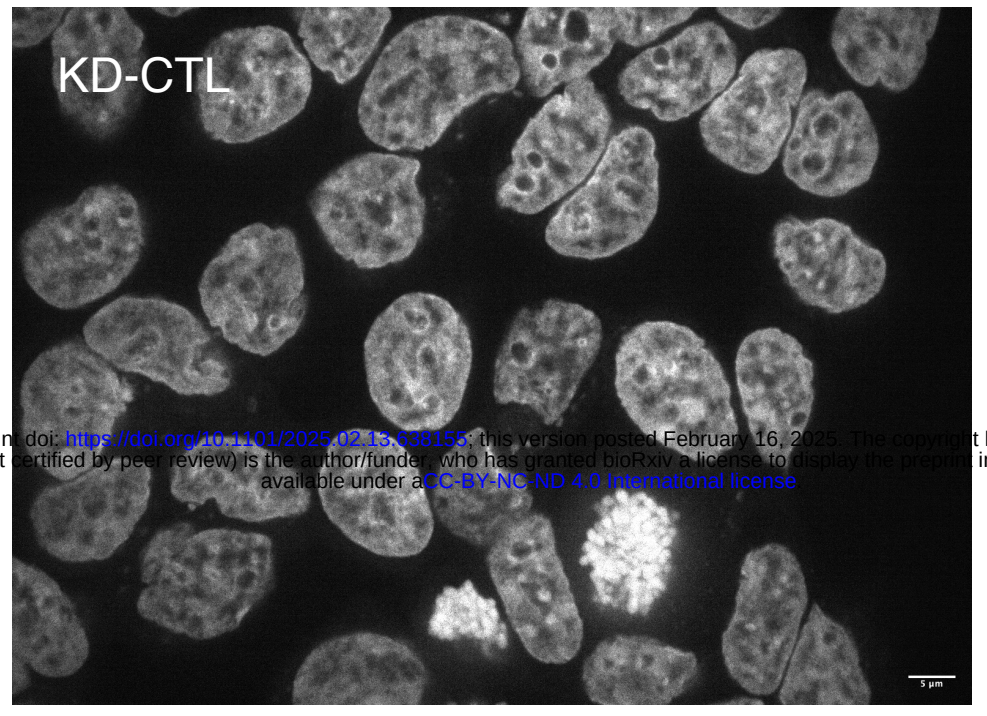

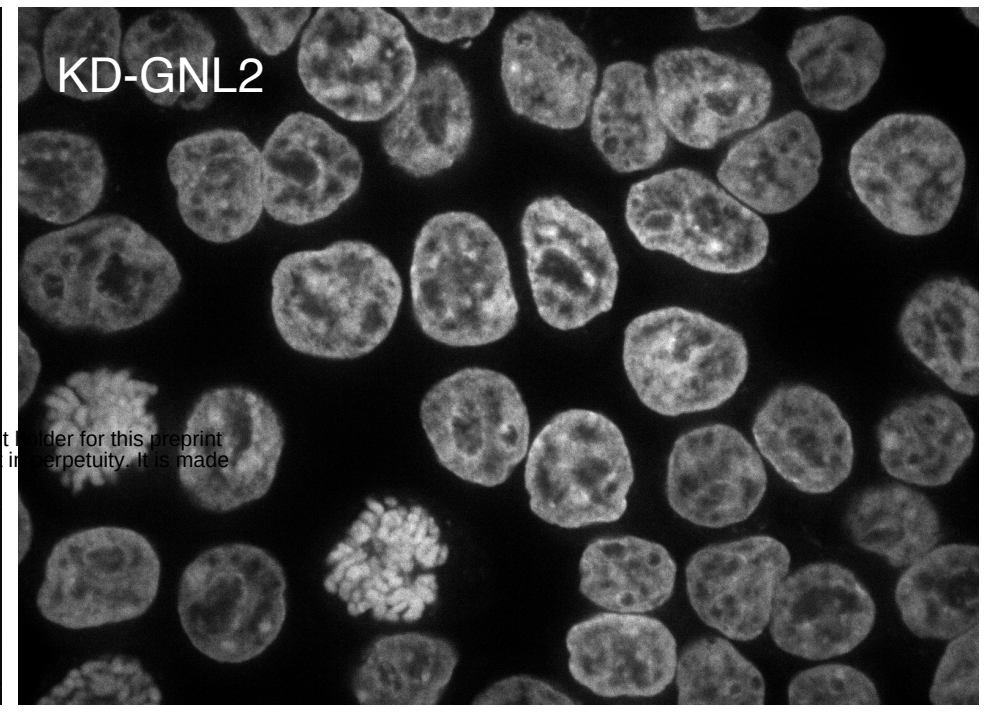

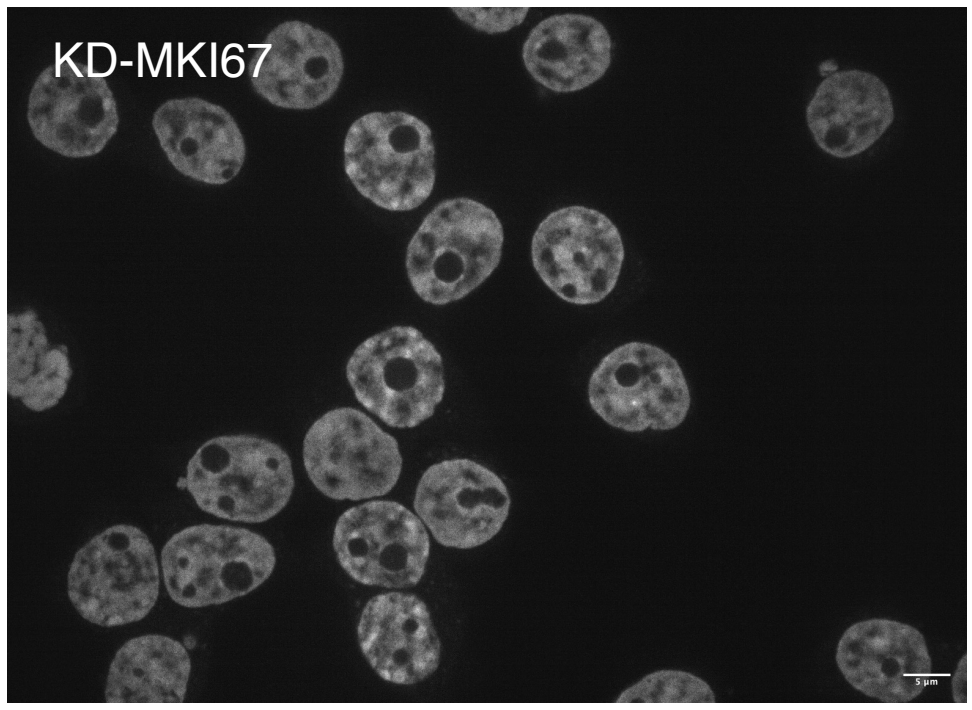

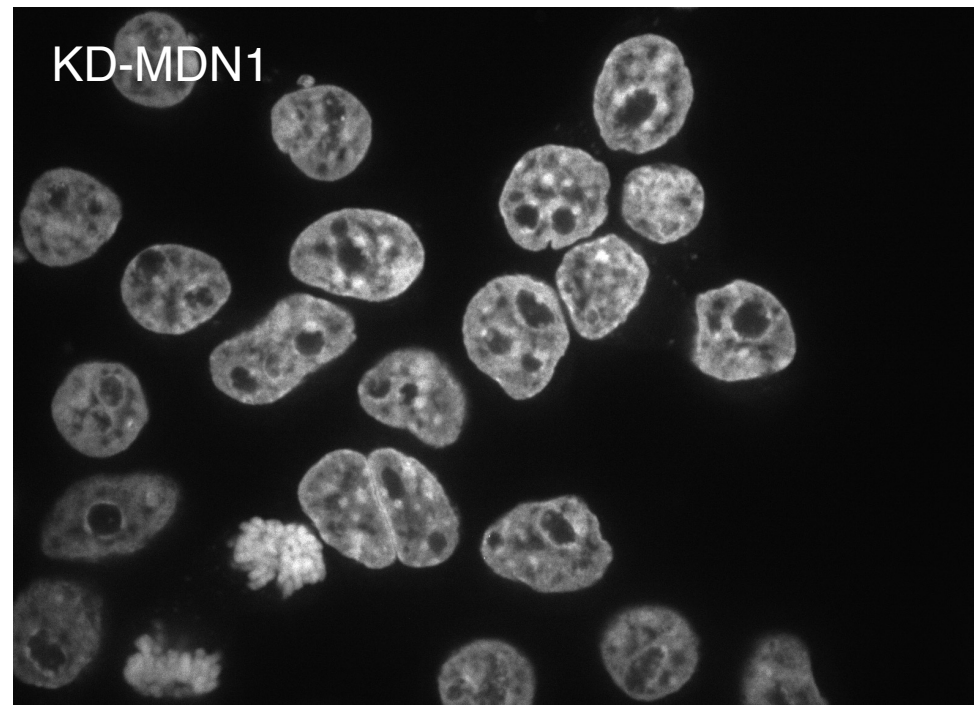

Supplemental Figure 7

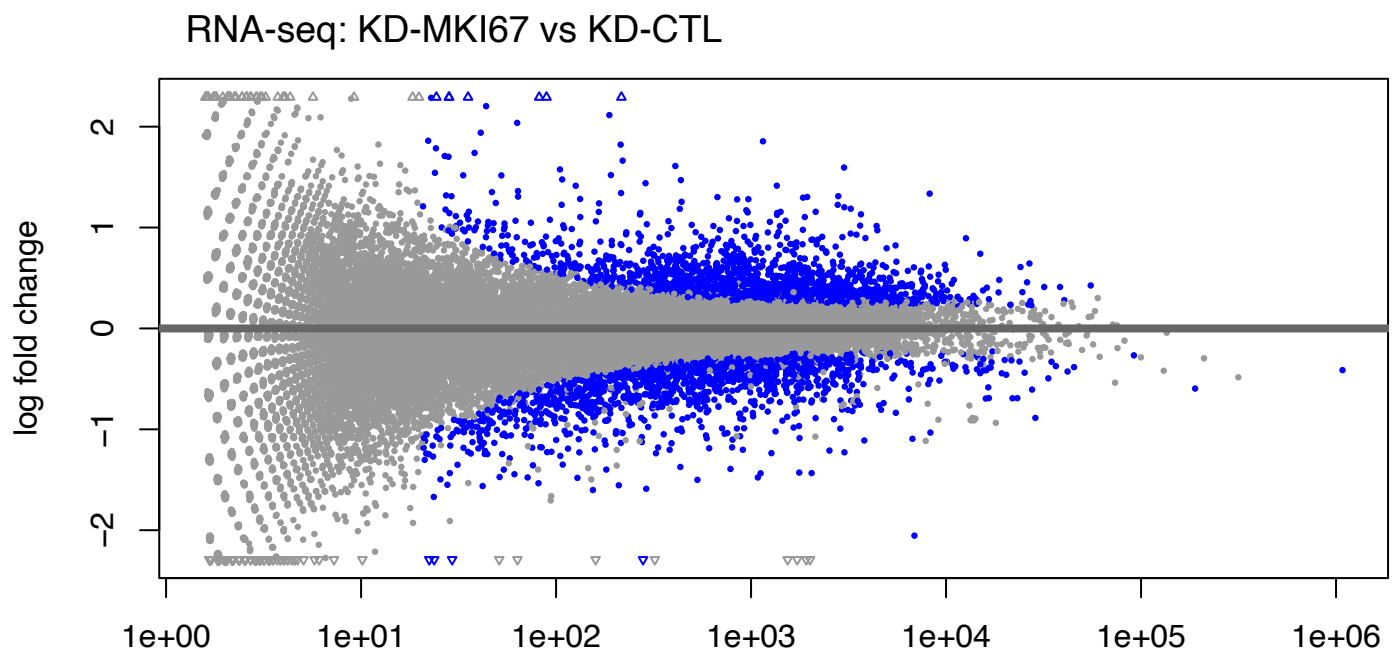

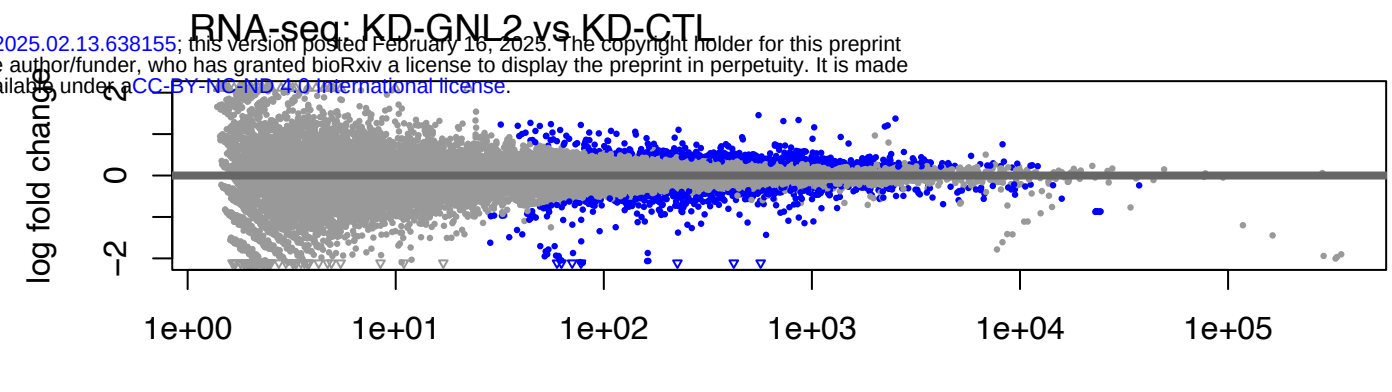

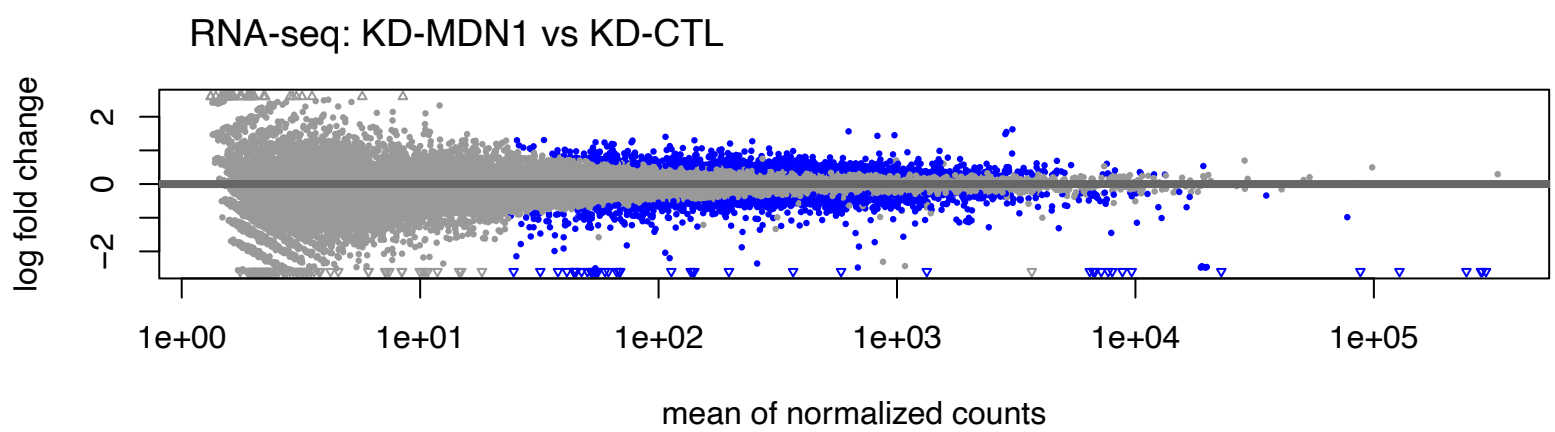

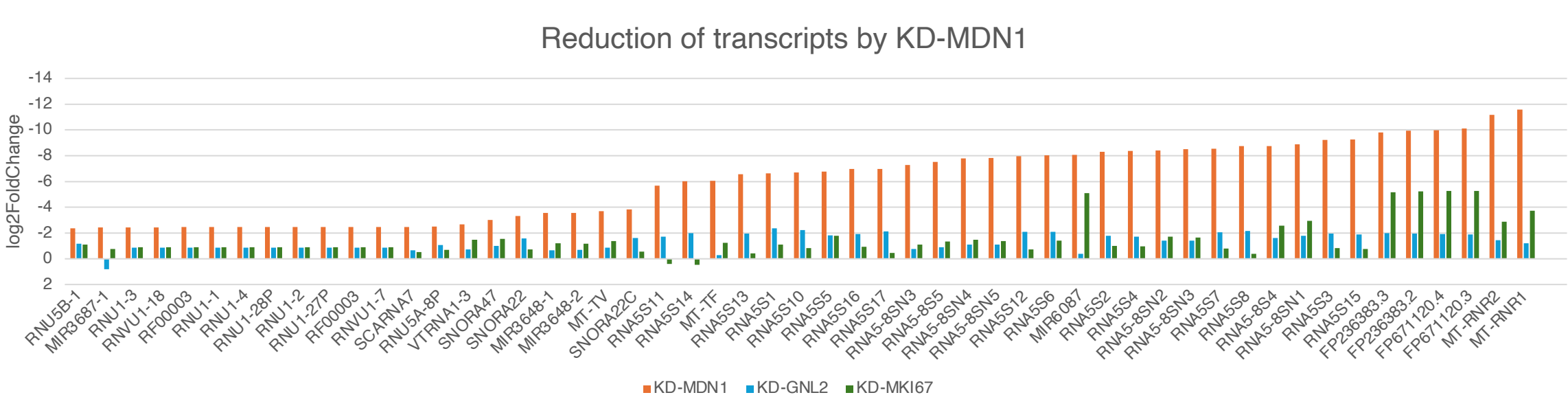

Supplementary Figure 8 for Figure 6

A, HEK7

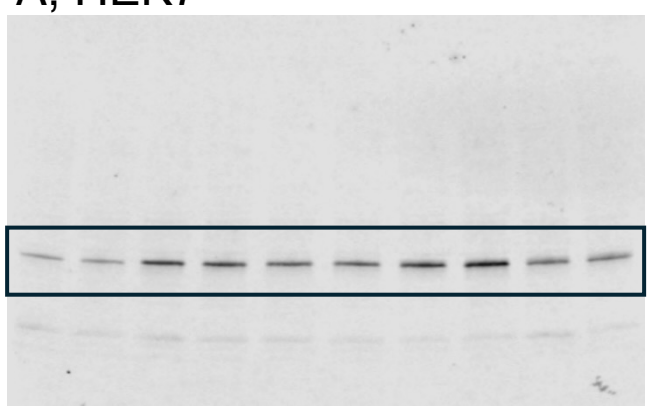

D, HEK7

H, HEK7

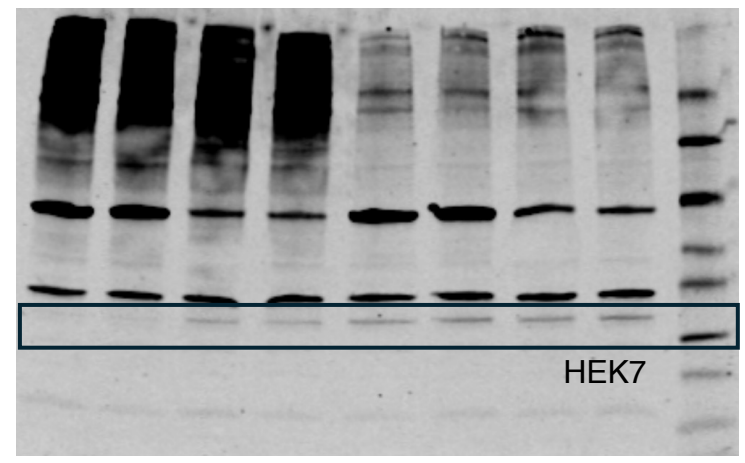

B, YTHDC2

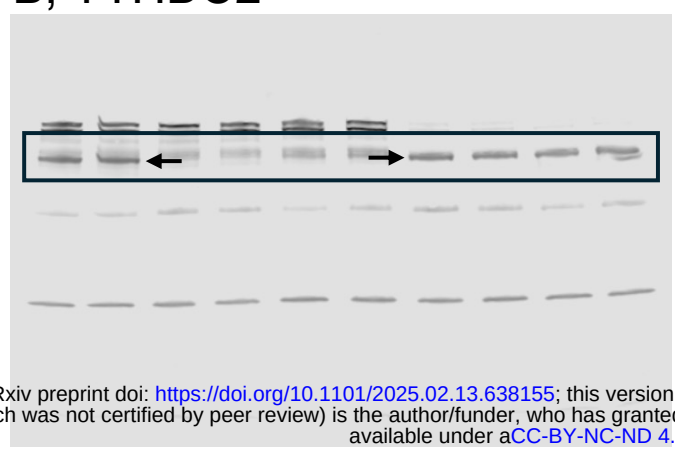

E, YTHDC2

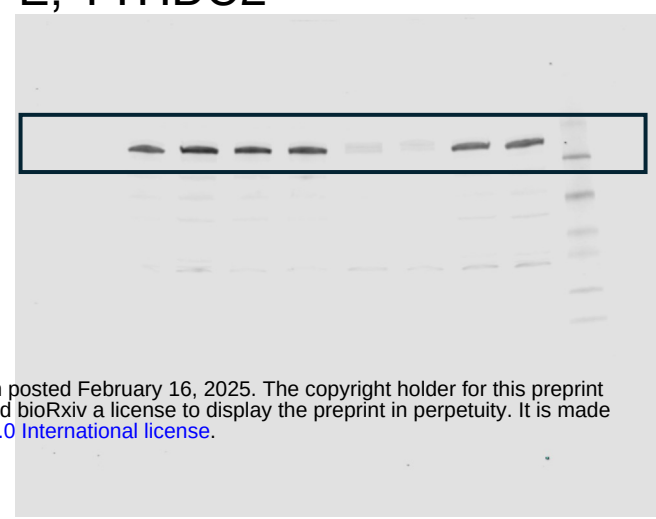

I, G3BP1

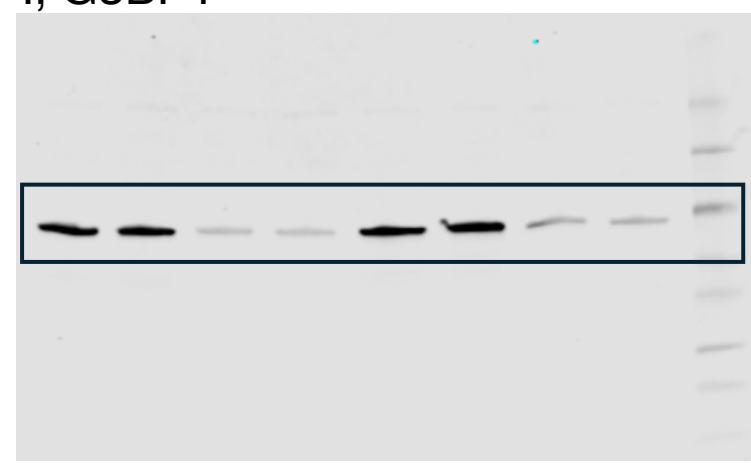

C, CNOT1

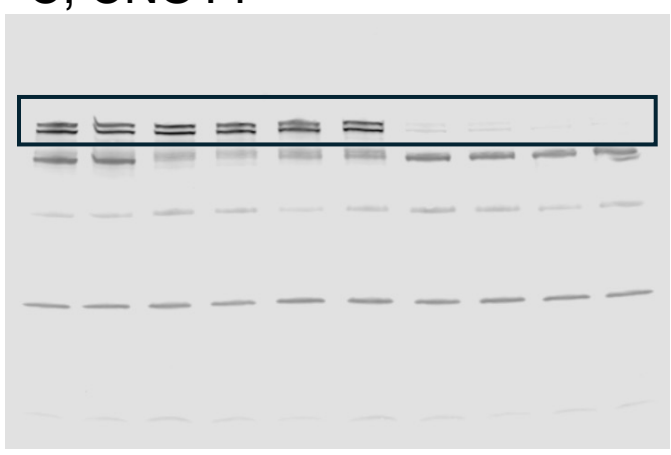

F, CNOT1

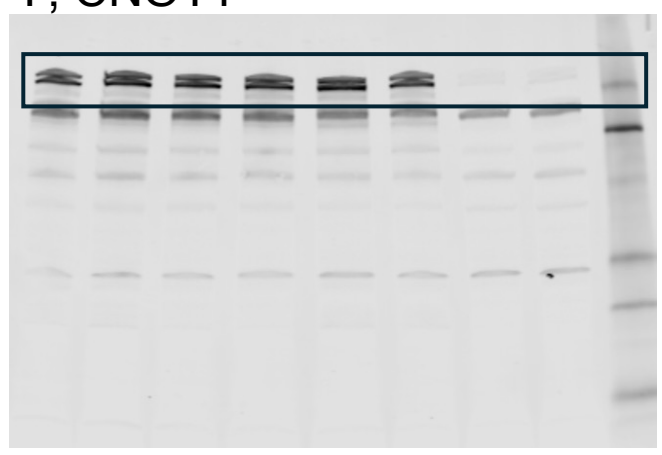

J, G3BP2

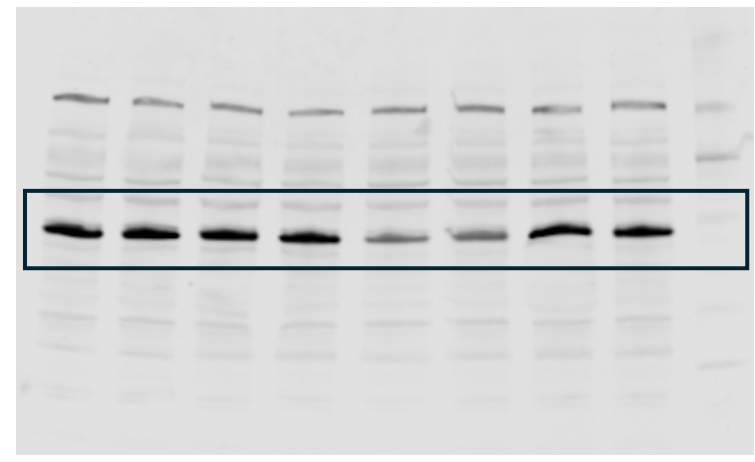

G, MKI67

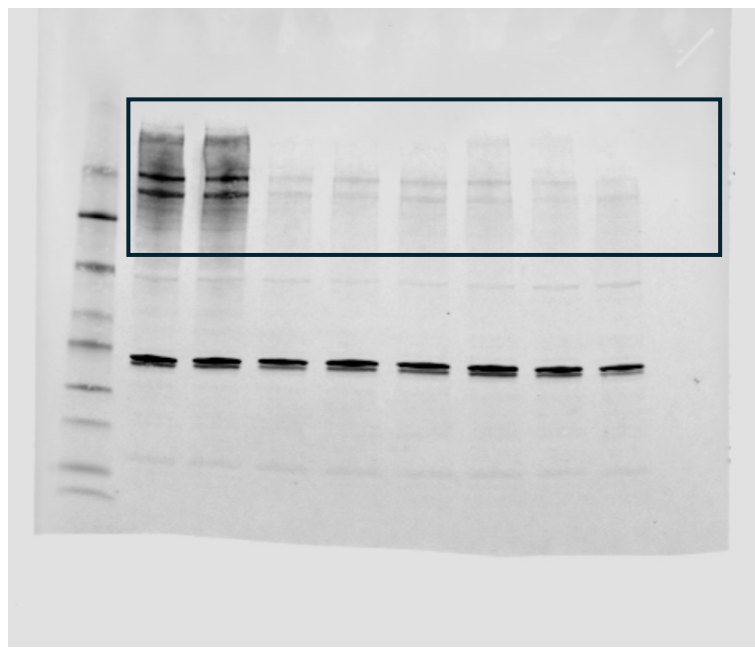

K, MKI67

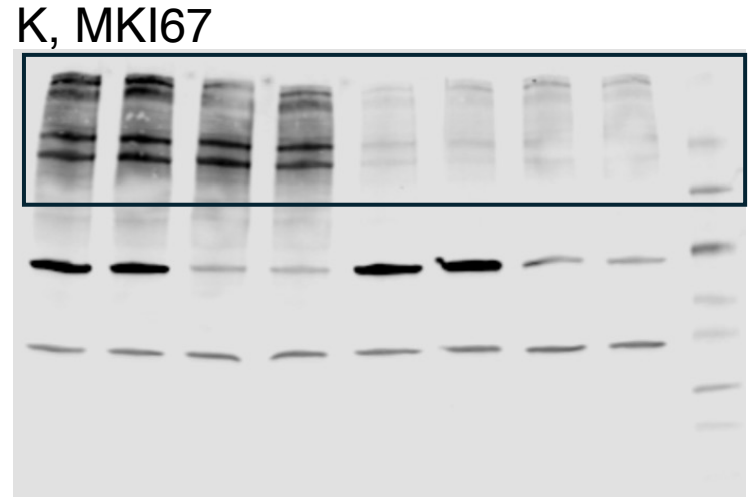

Framed selections were used for Figure 8.
Some of the images contain unwanted bands. This is due to Western blotting with 2 different primary antibodies or subsequent Western blotting on a PVDF membrane that blotted for other proteins.

Supplemental Figure 9 for Figure 7

A, UCN13A

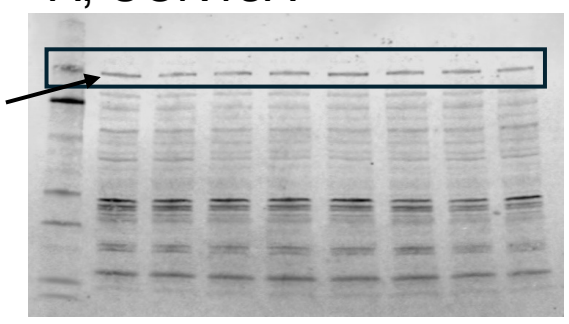

B, UCN13A

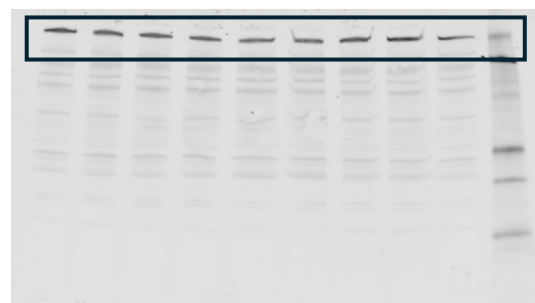

D and E,UNC13A

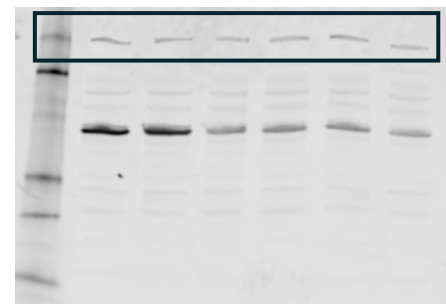

F, UNC13A

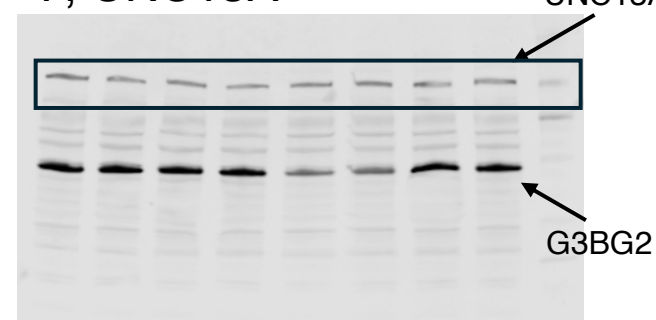

C, G3BP1

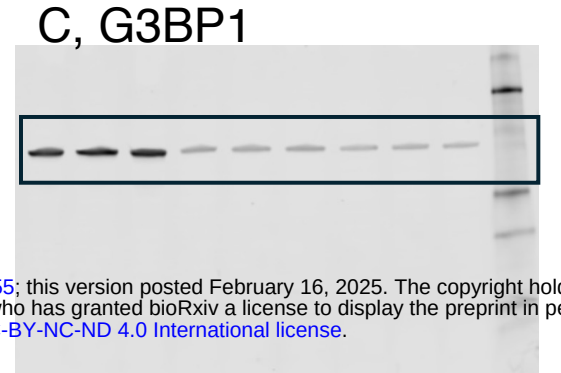

D and E, G3BP2

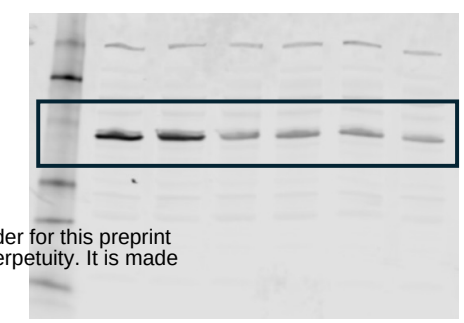

G, G3BP1

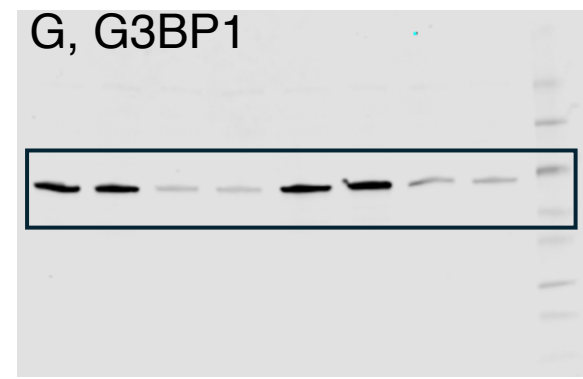

H, UNC13A

1 1 1 2 2 2 3 3 3 M

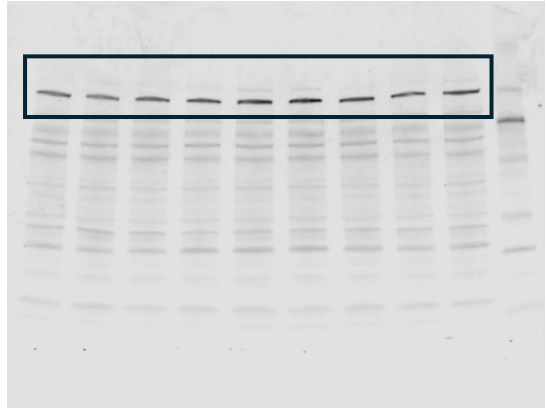

I, FMR1

1 1 1 2 2 2 3 3 3 M

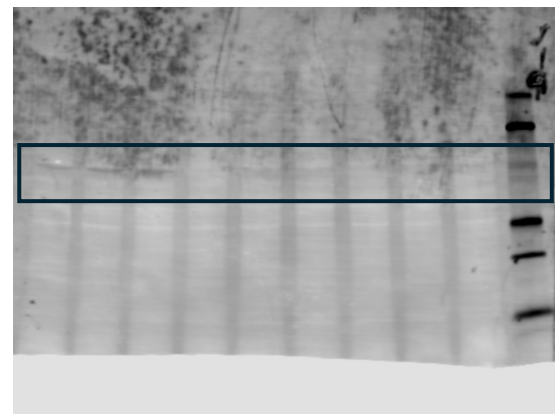

J, KMI67

1 1 1 2 2 2 3 3 3 M

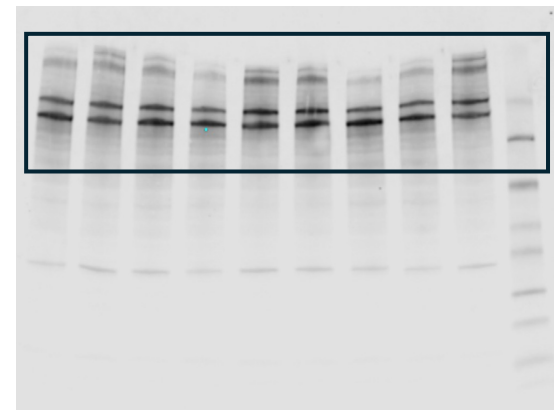

H, UNC13A

4 4 4 5 5 5 6 6 6 M

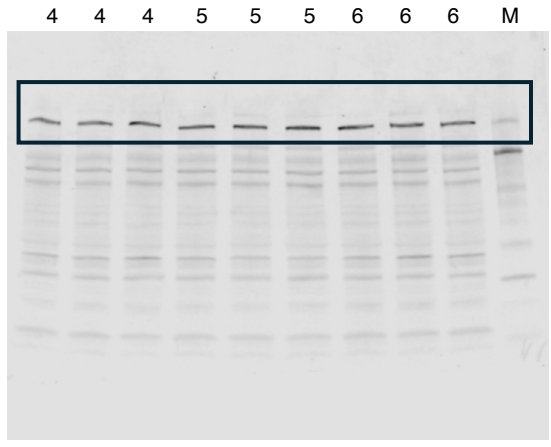

I, FMR1

4 4 4 5 5 5 6 6 6 M

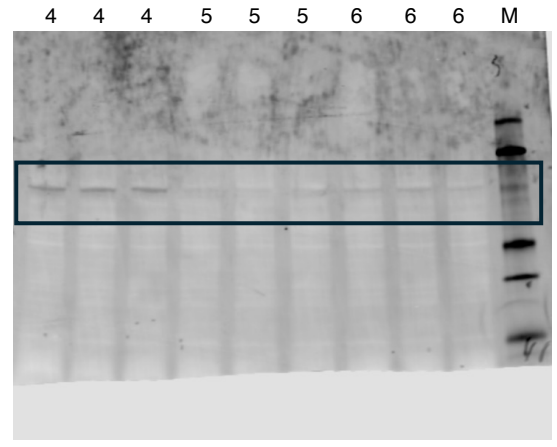

J, MKI67

4 4 4 5 5 5 6 6 6 M

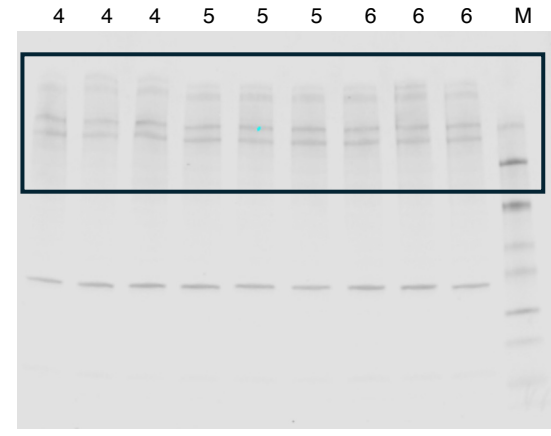

Framed selections were used for Figure 9.
Some of the images contain unwanted bands. This is due to Western blotting with 2 different primary antibodies or subsequent Western blotting on a PVDF membrane that blotted for other proteins.

Supplemental Fig. 10

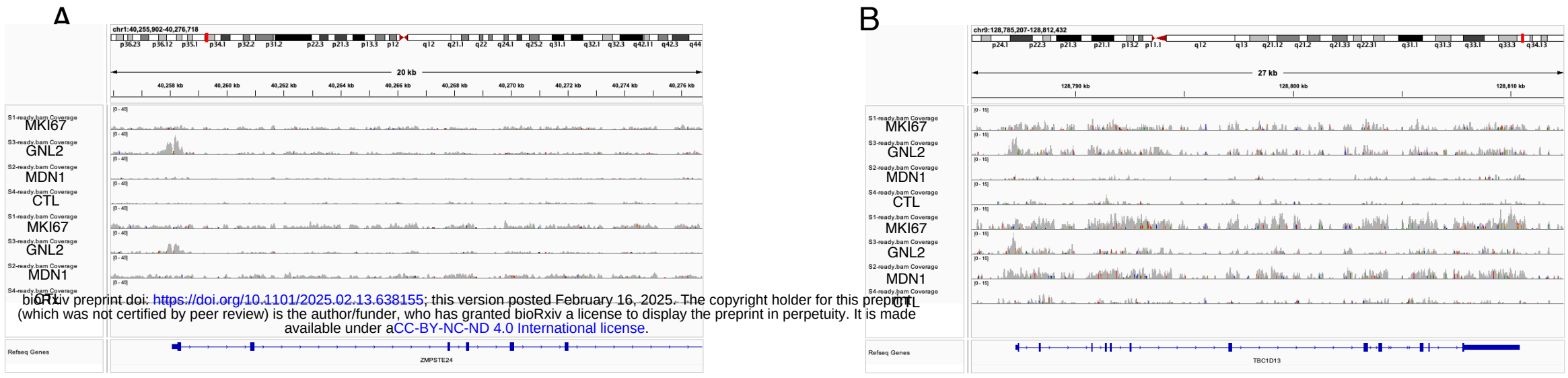

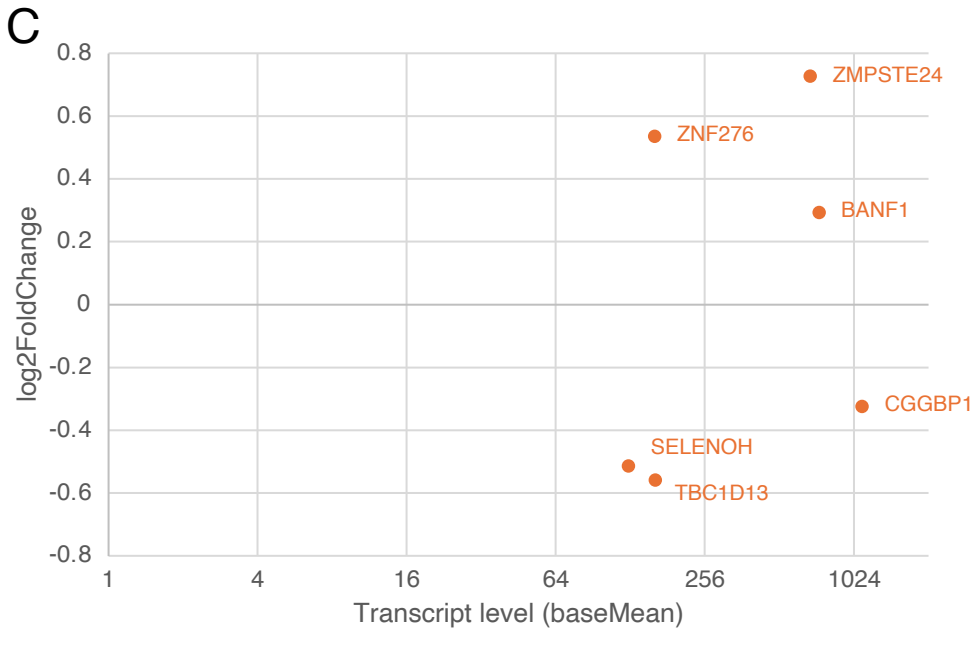

Up- and down-regulation of transcripts of the genes whose promoter regions are not bound by GNL2.

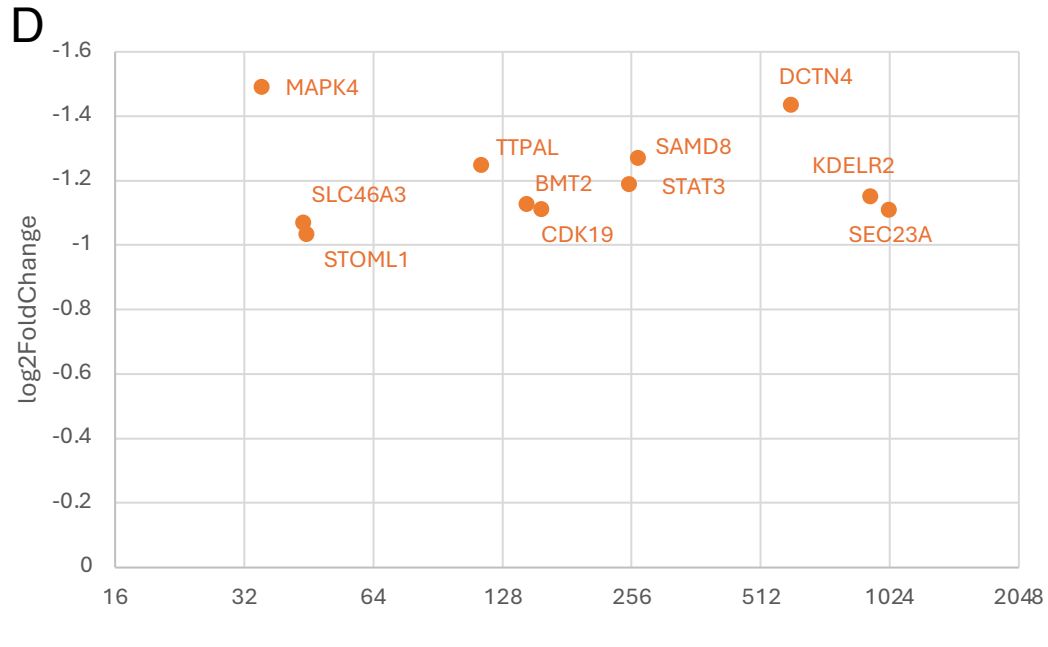

Downregulation of transcripts of the genes whose promoter regions are not bound by GNL2.

Supplemental Figure 11

A

Mplot of transcripts from genes whose promoters are bound by MDN1

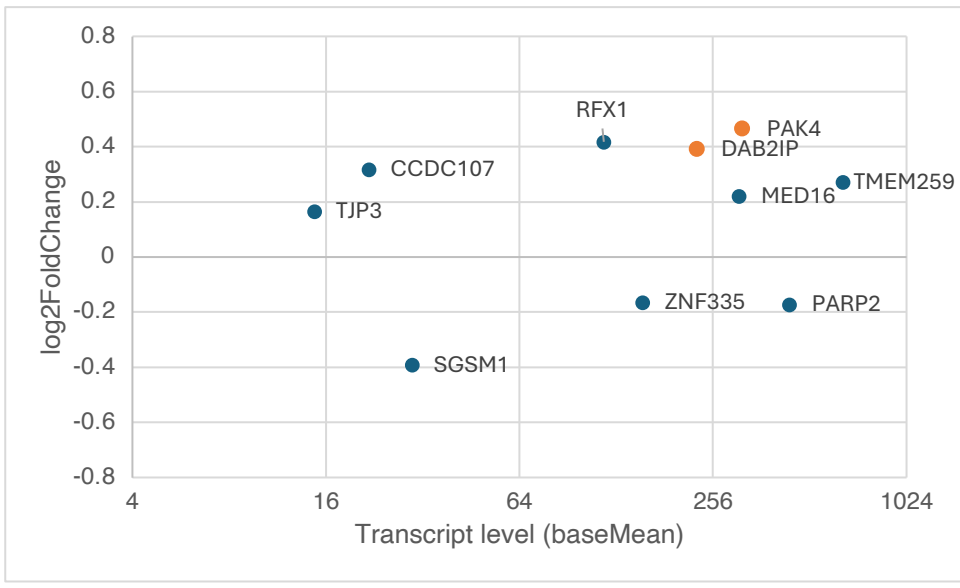

Padj < 0.01 for PAK4 and < 0.05 for BAB2IP, and > the other transcripts

B

MDN1 binding to promoter region of the *PAK4*

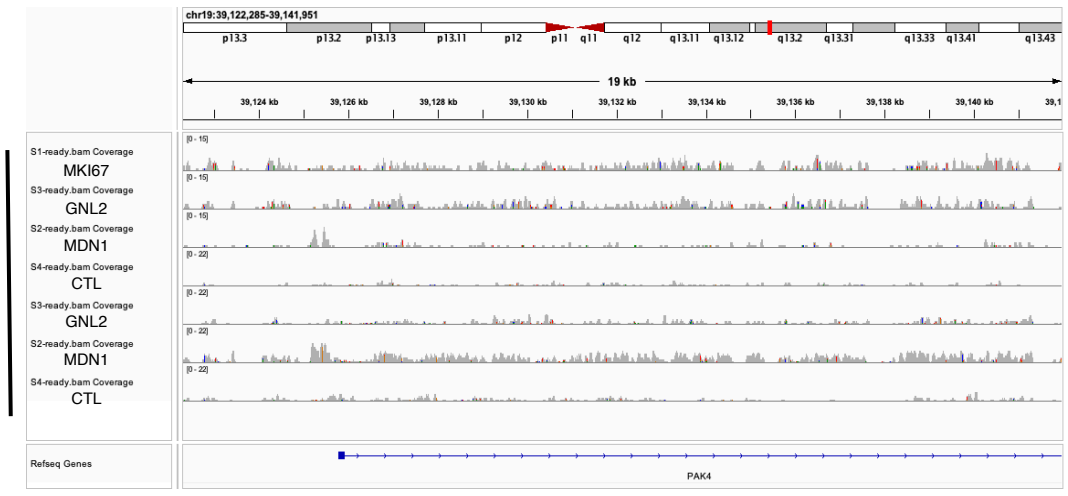

C

MDN1 binding to the *RNY3* and transcript levels of the gene

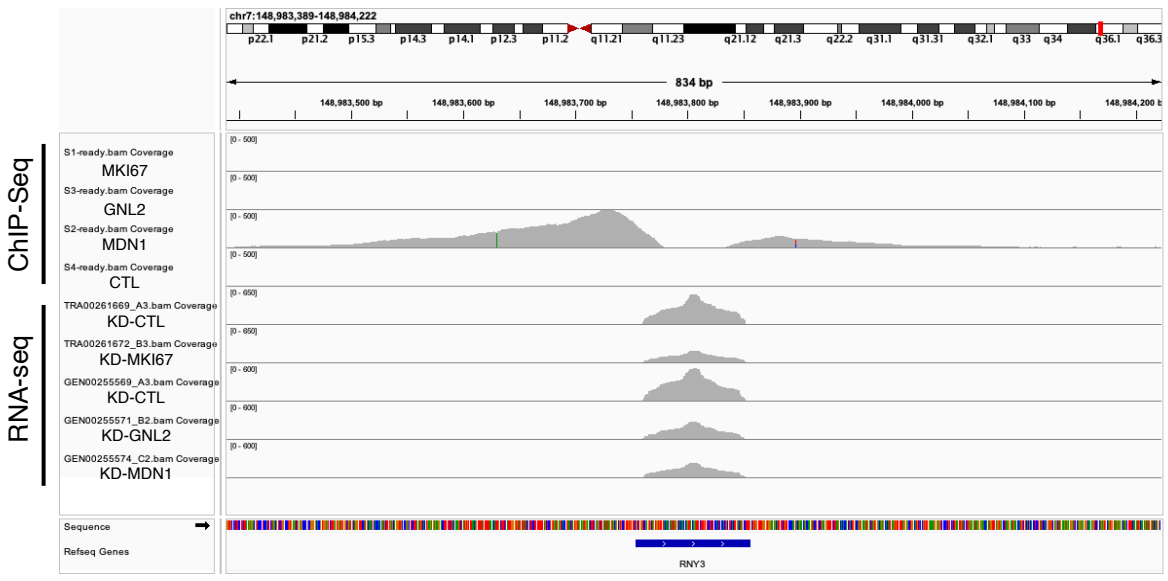

D

MDN1 binding to the *RMRP* and transcript levels of the gene

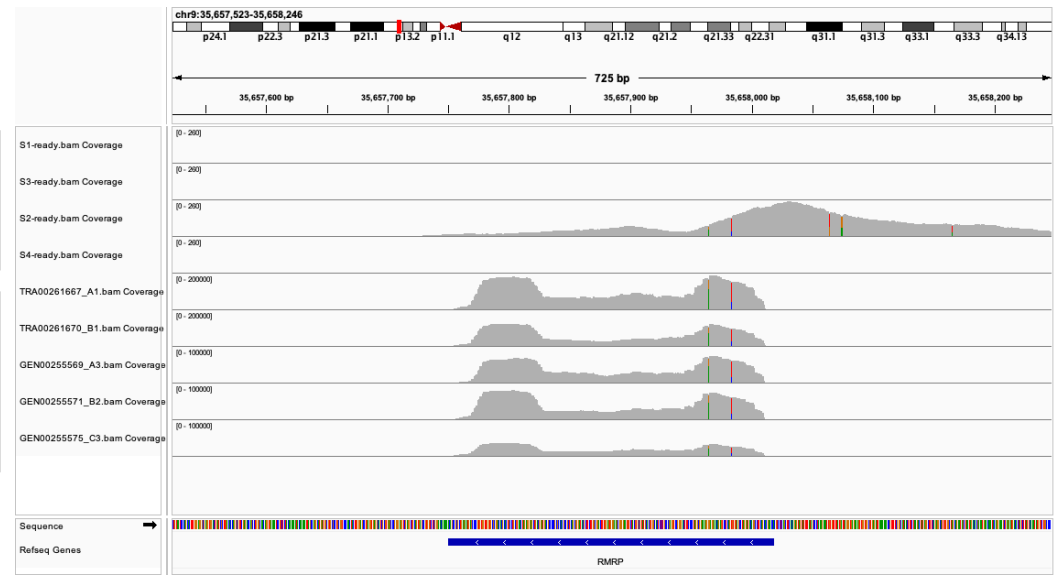

E

MDN1 binding to the *RNU6-2* and transcript levels of the gene

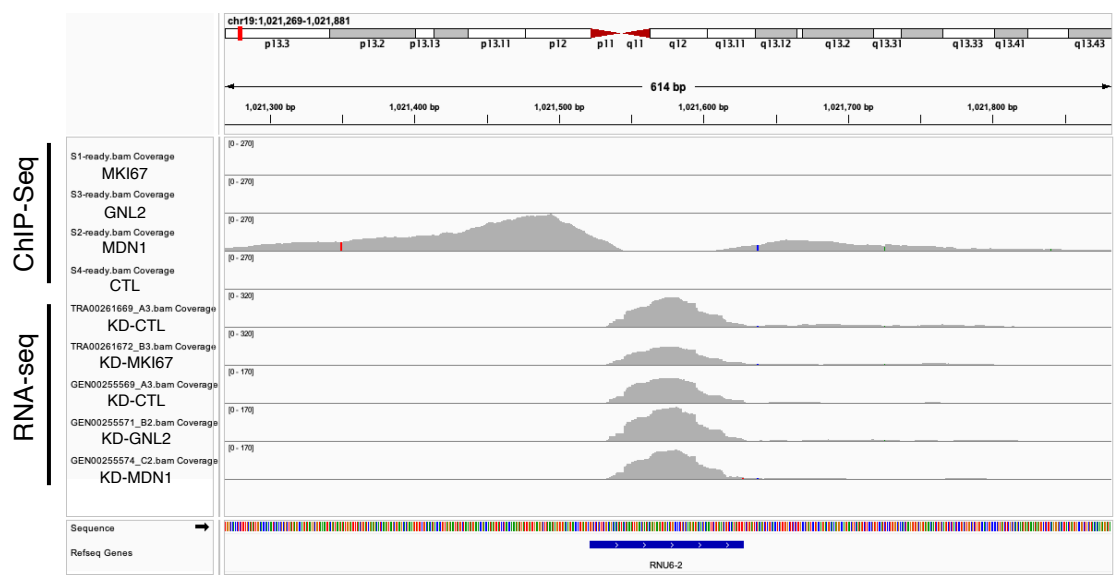

F

MDN1 binding to the *RN7SK and* transcript levels of the gene

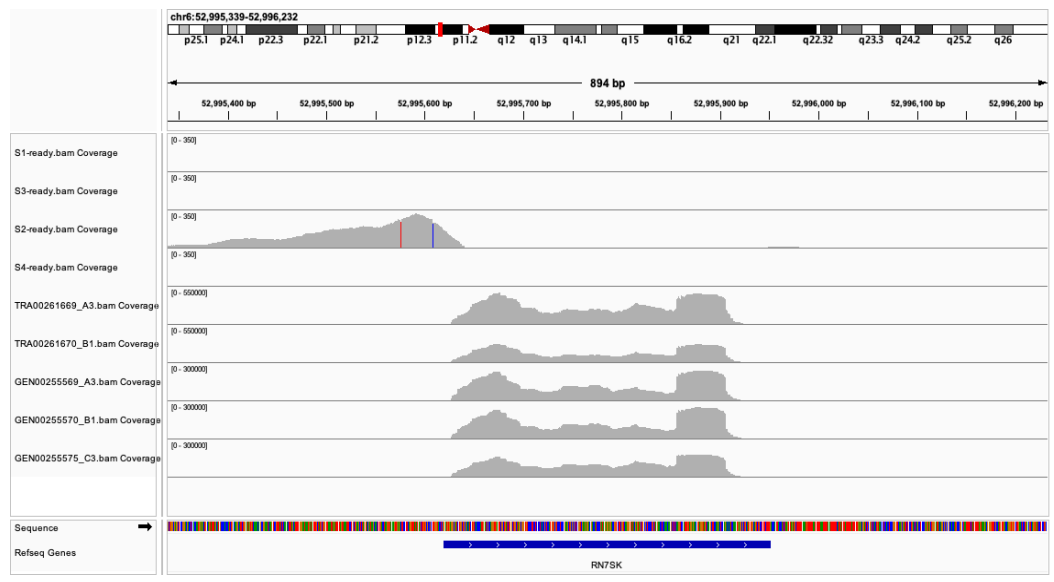

Supplemental Figure 12

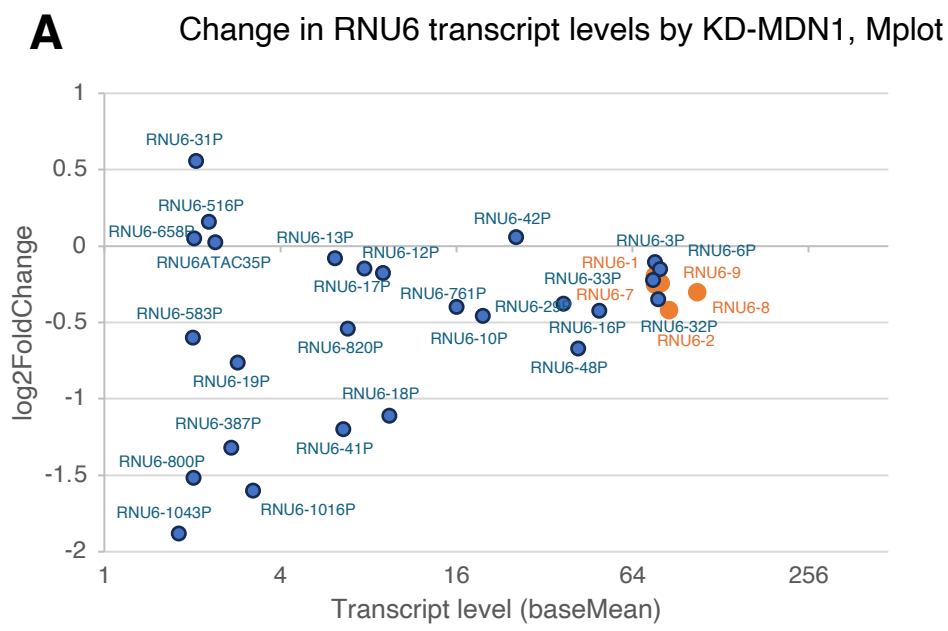

Changes by KD-MDN1 in *RNU* transcript levels (orange) are not different from those in the pseudogenes.

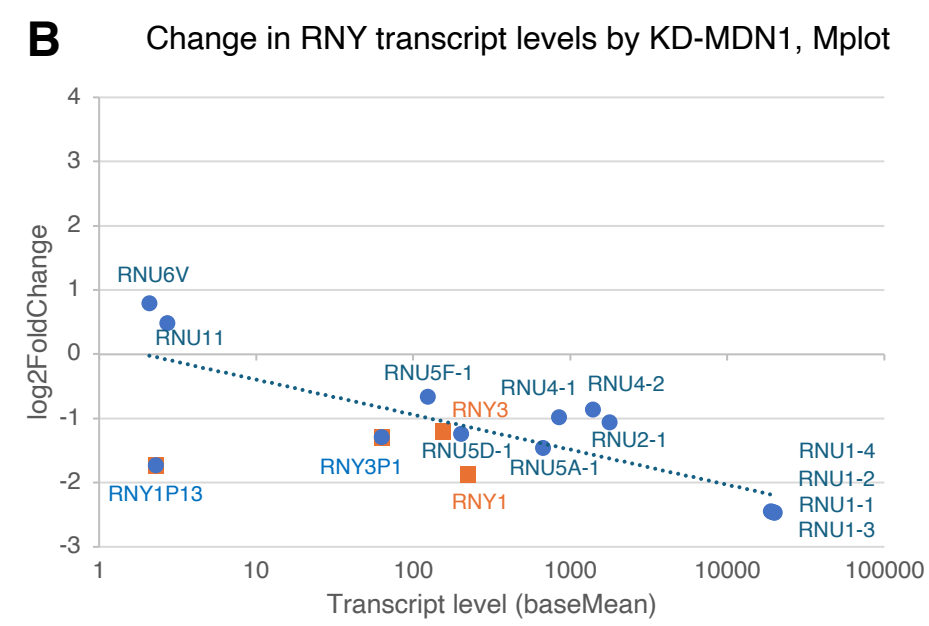

Changes by KD-MDN1 in RNY transcript levels (orange) are not different from those in the pseudogenes and RNU genes.

Supplemental Table 1. HOMER consensus sequences to which MKI67 binds

Motif	Sequnce	reverse complement	p-value	% of Target sequences with motif	% of Background sequences with motif
1	(C/G)GAGTGGA	TCCACTC(C/G)	1.00E-143	66.1	2.45
2	TGCAATTG	CAATTGCA	1.00E-63	46.11	4.15
3	TCCGTTCC	GGAACGGA	1.00E-35	21.67	1.24
4	CTAGACAG	CTGTCTAG	1.00E-31	18.89	1.03
5	GAAACACT	AGTGTTTC	1.00E-27	17.22	1.05
6	TTGTGATG	CATCACAA	1.00E-26	20	1.7
7	ATACTTC	GAAGTAT	1.00E-25	16.67	1.05
8	CATTC(G/C)AT	AT(G/C)GAATG	1.00E-25	60.56	23.5
9	GCGGAAT(T/C/G)	(A/G/C)ATTCCGC	1.00E-17	18.89	2.83
10	TCT(C/G)AGAA	TTCT(C/G)AGA	1.00E-15	13.89	1.52
11	(A/G)GTT(A/T)AAC	GTT(A/T)AAC(C/T)	1.00E-13	9.44	0.68
12	ACAGAGCA	TGCTCTGT	1.00E-13	16.67	2.97
13	CTACTGTT	AACAGTAG	1.00E-12	8.33	0.58
14	GATTTCAA	TTGAAATC	1.00E-11	7.78	0.65
15	G(A/C)(T/C)TACGT	ACGTA(A/G)(G/T)C	1.00E-10	13.89	2.36
	These motiefs are derived from chip-seq 1.				
	Sequences in red are present in units of the chr7 and chr13 consensus sequences.				

Supplemental Table 2A

Transcripts whose levels were altered by KD-MKI67.
Left: reduced; right: increased.

gene ID	gene symbol	FoldChange by KD-MKI67	gene ID	gene symbol	FoldChange by KD-MKI67
ENSG00000035862	TIMP2	0.49	ENSG00000231194	FARP1-AS1	23.9
ENSG00000184489	PTP4A3	0.49	ENSG00000077080	ACTL6B	22.3
ENSG00000261572	AC097639.1	0.49	ENSG00000278012	AL031658.2	17
ENSG00000238251	AL133477.1	0.49	ENSG00000264810	MIR4441	15.7
ENSG00000262089	AC040977.1	0.49	ENSG00000182315	MBD3L3	15.7
ENSG00000138772	ANXA3	0.49	ENSG00000196092	PAX5	15
ENSG00000066248	NGEF	0.49	ENSG00000206913	RF00409	14
ENSG00000279662	AC131649.2	0.49	ENSG00000201136	RNU6-353P	13.2
ENSG00000159648	TEPP	0.49	ENSG00000281756	C2-AS1	13.2
ENSG00000229191	AL358473.1	0.49	ENSG00000255571	MIR9-3HG	12.5
ENSG00000088881	EBF4	0.49	ENSG00000284603	AC105233.4	11.5
ENSG00000178082	TWF1P1	0.49	ENSG00000244094	SPRR2F	10.7
ENSG00000228109	MELTF-AS1	0.49	ENSG00000253576	AF181450.1	10.6
ENSG00000162772	ATF3	0.49	ENSG00000135625	EGR4	10.5
ENSG00000200997	RNU1-85P	0.49	ENSG00000254293	AC026688.2	10.5
ENSG00000265692	LINC01970	0.49	ENSG00000104112	SCG3	9.9
ENSG00000268785	RPL7P50	0.48	ENSG00000242175	RN7SL127P	9.7
ENSG00000138378	STAT4	0.48	ENSG00000130477	UNC13A	9.2
ENSG00000203411	RF00017	0.48	ENSG00000288234		7.5
ENSG00000136842	TMOD1	0.48	ENSG00000220937	HNRNPA1P41	7.5
ENSG00000156482	RPL30	0.48	ENSG00000178235	SLITRK1	7.3
ENSG00000021826	CPS1	0.48	ENSG00000260903	XKR7	6.7
ENSG00000100968	NFATC4	0.48	ENSG00000231688	RPL21P43	6.6
ENSG00000172250	SERHL	0.48	ENSG00000277883	NLRP3P1	6.6
ENSG00000278099	RF00003	0.48	ENSG00000089199	CHGB	6.5
ENSG00000206417	H1FX-AS1	0.48	ENSG00000218069	RSL24D1P1	6.3
ENSG00000142227	EMP3	0.48	ENSG00000277200	AC005696.4	6.2
ENSG00000100889	PCK2	0.48	ENSG00000100604	CHGA	5.8
ENSG00000251141	MRPS30-DT	0.48	ENSG00000254515	AP001124.1	5.6
ENSG00000185885	IFITM1	0.48	ENSG00000145113	MUC4	5.4
ENSG00000237343	AC246785.3	0.48	ENSG00000227845	AL627223.1	5.3
ENSG00000287262		0.48	ENSG00000230914	AC004840.1	5
ENSG00000110697	PITPNM1	0.48	ENSG00000173811	CCDC13-AS1	4.9
ENSG00000231856	AL162377.1	0.48	ENSG00000151615	POU4F2	4.8
ENSG00000184451	CCR10	0.48	ENSG00000144406	UNC80	4.8
ENSG00000253123	AC091182.1	0.48	ENSG00000158445	KCNB1	4.6
ENSG00000141968	VAV1	0.48	ENSG00000249465	RBMXP4	4.5
ENSG00000281912	LINC01144	0.48	ENSG00000155093	PTPRN2	4.5
ENSG00000249087	ZNF436-AS1	0.48	ENSG00000188306	LRRIQ4	4.5
ENSG00000104435	STMN2	0.48	ENSG00000239670	AL355864.2	4.4
ENSG00000139178	C1RL	0.48	ENSG00000236940	AL589765.3	4.3
ENSG00000278916	CEP83-AS1	0.47	ENSG00000171303	KCNK3	4.3
ENSG00000260081	AF274858.1	0.47	ENSG00000143469	SYT14	4.3

Supplemental Table 2A – continued 1

Transcripts whose levels were altered by KD-MKI67.
Left: reduced; right: increased.

ENSG00000207088	SNORA7B	0.47
ENSG00000090971	NAT14	0.47
ENSG00000273338	AC103591.3	0.47
ENSG00000171502	COL24A1	0.47
ENSG00000166734	CASC4	0.47
ENSG00000207257	RNU6-18P	0.47
ENSG00000168209	DDIT4	0.47
ENSG00000261514	LINC01976	0.47
ENSG00000077264	PAK3	0.47
ENSG00000143847	PPFIA4	0.47
ENSG00000279982	AL162274.3	0.47
ENSG00000115252	PDE1A	0.47
ENSG00000141750	STAC2	0.47
ENSG00000206972	RNU6-17P	0.47
ENSG00000198961	PJA2	0.47
ENSG00000254910	AC136475.2	0.47
ENSG00000278596	MIR6077	0.47
ENSG00000116761	CTH	0.46
ENSG00000200087	SNORA73B	0.46
ENSG00000185100	ADSSL1	0.46
ENSG00000141505	ASGR1	0.46
ENSG00000102007	PLP2	0.46
ENSG00000106948	AKNA	0.46
ENSG00000163110	PDLIM5	0.46
ENSG00000173208	ABCD2	0.46
ENSG00000074410	CA12	0.46
ENSG00000138757	G3BP2	0.46
ENSG00000197210	AP000550.1	0.46
ENSG00000257017	HP	0.46
ENSG00000160469	BRSK1	0.46
ENSG00000290904		0.46
ENSG00000200312	RN7SKP255	0.46
ENSG00000207187	SNORA10B	0.46
ENSG00000213920	MDP1	0.46
ENSG00000252826	RNU1-92P	0.45
ENSG00000223878	PPIAP53	0.45
ENSG00000129675	ARHGEF6	0.45
ENSG00000053524	MCF2L2	0.45
ENSG00000201665	RN7SKP6	0.45
ENSG00000183638	RP1L1	0.45
ENSG00000213967	ZNF726	0.45
ENSG00000185432	METTL7A	0.45
ENSG00000291057		0.45
ENSG00000114268	PFKFB4	0.45
ENSG00000182103	FAM181B	0.45
ENSG00000010379	SLC6A13	4.2
ENSG00000274529	SEBOX	4.2
ENSG00000166257	SCN3B	4.1
ENSG00000116544	DLGAP3	3.8
ENSG00000274569	AC024884.1	3.7
ENSG00000187642	PERM1	3.6
ENSG00000154736	ADAMTS5	3.6
ENSG00000151414	NEK7	3.6
ENSG00000224854	CDKN2A-AS1	3.5
ENSG00000103723	AP3B2	3.5
ENSG00000162981	FAM84A	3.4
ENSG00000267649	AC010327.4	3.4
ENSG00000008056	SYN1	3.3
ENSG00000134042	MRO	3.2
ENSG00000128564	VGF	3.2
ENSG00000204428	LY6G5C	3.2
ENSG00000284820	AC068946.2	3.1
ENSG00000168993	CPLX1	3.1
ENSG00000231304	SGO1-AS1	3.1
ENSG00000155886	SLC24A2	3
ENSG00000168843	FSTL5	3
ENSG00000273682	AC109583.2	3
ENSG00000172667	ZMAT3	3
ENSG00000261678	SCRT1	3
ENSG00000170540	ARL6IP1	3
ENSG00000140323	DISP2	2.9
ENSG00000188124	OR2AG2	2.9
ENSG00000238247	AC006210.2	2.9
ENSG00000289983		2.9
ENSG00000203877	RIPPLY2	2.9
ENSG00000092607	TBX15	2.9
ENSG00000237863	AL035425.1	2.8
ENSG00000204624	DISP3	2.8
ENSG00000125966	MMP24	2.8
ENSG00000204390	HSPA1L	2.8
ENSG00000136099	PCDH8	2.8
ENSG00000232218	AL021937.2	2.8
ENSG00000158089	GALNT14	2.8
ENSG00000277504	AC010536.3	2.7
ENSG00000148408	CACNA1B	2.7
ENSG00000217060	AL135903.1	2.7
ENSG00000263731	AC145207.5	2.7
ENSG00000226784	PGAM4	2.7
ENSG00000130287	NCAN	2.6
ENSG00000073598	FNDC8	2.6

Supplemental Table 2A-3 – continued 2

Transcripts whose levels were altered by KD-MKI67.
Left: reduced; right: increased.

ENSG00000006327	TNFRSF12A	0.45	ENSG00000168348	INSM2	2.6
ENSG00000260693	AC026150.1	0.45	ENSG00000164061	BSN	2.6
ENSG00000240392	RPL9P3	0.44	ENSG00000135127	BICDL1	2.6
ENSG00000180739	S1PR5	0.44	ENSG00000119283	TRIM67	2.5
ENSG00000213760	ATP6V1G2	0.44	ENSG00000183150	GPR19	2.5
ENSG00000106123	EPHB6	0.44	ENSG00000089558	KCNH4	2.5
ENSG00000090539	CHRD	0.44	ENSG00000155265	GOLGA7B	2.5
ENSG00000110786	PTPN5	0.44	ENSG00000253307	AC011676.1	2.5
ENSG00000264462	MIR3648-2	0.44	ENSG00000261342	AC006538.1	2.5
ENSG00000235034	C19orf81	0.44	ENSG00000242265	PEG10	2.5
ENSG00000137959	IFI44L	0.44	ENSG00000167619	TMEM145	2.5
ENSG00000177350	RPL13AP3	0.44	ENSG00000171314	PGAM1	2.5
ENSG00000135916	ITM2C	0.44	ENSG00000188060	RAB42	2.5
ENSG00000222041	CYTOR	0.44	ENSG00000254202	AC015522.1	2.4
ENSG00000020577	SAMD4A	0.44	ENSG00000186076	AC012085.1	2.4
ENSG00000224243	SOX1-OT	0.44	ENSG00000072657	TRHDE	2.4
ENSG00000129946	SHC2	0.44	ENSG00000105825	TFPI2	2.4
ENSG00000281103	TRG-AS1	0.44	ENSG00000162368	CMPK1	2.4
ENSG00000230873	STMND1	0.44	ENSG00000107105	ELAVL2	2.4
ENSG00000050130	JKAMP	0.43	ENSG00000216285	AC078819.1	2.4
ENSG00000004799	PDK4	0.43	ENSG00000152932	RAB3C	2.4
ENSG00000250069	AC011379.1	0.43	ENSG00000006576	PHTF2	2.4
ENSG00000157502	MUM1L1	0.43	ENSG00000271853	AL162258.1	2.4
ENSG00000223324	RN7SKP273	0.43	ENSG00000102003	SYP	2.4
ENSG00000118513	MYB	0.43	ENSG00000229214	LINC00242	2.3
ENSG00000150281	CTF1	0.43	ENSG00000186019	AC021092.1	2.3
ENSG00000163584	RPL22L1	0.43	ENSG00000254612	AP001000.1	2.3
ENSG00000172731	LRRC20	0.43	ENSG00000145920	CPLX2	2.3
ENSG00000275708	MIR3648-1	0.43	ENSG00000140403	DNAJA4	2.3
ENSG00000206702	RNU1-11P	0.43	ENSG00000197568	HHLA3	2.3
ENSG00000164405	UQCRQ	0.43	ENSG00000137710	RDX	2.3
ENSG00000242352	FAM91A3P	0.43	ENSG00000138061	CYP1B1	2.3
ENSG00000243926	TIPARP-AS1	0.43	ENSG00000267197	AC011461.1	2.3
ENSG00000283528	TCAF2C	0.43	ENSG00000007952	NOX1	2.3
ENSG00000234694	AL139289.2	0.42	ENSG00000130876	SLC7A10	2.3
ENSG00000141293	SKAP1	0.42	ENSG00000257923	CUX1	2.2
ENSG00000109107	ALDOC	0.42	ENSG00000173947	PIFO	2.2
ENSG00000225968	ELFN1	0.42	ENSG00000259533	AC040958.1	2.2
ENSG00000171219	CDC42BPG	0.42	ENSG00000143127	ITGA10	2.2
ENSG00000170074	FAM153A	0.42	ENSG00000092820	EZR	2.2
ENSG00000160131	VMA21	0.42	ENSG00000021645	NRXN3	2.2
ENSG00000128965	CHAC1	0.42	ENSG00000101638	ST8SIA5	2.2
ENSG00000273355	AP000894.4	0.42	ENSG00000274776	AC090241.3	2.2
ENSG00000255107	AC079089.2	0.42	ENSG00000166450	PRTG	2.2
ENSG00000213160	KLHL23	0.42	ENSG00000231530	AL157932.1	2.2

Supplemental Table 2A-3 – continued 3

Transcripts whose levels were altered by KD-MKI67.
Left: reduced; right: increased.

ENSG00000181458	TMEM45A	0.42	ENSG00000151490	PTPRO	2.2
ENSG00000204709	LINC01556	0.42	ENSG00000115762	PLEKHB2	2.2
ENSG00000006638	TBXA2R	0.42	ENSG00000141449	GREB1L	2.2
ENSG00000253190	AC084082.1	0.42	ENSG00000198944	SOWAHA	2.2
ENSG00000278356	AC005911.1	0.42	ENSG00000168243	GNG4	2.2
ENSG00000006611	USH1C	0.42	ENSG00000132026	RTBDN	2.2
ENSG00000092758	COL9A3	0.42	ENSG00000188760	TMEM198	2.2
ENSG00000229124	VIM-AS1	0.42	ENSG00000271601	LIX1L	2.2
ENSG00000143850	PLEKHA6	0.42	ENSG00000206172	HBA1	2.2
ENSG00000287729		0.42	ENSG00000179066	AC020907.1	2.2
ENSG00000168079	SCARA5	0.41	ENSG00000164082	GRM2	2.1
ENSG00000171798	KNDC1	0.41	ENSG00000135069	PSAT1	2.1
ENSG00000230882	AC005077.4	0.41	ENSG00000180720	CHRM4	2.1
ENSG00000171992	SYNPO	0.41	ENSG00000099822	HCN2	2.1
ENSG00000289827		0.41	ENSG00000270521	AL450336.1	2.1
ENSG00000230074	AL162231.2	0.4	ENSG00000080371	RAB21	2.1
ENSG00000231107	LINC01508	0.4	ENSG00000101938	CHRDL1	2.1
ENSG00000272583	AL592494.3	0.4	ENSG00000268655	AC008687.4	2.1
ENSG00000126838	PZP	0.4	ENSG00000280106	AC008555.8	2.1
ENSG00000232352	SEMA3B-AS1	0.4	ENSG00000287005		2.1
ENSG00000258545	RHOXF1-AS1	0.4	ENSG00000120675	DNAJC15	2.1
ENSG00000144908	ALDH1L1	0.4	ENSG00000163347	CLDN1	2.1
ENSG00000271078	AC139426.3	0.4	ENSG00000108468	CBX1	2.1
ENSG00000237853	NFIA-AS1	0.4	ENSG00000136928	GABBR2	2.1
ENSG00000248152	AC093879.1	0.4	ENSG00000118276	B4GALT6	2.1
ENSG00000160111	CPAMD8	0.4	ENSG00000255200	PGAM1P8	2.1
ENSG00000222210	RN7SKP65	0.4	ENSG00000167555	ZNF528	2.1
ENSG00000231908	IDH1-AS1	0.39	ENSG00000240280	TCAM1P	2.1
ENSG00000128242	GAL3ST1	0.39	ENSG00000188536	HBA2	2
ENSG00000165181	C9orf84	0.39	ENSG00000197457	STMN3	2
ENSG00000187479	C11orf96	0.39	ENSG00000187730	GABRD	2
ENSG00000263164	AC087500.2	0.39	ENSG00000165476	REEP3	2
ENSG00000188729	OSTN	0.39	ENSG00000254893	AC113404.3	2
ENSG00000183114	FAM43B	0.39	ENSG00000272142	AL359643.3	2
ENSG00000135842	FAM129A	0.39	ENSG00000272945	AL356299.2	2
ENSG00000277739	RNA5-8S5	0.38	ENSG00000260536	AL035071.2	2
ENSG00000228812	LAMA5-AS1	0.38	ENSG00000148798	INA	2
ENSG00000290398		0.38	ENSG00000108309	RUNDC3A	2
ENSG00000130589	HELZ2	0.38	ENSG00000280351	AC127496.7	2
ENSG00000274917	RNA5-8SN5	0.38	ENSG00000134256	CD101	2
ENSG00000272610	MAGI1-IT1	0.38	ENSG00000242866	STRC	2
ENSG00000106066	CPVL	0.38	ENSG00000090530	P3H2	2
ENSG00000250656	ST3GAL1P1	0.38	ENSG00000130558	OLFM1	2
ENSG00000221676	RNU6ATAC	0.37	ENSG00000260257	AL035071.1	2
ENSG00000246465	AC138904.1	0.37	ENSG00000267113	AF038458.1	2

Supplemental Table 2A - continued 4

Transcripts whose levels were altered by KD-MKI67.
Left: reduced; right: increased.

ENSG00000228423	AL357552.2	0.37
ENSG00000235020	AL390783.1	0.37
ENSG00000185022	MAFF	0.37
ENSG00000160318	CLDND2	0.37
ENSG00000238531	SNORD105B	0.37
ENSG00000255874	LINC00346	0.37
ENSG00000226519	LINC00390	0.37
ENSG00000175899	A2M	0.37
ENSG00000176171	BNIP3	0.37
ENSG00000131721	RHOXF2	0.37
ENSG00000128040	SPINK2	0.37
ENSG00000266472	MRPS21	0.37
ENSG00000130522	JUND	0.36
ENSG00000248712	CCDC153	0.36
ENSG00000213904	LIPE-AS1	0.36
ENSG00000280157	AL359510.2	0.36
ENSG00000201901	RN7SKP48	0.36
ENSG00000259439	LINC01833	0.36
ENSG00000228288	PCAT6	0.36
ENSG00000223751	AC116609.1	0.36
ENSG00000247095	MIR210HG	0.36
ENSG00000068697	LAPTM4A	0.35
ENSG00000202515	VTRNA1-3	0.35
ENSG00000102359	SRPX2	0.35
ENSG00000197358	BNIP3P1	0.35
ENSG00000225767	AL049637.1	0.35
ENSG00000130643	CALY	0.35
ENSG00000125730	C3	0.35
ENSG00000275215	RNA5-8SN4	0.35
ENSG00000198168	SVIP	0.35
ENSG00000254936	AF131215.4	0.35
ENSG00000132321	IQCA1	0.35
ENSG00000289065		0.34
ENSG00000238184	CD81-AS1	0.34
ENSG00000238961	SNORA47	0.34
ENSG00000144331	ZNF385B	0.34
ENSG00000049249	TNFRSF9	0.34
ENSG00000103528	SYT17	0.34
ENSG00000188487	INSC	0.34
ENSG00000003436	TFPI	0.34
ENSG00000203989	RHOXF2B	0.34
ENSG00000189377	CXCL17	0.33
ENSG00000152137	HSPB8	0.33
ENSG00000160801	PTH1R	0.33
ENSG00000067842	ATP2B3	0.33

ENSG00000271580	AL583832.1	2
ENSG00000187902	SHISA7	2
ENSG00000092529	CAPN3	2
ENSG00000288971		2
ENSG00000128923	MINDY2	2
ENSG00000001084	GCLC	2
ENSG00000158050	DUSP2	2
ENSG00000148677	ANKRD1	2
ENSG00000169252	ADRB2	2
ENSG00000101367	MAPRE1	2
ENSG00000102924	CBLN1	2
ENSG00000103056	SMPD3	2
ENSG00000009335	UBE3C	2
ENSG00000165323	FAT3	2
ENSG00000135048	TMEM2	2
ENSG00000198146	ZNF770	2
ENSG00000290717		2
ENSG00000187796	CARD9	2
ENSG00000163485	ADORA1	2
ENSG00000006468	ETV1	2
ENSG00000289210		2
ENSG00000171649	ZIK1	2

Supplemental Table 2A - continued 5

Transcripts whose levels were altered by KD-MKI67.
Left: reduced.

ENSG00000139547	RDH16	0.33
ENSG00000227533	SLC2A1-AS1	0.33
ENSG00000184545	DUSP8	0.33
ENSG00000276900	AC023157.3	0.33
ENSG00000245864	MEF2C-AS2	0.33
ENSG00000163683	SMIM14	0.32
ENSG00000132518	GUCY2D	0.32
ENSG00000279373	AC027228.3	0.32
ENSG00000166596	CFAP52	0.32
ENSG00000261519	AC010542.4	0.32
ENSG00000287525		0.32
ENSG00000231697	NANOGP5	0.32
ENSG00000248787	AC092903.2	0.32
ENSG00000274461	AL391425.1	0.31
ENSG00000269887	AL391001.1	0.31
ENSG00000206669	RF00019	0.31
ENSG00000174951	FUT1	0.31
ENSG00000288993		0.31
ENSG00000273730	RNA5-8SN2	0.3
ENSG00000165092	ALDH1A1	0.3
ENSG00000260498	AC126696.3	0.3
ENSG00000224807	DUX4L9	0.3
ENSG00000289609		0.29
ENSG00000267121	AC008105.3	0.29
ENSG00000128165	ADM2	0.29
ENSG00000199396	RNA5S5	0.29
ENSG00000233930	KRTAP5-AS1	0.29
ENSG00000253961	AC009563.1	0.28
ENSG00000124253	PCK1	0.28
ENSG00000272247	AC080013.5	0.28
ENSG00000153303	FRMD1	0.28
ENSG00000280122	AC016168.3	0.28
ENSG00000290319		0.28
ENSG00000120051	CFAP58	0.28
ENSG00000228089	PNKDP1	0.27
ENSG00000139269	INHBE	0.27
ENSG00000233175	AC008105.1	0.27
ENSG00000215244	AL137145.2	0.26
ENSG00000224839	RPL12P17	0.26
ENSG00000079385	CEACAM1	0.26
ENSG00000287064		0.26
ENSG00000265962	GACAT2	0.26
ENSG00000197921	HES5	0.26
ENSG00000251359	WWC2-AS2	0.25
ENSG00000270480	AC073413.1	0.24

Supplemental Table 2A - continued 6

Transcripts whose levels were altered by KD-MKI67.
Left: reduced.

ENSG00000171695	LKAAEAR1	0.24
ENSG00000176046	NUPR1	0.24
ENSG00000260186	LINC02137	0.24
ENSG00000290531		0.24
ENSG00000148773	MKI67	0.24
ENSG00000290162		0.23
ENSG00000207609	MIR491	0.23
ENSG00000173267	SNCG	0.23
ENSG00000130303	BST2	0.22
ENSG00000259666	LINGO1-AS1	0.22
ENSG00000250377	AC008525.1	0.22
ENSG00000200728	RNU6-271P	0.22
ENSG00000139567	ACVRL1	0.21
ENSG00000201084	RF00019	0.2
ENSG00000238783	RF00019	0.2
ENSG00000289159		0.2
ENSG00000226900	AL451069.1	0.2
ENSG00000239405	TMED10P2	0.19
ENSG00000159167	STC1	0.19
ENSG00000286478		0.18
ENSG00000261823	AC084782.2	0.18
ENSG00000128340	RAC2	0.18
ENSG00000246523	AP001528.1	0.17
ENSG00000235448	LURAP1L-AS1	0.17
ENSG00000289379		0.17
ENSG00000280166	AC016542.3	0.17
ENSG00000174059	CD34	0.17
ENSG00000286961		0.17
ENSG00000287094		0.16
ENSG00000276700	RNA5-8S4	0.16
ENSG00000267762	AC048380.1	0.16
ENSG00000289644		0.16
ENSG00000249306	LINC01411	0.16
ENSG00000162344	FGF19	0.16
ENSG00000185985	SLITRK2	0.16
ENSG00000280119	AC093642.2	0.15
ENSG00000228939	AKT3-IT1	0.15
ENSG00000228316	MTATP6P19	0.14
ENSG00000254528	AP000757.1	0.14
ENSG00000186453	FAM228A	0.14
ENSG00000290586		0.14
ENSG00000055813	CCDC85A	0.14
ENSG00000239731	RN7SL825P	0.14
ENSG00000261837	AC046158.2	0.14
ENSG00000236528	AL033528.2	0.13

Supplemental Table 2A - continued 7

Transcripts whose levels were altered by KD-MKI67.
Left: reduced.

ENSG00000240210	AL122013.1	0.12
ENSG00000259999	AC009054.1	0.12
ENSG00000269637	RPL12P41	0.12
ENSG00000091138	SLC26A3	0.11
ENSG00000211698	TRGV4	0.11
ENSG00000280721	LINC01943	0.11
ENSG00000160188	RSPH1	0.11
ENSG00000171401	KRT13	0.1
ENSG00000231130	HLA-T	0.1
ENSG00000213133	PPP1R14BP5	0.1
ENSG00000276524	AC010999.2	0.1
ENSG00000234663	LINC01934	0.1
ENSG00000235224	AL591212.2	0.1
ENSG00000257512	AC124947.2	0.1
ENSG00000006606	CCL26	0.1
ENSG00000285572		0.1
ENSG00000277710	AL589743.8	0.09
ENSG00000235848	RMDN2-AS1	0.09
ENSG00000259062	ACTN1-AS1	0.09
ENSG00000227913	KRT8P44	0.09
ENSG00000073146	MOV10L1	0.09
ENSG00000275908	RF00618	0.09
ENSG00000267573	KRT8P5	0.09
ENSG00000275776	RN7SL185P	0.09
ENSG00000265565	MIR3143	0.09
ENSG00000272862	AC106052.1	0.09
ENSG00000205869	KRTAP5-1	0.09
ENSG00000115523	GNLY	0.08
ENSG00000277109	AL935212.4	0.07
ENSG00000246082	NUDT16P1	0.07
ENSG00000225392	AC016700.1	0.07
ENSG00000211459	MT-RNR1	0.07
ENSG00000095370	SH2D3C	0.07
ENSG00000213049	HNRNPA1P34	0.06
ENSG00000124469	CEACAM8	0.06
ENSG00000211701	TRGV1	0.05
ENSG00000265128	AC016866.2	0.05
ENSG00000242236	RN7SL594P	0.04
ENSG00000241218	AC063944.2	0.04
ENSG00000273336	OR7M1P	0.04
ENSG00000223732	AL359706.1	0.04

Supplemental Table 2B

Transcripts whose levels were altered by KD-GNL2.
Left: reduced; right: increased.

geneID	geneSymbol	foldChange by KD-GLN2
ENSG00000067221	STOML1	0.48
ENSG00000139508	SLC46A3	0.47
ENSG00000100934	SEC23A	0.46
ENSG00000164603	BMT2	0.46
ENSG00000155111	CDK19	0.45
ENSG00000136240	KDELR2	0.45
ENSG00000168610	STAT3	0.43
ENSG00000124120	TTPAL	0.42
ENSG00000156671	SAMD8	0.41
ENSG00000132912	DCTN4	0.37
ENSG00000141639	MAPK4	0.35

geneID	geneSymbol	foldChange by GNL2
ENSG00000216285	AC078819.1	2.7
ENSG00000171314	PGAM1	2.5
ENSG00000186076	AC012085.1	2.5
ENSG00000108468	CBX1	2.4
ENSG00000084628	NKAIN1	2.4
ENSG00000159753	CARMIL2	2.3
ENSG00000143469	SYT14	2.3
ENSG00000280916	FOXCUT	2.3
ENSG00000204389	HSPA1A	2.3
ENSG00000103723	AP3B2	2.2
ENSG00000136928	GABBR2	2.2
ENSG00000204388	HSPA1B	2.2
ENSG00000170540	ARL6IP1	2.2
ENSG00000102003	SYP	2.1
ENSG00000260257	AL035071.1	2.1
ENSG00000226784	PGAM4	2.1
ENSG00000168993	CPLX1	2.1
ENSG00000153162	BMP6	2
ENSG00000263731	AC145207.5	2
ENSG00000073150	PANX2	2
ENSG00000138061	CYP1B1	2
ENSG00000179743	AL450998.2	2
ENSG00000172667	ZMAT3	2
ENSG00000167619	TMEM145	2

Supplemental Table 2C

Transcripts whose levels were altered by KD-MDN1.
Left: reduced; right: increased.

geneID	geneSymbol	foldChange by KD-MDN1
ENSG00000277027	RMRP	0.5
ENSG00000180979	LRRC57	0.49
ENSG00000172115	CYCS	0.49
ENSG00000128000	ZNF780B	0.49
ENSG00000207205	RNVU1-15	0.49
ENSG00000135070	ISCA1	0.49
ENSG00000229807	XIST	0.49
ENSG00000116761	CTH	0.49
ENSG00000264229	RNU4ATAC	0.49
ENSG00000250337	PURPL	0.49
ENSG00000081320	STK17B	0.49
ENSG00000230358	SPDYE21P	0.48
ENSG00000213025	COX20P1	0.48
ENSG00000169019	COMMD8	0.48
ENSG00000213453	FTH1P3	0.48
ENSG00000269929	AL158152.1	0.48
ENSG00000201998	SNORA23	0.48
ENSG00000250903	GMDS-AS1	0.48
ENSG00000236439	AC099336.2	0.48
ENSG00000252947	SCARNA1	0.48
ENSG00000111816	FRK	0.48
ENSG00000264112	AC015813.1	0.48
ENSG00000274585	RNU2-1	0.48
ENSG00000230291	AC078817.1	0.48
ENSG00000122545	SEPIN7	0.47
ENSG00000212232	SNORD17	0.47
ENSG00000243137	PSG4	0.47
ENSG00000227081	AC005912.1	0.47
ENSG00000274862	RF00004	0.47
ENSG00000278591	RF00004	0.47
ENSG00000119900	OGFRL1	0.47
ENSG00000274062	RF00004	0.47
ENSG00000291015	NA	0.47
ENSG00000278774	RF00004	0.46
ENSG00000230606	AC092683.1	0.46
ENSG00000215386	MIR99AHG	0.46
ENSG00000276596	RF00004	0.46
ENSG00000157214	STEAP2	0.46
ENSG00000277903	RF00004	0.46
ENSG00000212402	SNORA74B	0.46
ENSG00000232931	LINC00342	0.46
ENSG00000275219	RF00004	0.45

geneID	geneSymbol	foldChange by KD-MDN1
ENSG00000204389	HSPA1A	3.08
ENSG00000216285	AC078819.1	2.95
ENSG00000204388	HSPA1B	2.92
ENSG00000171314	PGAM1	2.79
ENSG00000186076	AC012085.1	2.73
ENSG00000108468	CBX1	2.69
ENSG00000210151	MT-TS1	2.64
ENSG00000148408	CACNA1B	2.47
ENSG00000130477	UNC13A	2.46
ENSG00000172667	ZMAT3 (p53 target gene)	2.46
ENSG00000240036	AC104563.1(pseu)	2.44
ENSG00000251259	AC004069.1(new)	2.41
ENSG00000168993	CPLX1	2.36
ENSG00000167680	SEMA6B	2.36
ENSG00000159753	CARMIL2	2.35
ENSG00000128228	SDF2L1(a part of Chap complex)	2.3
ENSG00000167136	ENDOG (DNA nuclease)	2.28
ENSG00000073150	PANX2	2.27
ENSG00000135127	BICDL1 (make dyenin active)	2.22
ENSG00000001630	CYP51A1	2.18
ENSG00000166897	ELFN2	2.17
ENSG00000104967	NOVA2	2.16
ENSG00000173404	INSM1	2.12
ENSG00000177374	HIC1	2.12
ENSG00000178531	CTXN1	2.1
ENSG00000153162	BMP6	2.08
ENSG00000179673	RPRML	2.08
ENSG00000139219	COL2A1	2.08
ENSG00000113196	HAND1	2.05
ENSG00000226784	PGAM4	2.05
ENSG00000177542	SLC25A22	2.04
ENSG00000059915	PSD	2.04
ENSG00000110675	ELMOD1	2.02
ENSG00000160161	CILP2	2.02
ENSG00000171388	APLN	2.02
ENSG00000078549	ADCYAP1R1	2.01
ENSG00000180730	SHISA2 (WNT signalling)	2.01
ENSG00000168282	MGAT2	2
ENSG00000272449	AL139246.5	2

Supplemental Table 3

Transcripts relevant to apoptosis, proliferation, gene silencing, etc., which were altered by KD-MKI67, KD-GNL2, or KD-MDN1. baseMean is the data derived from the KD-MKI67 and KD-CTL experiment.

geneSymbol	baseMean	foldChange by KS-MKI67	padj	foldChange by KD-GNL2	padj	foldChange by KD-MDN1
ACIN1	6525.87011	1.19	0.0294909	1.14	0.13482521	1.01
ATF2	1375.84158	0.69	5.1447E-05	0.97	0.90744492	0.77
AVEN	186.721707	1.6	0.00066604	1.09	0.83251818	1.2
BAD	395.727069	0.65	0.0000235	0.82	0.31902837	1.16
BAX	1060.81732	0.95	0.73692296	1.08	0.70381429	1.28
BCL2	234.784548	0.91	0.62264745	1.05	0.88175239	1.01
BCL2L1	352.174859	1.19	0.13517475	0.98	0.26102189	1.08
BCL2L11 (BIM)	784.98636	1.76	1.79E-12	0.89	0.63154086	1.18
BCL2L12	1014.27884	0.98	0.90990817	1.04	0.82413085	1.32
BCL2L13	1931.96917	0.92	0.49042425	0.89	0.30724501	1.18
BCL2L2	519.778725	0.98	0.94472229	1.13	0.53245947	0.81
BNIP3	1766.6073	0.37	1.54E-19	0.97	0.89211295	0.93
BNIP3L	963.9375	0.72	0.02969017	1.1	0.49270628	0.99
CBX1	1885.8298	2.14	1.1936E-26	2.47	1.1E-31	2.69
CBX2	1693.84242	0.77	0.00510751	1.11	0.38783507	1.25
CBX3	6664.09131	0.97	0.89063208	1.08	0.44064564	1.01
CBX5	10289.6162	1.03	0.74043444	0.99	0.95261608	1.03
CBX6	6286.91799	1.2	0.15483266	1.32	0.0000894	1.23
CBX7	150.514961	0.79	0.17748078	1.04	0.79895867	1.09
DDIT4	2135.83738	0.47	0.05407216	0.9	0.46557537	1.05
EHMT2	1375.95242	0.83	0.0500511	0.92	0.53166851	0.97
FAIM	504.406747	0.55	1.2706E-07	1.05	0.82305947	0.94
FAM129A (NIBAN1)	76.0507131	0.39	2.9242E-06	0.88	0.7894266	NA
HDAC1	173.192564	0.81	0.20828252	1.12	0.21640663	1.15
HDAC2	7962.77986	0.75	0.00543859	0.99	0.98852976	0.9
HDAC3	2025.07632	1.18	0.03863481	0.98	0.94767334	0.71
LAMTOR1	953.313984	1.14	0.244478	1.07	0.72646725	1.39
LAMTOR2	562.519415	0.97	0.88875802	1.06	0.81017156	1.32
LAMTOR3	977.79487	1.12	0.37617509	0.94	0.76516646	0.74
LAMTOR4	1161.88496	0.89	0.54361192	1.03	0.87826434	1.63
LAMTOR5	1352.91374	1	0.99482779	1.02	0.9046873	1.11
LAS1L	2337.13137	0.99	0.98845801	0.96	0.85522891	1.13
MDN1	9556.3518	1.33	0.0002047	0.99	0.9622943	0.33
PELP1	3134.2021	1.13	0.11484998	1.02	0.89044665	1.25
PES1	4118.45886	1.25	0.01392092	1.21	0.05486439	1.35
RRP8	676.800996	1.05	0.68917952	0.95	0.8578854	1.04
SENP3	792.822599	0.82	0.06899426	1.17	0.30085731	1.27
SETD1B	1446.38993	1.42	2.7541E-05	1.03	0.88906261	1.04
SIRT1	1365.18942	1.25	0.01086003	0.96	0.85931077	0.89
SUV39H1	627.494868	1.1	0.41751369	0.98	0.58348974	1
SUV39H2	1431.29511	1.42	4.9975E-05	1.25	0.0476658	0.98
TEX10	1808.01552	1.1	0.35104921	1.02	0.90511055	1.01
TP53	2927.44865	0.57	1.45E-16	1.04	0.74083083	1.01

Supplemental Table 3 - continued.

Transcripts relevant to apoptosis, proliferation, gene silencing, etc., which were altered by KD-MKI67, KD-GNL2, or KD-MDN1. baseMean is the data derived from the KD-MKI67 and KD-CTL experiment.

geneSymbol	baseMean	foldChange by KS-MKI67	padj	foldChange by KD-GNL2	padj	foldChange by KD-MDN1
SETD1B	1446.38993	1.42	2.7541E-05	1.03	0.88906261	1.04
SIRT1	1365.18942	1.25	0.01086003	0.96	0.85931077	0.89
SUV39H1	627.494868	1.1	0.41751369	0.98	0.58348974	1
SUV39H2	1431.29511	1.42	4.9975E-05	1.25	0.0476658	0.98
TEX10	1808.01552	1.1	0.35104921	1.02	0.90511055	1.01
TP53	2927.44865	0.57	1.45E-16	1.04	0.74083083	1.01
WDR18	1257.56712	0.99	0.94322574	0.94	0.76582482	1.14
XIAP	2584.6527	1.31	0.00013215	1.14	0.25842717	0.84
MTOR	4306.41124	1.08	0.35063023	1.06	0.66538858	1.09
RPTOR	1906.26415	1.3	0.00046104	1.1	0.55663665	1.23
RICTOR	1395.77763	1.21	0.02612281	1.07	0.66538858	0.91
PIK3R3	899.405844	1.3	0.03184834	1.01	0.94500577	0.97
PIK3R1	728.687501	1.21	0.04322733	1.11	0.60609101	1.11
PIK3R4	1324.39406	1.19	0.05011104	1.17	0.26025137	1.23
SLC7A2	1836.50515	1.78	2.8308E-17	1.09	0.56074113	1.07
SLC7A5	8290.97637	1.42	1.9169E-08	0.97	0.86865239	1.1
SLC7A6	1220.45277	1.19	0.0498985	0.91	0.62967718	1.08

Supplemental Table 4

Transcripts relevant to the electron transport and glycolysis, which were altered by KD-MKI67, KD-GNL2, or KD-MDN1. baseMean is the data derived from the KD-MKI67 and KD-CTL experiment.

geneSmbol	baseMean	foldChange by KD-MKI67	padj	MS counts KD-CTL/KD-MKI67	MS-foldChange by KD-MKI67	foldChange by KD-GNL2	padj	foldChange by KD-MDN1	padj
ALDOC	94.6532562	0.42	8.278E-06	3+4/5+5	1.42	1.24	0.52442863	1.27	0.33303457
COX14	381.261561	0.94	0.81170344	NA	NA	1.16	0.56838903	1.81	0.00040982
COX16	182.627926	1.43	0.01840044	NA	NA	0.89	0.80662256	1.15	0.64152199
COX4I1	4877.19678	0.98	0.94133044	NA	NA	1.05	0.69570488	1.3	0.0216517
COX5B	2636.35035	0.69	0.00054541	NA	NA	0.89	0.32705196	1.05	0.70960321
COX6C	1780.72749	0.81	0.1611866	NA	NA	0.86	0.34754871	0.62	4.6829E-05
COX7B	4544.86154	0.91	0.4799186	NA	NA	0.83	0.61674769	0.72	0.01585186
COX7C	8323.21849	0.78	0.00851682	1+0/0+0	0	0.8	0.3828186	0.83	0.14596283
COX8A	2018.40026	0.67	1.3742E-08	NA	NA	0.99	0.96010828	1.2	0.08709443
CYCS	7585.55985	1	0.35698923	6+6/6+8	1.16	1.15	0.10291107	0.49	5.2317E-26
HK2	3136.89185	0.57	3.8432E-08	7+7/6+4	0.71	1.19	0.04328824	1.34	0.00037985
NDUFA1	2919.58038	0.86	0.64530691	NA	NA	1.05	0.81248396	1.37	0.02141087
NDUFA13	1036.44164	0.88	0.23849016	NA	NA	1.08	0.71749323	1.33	0.02786505
NDUFA5	2234.89728	1.47	1.1569E-05	NA	NA	1.05	0.75496572	0.97	0.88255519
NDUFAB1	1330.56091	0.89	0.46129082	NA	NA	1.05	0.81652172	0.69	0.00013783
NDUFAF3	1716.54619	0.72	0.00034075	NA	NA	1.09	0.4710905	1.14	0.18031328
NDUFAF7	474.50843	0.87	0.35168881	NA	NA	0.83	0.27528616	0.7	0.00716145
NDUFB10	3120.58006	0.72	0.00059131	NA	NA	1.2	0.09244217	1.25	0.01557094
NDUFB4	2.28557465	0.69	NA	NA	NA	0.91	0.49068741	0.79	0.01142791
NDUFV1	2655.02504	0.9	0.33851372	NA	NA	1.02	0.88175239	1.26	0.03848132
PCK2	731.388809	0.48	1.7853E-07	11+9/5+3	0.4	0.61	4.47E-08	0.89	0.352116
PDK1	1672.75636	0.55	7.8942E-07	2+2/1+0	0.25	NA	NA	0.81	0.03860332
PDK2	277.370709	0.94	0.74211901	NA	NA	0.91	0.811149	1.06	0.79324741
PDK3	2546.31681	0.94	0.58716643	1+0/1+0	1	0.96	0.81435679	0.85	0.29302478
PDK4	39.9383353	0.43	0.003451	NA	NA	0.81	0.66889715	0.64	0.18834006
PFKFB1	12.0625389	1.08	NA	NA	NA	0.97	0.97291673	NA	NA
PFKFB2	829.451816	1.27	0.00960782	3+2/2+2	0.8	0.96	0.87489355	1.16	0.30371733
PFKFB3	1717.68791	1.08	0.5482271	3+2/2+0	0.4	1.26	0.01310105	1.26	0.01518446
PFKFB4	390.829847	0.45	2.0639E-09	NA	NA	0.84	0.40214215	1.16	0.3170445
PFKL	2820.73922	0.77	0.00103371	6+7/10+4	1.07	0.95	0.79588449	1.27	0.01256896
PFKM	1554.85631	1	0.97974975	17+12/9+6	0.51	1.13	0.40791142	1.31	0.00789021
PFKP	1411.20956	1.07	0.58475283	15+11/15+18	1.26	1.21	0.13191518	1.44	0.0009164
PGAM1	8239.01486	2.52	1.9625E-32	0+1/1+3	4	2.59	8.59E-64	2.79	6.9857E-50
PGAM4	287.605437	2.71	8.0028E-13	4+3/5+10	2.14	2.11	0.00000116	2.05	8.6329E-06
PGAM5	3744.99949	1.08	0.48774865	9+7/10+18	1.75	1.21	0.01845177	1.34	0.00296684
UQCR11	1502.70604	0.79	0.02453159	NA	NA	0.8	0.07890909	1.02	0.87334267
UQCRH	4642.76754	0.57	1.0562E-07	NA	NA	0.96	0.83183964	0.88	0.19840733
UQCRHL	273.380931	0.54	7.8975E-06	NA	NA	0.82	0.32788847	0.64	0.00237925
UQCRQ	2522.93823	0.43	9.7389E-18	NA	NA	1.02	0.9122584	1.19	0.20356463

Supplemental Table 5. A list of plasmids and oligonucleotides used in this study

Plasmids	Template	vector	Primers	Foward primer	Reverse primer
pGNL2-G7	HEK293T total RNA	pEGFP-C2	Olit349 + 350	agcttcgaattcATGGTGAAGCCCAAGTAC	acatgtcccgcggtcagtggtggtggtggtggtgCTGCTTTTGTCTGAATTTTTTGC
pGNL2-#9	pGNL2-G7	pEGFP-C2	Olit364 + 365	CACCACCACCACCACCACTGA	GAATTCGAAGCTTGAGCTC
pGNL2-#1	pGNL2-G7	pEGFP-C2	Olit355 + 356	TAACTGATCATAATCAGCCATACC	CTGCTTTTGTCTGAATTTTTTGC
pGNL2-#2	pGNL2-G7	pEGFP-C2	Olit355 + 357	TAACTGATCATAATCAGCCATACC	AACTTGAACTACAACATCTGATGAA
pGNL2-#3	pGNL2-G7	pEGFP-C2	Olit355 + 358	TAACTGATCATAATCAGCCATACC	AAGTGTTGGATAATCCTGGG
pGNL2-#28	pGNL2-G7	pEGFP-C2	Olit355 + 371	TAACTGATCATAATCAGCCATACC	CACAATGTCTGTCTCGGAG
pGNL2-#29	pGNL2-G7	pEGFP-C2	Olit355 + 372	TAACTGATCATAATCAGCCATACC	CACAAGTGGCTCTGCAT
pGNL2-#30	pGNL2-G7	pEGFP-C2	Olit355 + 375	TAACTGATCATAATCAGCCATACC	AAGATCTGACACCTCCACA
pGNL2-#27	pGNL2-#4	pEGFP-C2	Olit355 + 386	TAACTGATCATAATCAGCCATACC	GTCGTTTCCCACATTTTCC
pGNL2-#4	pGNL2-G7	pEGFP-C2	Olit355 + 359	TAACTGATCATAATCAGCCATACC	CTTCCGCTTCTTTCCCT
pGNL2-#17	pGNL2-#1	pEGFP-C2	Olit369 + 364	GAAGATGTAGATGACAGAGCAC	GAATTCGAAGCTTGAGCTC
pGNL2-#10	pGNL2-#1	pEGFP-C2	Olit369 + 370	GAAGATGTAGATGACAGAGCAC	CTTTTTATAGATCTCTTCTTGAGCTTCATTT
pGNL2-#26	pGNL2-#4	pEGFP-C2	Olit385 + 364	ACCAAAGCCGTTATTAAAGC	GAATTCGAAGCTTGAGCTC
pGNL2-#5	pGNL2-G7	pEGFP-C2 but no EGFP	Olit353 + 354	ATGGTGAAGCCCAAGTAC	GGTGGCGACCGGTAG
pGNL2-#8	pGNL2-#5	pEGFP-C2 but no EGFP	Olit363 + 361	GTTGTTCAAGTAGAAAAAATTAAGAGTCC	CTTGGGCTTCACCATGG
pGNL2-#18	pGNL2-#5	pEGFP-C2 but no EGFP	Olit378 + 361	ACACTGGAAGAAGATGTAGATGA	CTTGGGCTTCACCATGG
pGNL2-#19	pGNL2-G7	pGEX-5X-1	Olit379 + 380	GCTTCGAATTCATGGTGAAGC	AGCCGCTCGAGTCGCGGTCAGTGGTG
pGNL2-#20	pGNL2-G7	pGEX-5X-1	Olit379 + 381	GCTTCGAATTCctggaagaagatgtagatgacaga	AGCCGCTCGAGTCGCGGTCAGTGGTG
pGNL2-#22	pGEX-5X-1	pGEX-5X-1	Olit384 + 383	GCCGCATCGTGACTGA	TCAGTGGTGGTGGTGGTGGTGGGGGATCCCACGAC
pGNL2-#21	pGNL2-G7	pGEX-5X-1	Olit380 + 382	GCTTCGAATTCATGGTGAAGC	AAGCCGCTCGAGTCAGTGGTGGTGGTGGTGTTCTTCCAGTGTTTTTCTTTGTTCTT

Supplemental Table 6

Double stranded siRNA

siRNA name	Target	Sequence
NC1	No activity in human cells	
hs.Ri.MKI67.13.1	MKI67 mRNA	5'- GCAUUGAAGGAAUCUGCAAAACAGA -3' 3'- UUCGUAACUUCCUUAGACGUUUUGUCU -5'
hs.Ri.GNL2.13.2	GNL2 mRNA	5'- CCCCUCACAUUGAAACUUACCUGAA -3' 3'- AAGGGGAGUGUAACUUUGAAUGGACUU -5'
hs.Ri.MDN1.13.1	MDN1 mRNA	5'- GCUAUCACGAUGGAGAUUGUCAACA -3' 3'- UUCGAUAGUGCUACCUCUAACAGUUGU -5'
hs.Ri.YTHDC2.13.1	YTHDC2 mRNA	5'- CGCCUGUCACUAUAUUGGUAUUCUG -3' 3'- CUGCGGACAGUGAUAUAACCAUAAGAC -5'
hs.Ri.YTHDC2.13.2	YTHDC2 mRNA	5'- GGUAUUUAAAAUGAAUACAACUUGA -3' 3'- AACCAUAAAUUUUACUUAUGUUGAACU -5'
hs.Ri.CNOT1.13.1	CNOT1 mRNA	5'- GAAUGAUCACAUUAGCUAAAAACAA -3' 3'- UCCUUACUAGUGUAAUCGAUUUUUGUU -5'
hs.Ri.CNOT1.13.2	CNOT1 mRNA	5'- AGCAUUUGGCUUCUAUCAGUCACTT -3' 3'- AGUCGUAAACCGAAGAUAGUCAGUGAA -5'
hs.Ri.G3BP1.13.1	G3BP1 mRNA	5'- GUUUCUUCUUUGAGAGUCAUGACTA -3' 3'- AACAAAGAAGAAACUCUCAGUACUGAU -5'
hs.Ri.G3BP1.13.2	G3BP1 mRNA	5'- GUGGACAAAUCAGAGCUUAAAGATT -3' 3'- UUCACCUGUUUAGUCUCGAAUUUCUAA -5'
hs.Ri.G3BP2.13.1	G3BP2 mRNA	5'- AAUGAGCUAAAGGAAUUCUUCAUGA -3' 3'- UUUUACUCGAUUUCCUUAAGAAGUACU -5'
hs.Ri.G3BP2.13.2	G3BP2 mRNA	5'- GAAUCUUUAAACAAUUCUGUGAGCA -3' 3'- UACUUAGAAAUUUGUUAAGACACUCGU -5'
hs.Ri.FMR1.13.1	FMR1 mRNA	5'- GUACUGAGCAGUGAUAUUCUUUGTT -3' 3'- UUCAUGACUCGUCACUAUAAGAAACAA -5'
hs.Ri.FMR1.13.2	FMR1 mRNA	5'- GUCACUGCUAUUGAUCUAGAUGAAG -3' 3'- CCCAGUGACGAUAACUAGAUCUACUUC -5'

Supplemental Table 7 Antibodies used in this work.

Target	Antibody	Host and Type	Concentration	(µg/ ml)		Cat #	Vendor
-	-	-	IF	WB	IP	-	-
CNOT1	CNOT1 (D5M1K)	r-Monoclonal		0.1		44613	Cell Signaling
FMR1	Anti-FMR1 (1F1)	m-Monoclonal		1		MABN2453	MILLIPORE
G3BP1	G3BP1 (E9G1M) XP	r-Monoclonal		0.075		61559S	Cell Signaling
G3BP2				0.031		31799S	Cell Signaling
GFP	GFP antibody, purified	r-Polyclonal		0.25	See Methods	SP3005P	ORIGENE
GNL2	GNL2 (B-8)	m-Monoclonal	2.5	1		sc-514050	SANT CRUZ
GNL2	GNL2 antibody	r-IgG			See Methods	A305-155A-M	BETHYL
6x His	Tetra.His Antibody	m-IgG1	1			34670	QIAGEN
6x His	U571WHA040-1	m-Polyclonal		0.1	See Methods	A00186-100	GenScript
MDN1	MDN1 antibody	r-Polyclonal	0.7	0.25	See Methods	PA556225	Thermo Fisher
MKI67	Human Ki-67/MKI67 antibody	r-Monoclonal	1	0.25	See Methods	MAB7617-SP	R&D
MKI67	Ki-67 (Ki67)	m-Monoclonal	8			sc-23900	SANT CRUZ
NEK7	NEK7 (C34C3)	r-Monoclonal		0.04		3057S	Cell Signaling
PELP1	PELP1 (D5Q4W)	r-Monoclonal	0.94				Cell Signaling
UNC13A		r-IgG		0.2		55053-1-AP	proteintech
YTHDC2	YTHDC2	r-IgG		0.2		27779-1-AP	proteintech
mouse IgGs, IgM, IgA	IRDye 680RD Goat anti-Mouse IgG	goat-Polyclonal		0.025		926-689070	LI-COR
rabbit IgG	IRDye 800 Affinity Purified Goat anti-Rabbit IgG	goat-Polyclonal		0.05		611-132-122	ROCKLAND
mouse IgG (H+L)	Goat anti-Mouse Highly Cross-Absorbed, Alexa Fluor 488	goat-Polyclonal	1			A11029	Thermo Fisher
rabbit IgG (H+L)	Goat anti-Rabbit Highly Cross-Absorbed, Alexa Fluor 555	goat-Polyclonal	1			A21429	Thermo Fisher